

**INFLUENCE OF LASER SURFACE TREATMENT ON
RESIDUAL STRESS DISTRIBUTION AND DYNAMIC
PROPERTIES IN ROTARY FRICTION WELDED
Ti-6Al-4V COMPONENTS**

DAVIES SHAMISO TSIKAYI

2019



INFLUENCE OF LASER SURFACE TREATMENT ON
RESIDUAL STRESS DISTRIBUTION AND DYNAMIC
PROPERTIES IN ROTARY FRICTION WELDED Ti-6Al-4V
COMPONENTS

By:

Davies Shamiso Tsikayi (209080067)

Submitted in fulfilment of the requirements for the degree of Doctor of
Philosophy Engineering: Mechanical to be awarded at the Nelson Mandela
University

Submitted: April 2019


Supervisor: Prof D.G. Hattingh

Co-Supervisor: Dr A. Steuwer

Copyright © 2018 Nelson Mandela University
All rights reserved

Declaration

I, **Davies Shamiso Tsikayi**, student number: 20908067 hereby declare that the *thesis for Students qualification to be awarded* is my own work and that it has not previously been submitted for assessment or completion of any postgraduate qualification to another University or for another qualification.

Signature: 

Davies Shamiso Tsikayi

Official use:

In accordance with Rule G5.6.3,

5.6.3 A treatise/dissertation/thesis must be accompanied by a written declaration on the part of the candidate to the effect that it is his/her own work and that it has not previously been submitted for assessment to another University or for another qualification. However, material from publications by the candidate may be embodied in a treatise/dissertation/thesis.

Acknowledgements

Thus far, the Lord has helped us.

(One Samuel 7:12)

First, to the Lord Almighty, I am because YOU ARE. Thank You Lord.

I would like to express my sincere gratitude to Prof D. G. Hattingh for his supervision and unconditional support during this research doctorate. It would not have been possible without his assistance and vast knowledge of the field of Friction Processing. I would also like to thank my co-supervisor Dr Steuwer, for all the assistance he provided during this work.

I would like to thank the staff of Nelson Mandela University metallurgy lab and eNtsa, “a Technology Innovation Agency station” for their technical and administrative support especially: Riaan Brown, Lucinda Lindsay and Nadine Goliath (administrative assistance), Coos Bosma (statistician) and William Goosen (CHRTEM), Kurt Jennicker and Marlon Koopman for their help in sample preparation as well as Amish Lalla, Melikhaya Nohonyaza and Jaromir Cizek for providing me with assistance in the manufacturing of the test samples. I would also like to the ESRF especially M. Buslaps.

To my fellow researchers, Willem Pentz, Madindwa Mashinini, Dreyer Bernard, Lindsay Swan and Nthatisi Koloï, thank you for the help and constructive criticism.

Further special mention goes to my wife (Ayanda), my family, my son (Ammi ‘Amza’ Osagyefo) and Viwe Mbelekane for their support during my studies.

I dedicate this thesis to my late father who passed away in 2007. He made me the man I am today and because of his hard work, I have got this far.

Contents

Declaration.....	iii
Acknowledgements.....	iv
Abstract.....	xv
List of Abbreviations.....	xviii
Nomenclature.....	xx
Glossary of Terms.....	xxii
Chapter 1. Project Overview.....	1
1.1. Background.....	1
1.2. Research Question.....	2
1.3. Problem Statement.....	3
1.3.1. Sub-problems.....	3
1.4. Objective.....	3
1.5. Hypothesis.....	4
1.6. Significance and Feasibility of Research.....	4
1.7. Delimitations.....	4
1.8. Research Methodology.....	5
1.9. Organisation of Thesis.....	5
Chapter 2. Literature Review.....	7
2.1. Introduction.....	7
2.2. Ti-6Al-4V Alloy.....	7
2.3. Friction Welding.....	15
2.3.1. Introduction.....	15
2.3.2. Rotary Friction Welding.....	18
2.4. Fracture Mode.....	21
2.4.1. Introduction.....	21
2.4.2. Fatigue Failure.....	22
2.4.3. Fatigue failure in Ti-6Al-4V.....	23
2.5. Residual Stresses.....	26
2.5.1. Nature and Origin.....	26

Table of Contents

2.5.2. Measuring Technique and determination of residual stresses .	27
2.5.3. Effect of residual stresses on fatigue life	29
2.6. Laser Material Processing	32
2.6.1. Introduction	32
2.6.2. Laser surface treatment	34
2.6.3. Laser surface treatment process parameters.....	39
2.7. Summary	41
Chapter 3. Research Material, Testing and Processing Platforms	43
3.1. Introduction	43
3.2. Research Material.....	43
3.3. Research Platforms	44
3.3.1. Weldcore III Friction processing platform	44
3.3.2. Trumpf TruLaser5020 laser cell.....	45
3.3.3. Temperature measurement.....	47
3.3.4. Rotating bending fatigue machine.....	48
3.4. RFW Processing of Ti-6Al-4V ELI Samples.....	52
3.4.1. Introduction	52
3.4.2. Rotary Friction Welding of Ti-6Al-4V set-up	52
3.4.3. RFW consumable stud design	53
3.4.4. RFW shielding mechanism.....	54
3.5. Summary	56
Chapter 4. Laser Surface Treatment	57
4.1. Introduction	57
4.2. Stage 1: Process Development on 3 mm Ti-6Al-4V Sheets.....	59
4.2.1. Introduction	59
4.2.2. Experimental set-up	59
4.2.3. Results	60
4.2.4. Summary.....	69
4.3. Stage 2: Laser Surface Treatment Strategy.....	70
4.3.1. Introduction	70

Table of Contents

4.3.2. Experimental set-up	71
4.3.3. LST strategy 1: Continuous.....	71
4.3.4. LST strategy 2: Non-continuous.....	75
4.4. Stage 3: Final Experimental Matrix	80
4.4.1. Introduction	80
4.4.2. Experimental Design	82
4.4.3. Experiment set-up	83
4.4.4. Statistical Analysis.....	87
4.5. Final Matrix Analysis.....	92
4.5.1. Visual Inspection	93
4.5.2. Macrostructure analysis of LST specimen.....	94
4.5.3. Hardness distribution of Laser Surface Treated Specimens	99
4.5.4. Selection specimens for final analysis.....	102
4.6. Summary	103
Chapter 5. Microstructural Characterisation	106
5.1. Introduction	106
5.2. Experimental Method.....	106
5.3. Microstructure Characterisation: Results	108
5.3.1. Parent material.....	108
5.3.2. Weld zone	110
5.3.3. RFW - LST specimens	113
5.4. Hardness Distribution in the Laser Surface Distributed Zone	116
5.5. Summary	118
Chapter 6. Residual Stresses and Fatigue Properties of Laser Surface Treated Specimens.....	120
6.1. Introduction.....	120
6.2. Residual Stress Analysis	120
6.2.1. Experimental method and set-up	121
6.2.2. Residual stress results	126
6.2.3. Summary.....	133

6.3. Fatigue Life Characterisation	134
6.3.1. Fatigue Data.....	135
6.3.2. Fracture Surfaces of the LST, Parent and RFW specimens...	139
6.4. Summary	142
Chapter 7. Conclusion and Future work	143
References.....	149
Appendix A: Laser source characteristics and focus position graph	157
Appendix B: Friction weld upset verification and analysis.....	159
Appendix C: Macrograph of different energy input levels.....	160
Appendix D: EBSD results of the RFW specimen.....	173
Appendix E: Fatigue Fracture Surfaces	175

List of Figures

Figure 2-1: Specific strength versus temperature of selected materials [6]....	8
Figure 2-2: Crystal structures at atomic level a) Hexagonal, closed packed b) Cubic, body centred [7].	9
Figure 2-3: Applications of titanium and its alloys in aeroplanes (Airbus A380) [14].....	10
Figure 2-4: Effect of cooling rate on the microstructure of Ti6Al4V a) α' + β ; prior beta grain boundaries b) Primary α and α' + β c) Primary α and α' + β d) Primary α and metastable β e) Acicular α + β ; prior beta grain boundaries f) Primary α and acicular α + β g) Primary α + β h) Primary α and β i) Equiaxed α and intergranular β j) Equiaxed α and intergranular β k) Equiaxed α and intergranular β l) Equiaxed α and intergranular β [7].....	11
Figure 2-5: Equiaxed Ti-6Al-4V microstructure a) Optical microscope image and b) EBSD image [15, 18].	12
Figure 2-6: Influence of slip length (α colony size) on mechanical properties, (schematically) [20]	13
Figure 2-7: α -lamella with different cooling rates a) air cooled (1 °C/min), b) Furnace cooled 100 °C/min, c) Quenched (8000 °C/min) [20].	13
Figure 2-8: Influence of slip length (α colony size) on mechanical properties, (schematically) [20].	14

List of Figures

Figure 2-9: Bimodal microstructure in Ti-6Al-4V [21].	14
Figure 2-10: Processing route for bimodal microstructures, (schematically) [21].	15
Figure 2-11: Friction Stir Welding schematic [29].	16
Figure 2-12: EBSD phase maps (α -blue: β -red) of 500 rpm and 120 mm/min (500 J/mm); HAZ and Weld Nugget [30].	17
Figure 2-13: Friction Hydro Pillar Processing schematic [33].	18
Figure 2-14: RFW process schematic [24].	19
Figure 2-15: Definition of stages on the friction torque curve of RFW [34].	19
Figure 2-16: Micro image of a RFW Ti-6Al-4V joint [5].	20
Figure 2-17: SN curve [39].	23
Figure 2-18: Fatigue loadings and the type of fracture surfaces [39].	23
Figure 2-19: Fracture surface of a constant amplitude specimen a) full fracture surface b) crack initiation site c) high spots [5].	25
Figure 2-20: SN curve for different conditions of Ti-6Al-4V [48].	26
Figure 2-21: Principle of Bragg's law [52].	28
Figure 2-22: Longitudinal (top) and transverse (bottom) residual stress profiles of Ti-6Al-4V FSW joints [59].	31
Figure 2-23: Stress relief versus time of Ti-6Al-4V [59].	32
Figure 2-24: Coherent and incoherent light [75].	33
Figure 2-25: Different laser processing techniques [63, 64].	34
Figure 2-26: Laser surface treatment/engineering process [64].	36
Figure 2-27: Top view and cross sectional micrograph of laser modified Ti-6Al-4V [69].	36
Figure 2-28: Microstructure of Ti-6Al-4V after laser surface treatment at a) 800, b) 1200, and c) 1500 W powers [71].	37
Figure 2-29: Microstructure appearance [71].	38
Figure 2-30: Focus position a), beam into the material, b) beam on the work piece surface, c) beam defocussed.	39
Figure 2-31: An example of 50% overlap in a) seam welding b) LST using a pulsed laser.	41
Figure 3-1: Weldcore III Friction Processing platform.	45
Figure 3-2: Laser Kuka robot.	46

List of Figures

Figure 3-3: Laser welding head.....	46
Figure 3-4: Temperature point amplifier.....	47
Figure 3-5 Rotating bending fatigue machine.	48
Figure 3-6: Load verification on the PUNZ.....	49
Figure 3-7: Calibration curve.....	50
Figure 3-8: RFW set-up.	53
Figure 3-9: Stud design for RFW process.....	53
Figure 3-10: A torque curve of RFW Ti-6Al-4V ELI.....	55
Figure 3-11: Example of the RFW weld upset process feedback data analysis.	56
Figure 4-1: LST development methodology.	58
Figure 4-2: Schematic of LST of 3 mm Ti-6Al-4V sheets.	60
Figure 4-3: Results of first stage analysis.	61
Figure 4-4: Results of first stage analysis (continued).	62
Figure 4-5: Analysis of focus position vs depth of penetration.	63
Figure 4-6: Analysis of focus position vs width.	64
Figure 4-7: 2000 W and 3000 W results	65
Figure 4-8: Hardness indentations map.	65
Figure 4-9: Hardness of LST specimens at 1000 W and 0 mm focus position (parallel and perpendicular to the surface).....	66
Figure 4-10: Micro hardness profiles of the 1000 W LST specimens at different focus positions.	67
Figure 4-11: Micro Vickers hardness profiles of the 2000 W LST specimens at different focus positions.	67
Figure 4-12: Ti-6Al-4V parent microstructure (Polarised light).	68
Figure 4-13: Attained microstructure for LST specimen power; 1000 W and focus position, 0 mm.	69
Figure 4-14: Weld experimental set-up.	71
Figure 4-15: LST strategy 1 a) profile followed on the specimen b) expected cross section of LST strategy 1.....	72
Figure 4-16: LST visual images of 675 W and 1000 W specimen.....	72
Figure 4-17: LST 1 (675 W, red arrow shows treatment direction).....	73
Figure 4-18: LST 2 (1000 W, red arrow shows treatment direction).....	74

List of Figures

Figure 4-19: LST 1000 W microstructural analysis showing effect of continuous LST strategy and difference between the needles in the colonies.	75
Figure 4-20: LST strategy 2 non- continuous scan (from 1 to 2, 3, etc.).	76
Figure 4-21: Visual image of LST specimens	77
Figure 4-22: Effect of LST strategies on depth of penetration.....	78
Figure 4-23: LST depth of penetration measurements on cross section analysis.....	79
Figure 4-24: LST process development schematic.....	81
Figure 4-25: Hole position for thermocouple inserted in the specimen undergoing LST processing.	84
Figure 4-26: From RFW to final LST specimen.....	85
Figure 4-27: LST process for the final matrix.	86
Figure 4-28: Repeated experimental runs.....	88
Figure 4-29: Profile plot of temperature vs scanning speed.....	90
Figure 4-30: Profile plot of temperature vs laser power.	90
Figure 4-31: Profile plot of temperature vs focus position.	91
Figure 4-32: Illustration of the selection process for the final analysis.	93
Figure 4-33: Examples of random visual images of the final matrix, a) example of full specimen, b) low energy input (LST 4), c) medium energy input (LST 1) and c) high energy input (LST 7).....	93
Figure 4-34: Two LST specimens at different scanning speeds a)102 mm/s b) 75 mm/s.	94
Figure 4-35: Example of perpendicular cross section used for analysis.	95
Figure 4-36: A comparison of energy input versus LST depth of penetration.	98
Figure 4-37: Power density vs LST depth of penetration at constant energy input.	99
Figure 4-38: Hardness profiles across the LST specimen's centre.....	100
Figure 5-1: EBSD analysis position.....	107
Figure 5-2: Parent material microstructure (Band Contrast with Grain Boundaries).....	109
Figure 5-3: EBSD phase maps (α -red: β -blue).....	109

List of Figures

Figure 5-4: Band Contrast: weld zone, HAZ to parent microstructural evolution.	111
Figure 5-5: Band Contrast Euler contrast: weld zone, HAZ to parent microstructural evolution.	111
Figure 5-6: Phase map: weld zone, HAZ to parent microstructural evolution.	111
Figure 5-7: RFW weld interface microstructure band contrast + sub grains (red).	112
Figure 5-8: Phase maps at position two (α -red and β -blue).	113
Figure 5-9: All Euler plots of LST specimens at position 1, 200 μm showing the difference in the colonies and lamella size a) low b) high.	114
Figure 5-10: Microstructure evolution of low-power density specimen a). 200 μm b). 800 μm positions.	114
Figure 5-11: Microstructure at 800 μm for a) low (a_0 – enlarged area IPF plot and a_1 – small zoomed in area) and b) high (a_0 – enlarged area IPF plot and a_1 – small zoomed in area).	116
Figure 5-12: Position of hardness indentation.	117
Figure 5-13: Hardness analysis for the three specimens. (Two circles highlighting position of the HAZ)	117
Figure 6-1: Specimens to be analysed by synchrotron X-ray diffraction. ...	122
Figure 6-2: Illustration of the ID15A beam at the ESRF [77].	123
Figure 6-3: Depiction of the synchrotron X-ray diffraction specimens mounted on the specimen holder before testing commenced.	124
Figure 6-4: Schematic illustrating residual strain measurement positions..	124
Figure 6-5: Residual stress profile: Axial.	127
Figure 6-6: Axial residual stress analysis.	128
Figure 6-7: Residual stress profile: Radial stress.	130
Figure 6-8: Radial residual stress analysis.	131
Figure 6-9: Residual stress analysis: Hoop stress close to the surface only.	132
Figure 6-10: Fatigue specimen dimensions (all dimensions in mm).	135
Figure 6-11: Fatigue life plot of the parent, RFW and LST specimens.	137

List of Figures

Figure 6-12: Example of the failure position after cross section the half fractured fatigue specimen a) RFW fatigue specimens and b) friction welded LST processed fatigue specimens. 138

Figure 6-13: Examples of fatigue fracture surfaces (Additional fracture surfaces are shown in Appendix E)..... 139

Figure 6-14: Crack initiation site with evidence of striations for LST fracture surface at a stress of 502 MPa (45 000 cycles). 141

List of Tables

Table 2-1: Comparison of residual stress measurement techniques [50]. ...	27
Table 2-2: Effect of residual stresses [55].	29
Table 3-1: Chemical composition specification % wrt.	44
Table 3-2: Weldcore III platform capabilities.	45
Table 3-3: Strain measurements vs sliding weight movement.	50
Table 3-4: The fatigue specimen preparation polishing sequence.	51
Table 3-5: Input RFW process parameters.	54
Table 4-1: First stage analysis: 3 mm Ti-6Al-4V.	60
Table 4-2: Hardness (start and finish) 0.125 mm from the outer edge of the specimen.	79
Table 4-3: Experimental domain star points.	82
Table 4-4: Final experimental matrix showing the varied process parameters.	83
Table 4-5: Measured temperature for each experimental run.	87
Table 4-6: Model results after regression analysis.	89
Table 4-7: Macrographs of the three different energy input levels.	96
Table 4-8: Average LST depth of penetration.	97
Table 4-9: Medium Energy Input LST depth of penetration analysis.	99
Table 4-10: Summary of the 3 selection criteria at different energy inputs.	102
Table 4-11: Selected LST specimens for further analysis.	103
Table 6-1: Specimens analysed by synchrotron X-ray diffraction.	122
Table 6-2: A summary of the axial residual stresses results.	127
Table 6-3: A summary of the radial residual stress results.	130
Table 6-4: Parent material fatigue test results.	135
Table 6-5: RFW fatigue results.	136
Table 6-6: LST low-power density specimen fatigue results.	136
Table 6-7: LST High-power density specimen fatigue results.	136

Abstract

Influence of Laser Surface Treatment on Residual Stress Distribution and Dynamic Properties in Rotary Friction Welded Ti-6Al-4V components

D.S. Tsikayi

Faculty of Engineering, the Built Environment and Information Technology

Nelson Mandela University

PO Box 77000, Port Elizabeth, South Africa

Thesis for Doctor of Philosophy: Engineering Mechanical

April 2019

This manuscript details a study on laser surface treatment, a surface modification technique that is an easily flexible way of improving material surface properties of complex geometries. The research explored the potential of laser surface modification/treatment as a post welding surface processing technique for RFW Ti-6Al-4V ELI components by evaluating the microstructural effects, influence on fatigue life and the depth and magnitude of residual stresses induced. The outcome of this study reveals how post processing by laser surface modification affects crack initiation hence fatigue life and further explains mechanisms potentially contributing to enhanced joint properties.

This study was accomplished by investigating the effect of laser surface treatment on surface properties of hourglass cylindrical rotary friction welded Ti-6Al-4V ELI specimens. Preliminary work was done in two stages. The first stage involved conducting laser surface treatment on 3 mm Ti-6Al-4V sheets. In this stage, an understanding of the process variables concerning the laser surface treatment process characteristics was established. Laser power and focus position were varied whilst scanning speed was kept constant. The observed macrographs were quantified in terms of laser penetration depth and width. A hardness and microstructural analysis was also conducted on

selected specimens of the laser surface treated flat sheets trials. The second stage involved surface treatment of the hourglass fatigue specimen. This preliminary work allowed for the type and influence of treatment strategy to be analysed. The influence of treatment strategy on the depth of penetration was established with an emphasis on achieving homogeneity of the laser surface treated zone's depth of penetration around the complete cylindrical specimen's diameter.

The final matrix involved varying laser power, scanning speed and focus position and the specimens were characterised by comparing hardness, residual stresses and microstructure. The results showed that laser surface treatment changed the hardness profile of the near surface of the specimen owing to the introduction of a homogenous microstructure at the surface as compared to a friction welded specimen.

The microstructure was resolved using electron backscatter diffraction. A fully α -lamella microstructure was observed in the two specimens analysed at a position of 200 μm from the surface. The α -lamella had different width sizes with the low-power density specimen having a very fine microstructure as compared to that of the high-power density specimen. EBSD phase maps were also analysed for the parent, rotary friction welded only and friction welded laser surface treated specimens. The laser treated specimens showed virtually no β phase present as compared to the parent and rotary friction welded only specimens.

LST processing improved the fatigue properties of the RFW specimens. The position of failure shifted from the HAZ to outside the RFW joint. This change in position was attributed to the surface modification by LST thereby introducing a more homogenous microstructure at the surface of the specimen. Additionally, it was also observed that the power density had an important role to play in the fatigue properties of the laser surface treated specimens. The high-power density LST specimens had a low fatigue limit compared to the low-power density specimens. The low fatigue limit at high-

power density correlated with the residual stress results where the high-power density specimen had the highest attained surface tensile axial residual stresses.

In conclusion, the main influences of laser surface treatment of small friction welded Ti-6Al-4V ELI components relate to an increase in fatigue properties by shifting crack initiation sites to less stressed areas. In this way, laser surface treatment could assist in the optimisation of manufacturing methodologies for small near net shape complex geometry components. The uniform and homogenous microstructure eliminates or reduces microstructural variations as observed in as welded components, reducing weld zone hardness variation. Additionally, the study showed that the introduction of a near surface refined microstructure inhibited crack initiation in the welded region.

Keywords: Laser Surface Treatment, Rotary Friction Welding, Electron Backscatter Diffraction, Fatigue, Residual stress, Microstructure.

List of Abbreviations

ASTM	American Society for Testing and Materials
AWS	American Welding Society
EBS	Electron Backscatter Diffraction
EDXRD	Energy Dispersive Synchrotron X-ray diffraction
ELI	Extra Low Interstitials
FP	Friction Processing
FHPP	Friction Hydro Pillar Processing
FW	Friction Welding
FPn	Focus Position
FSW	Friction Stir Welding
FTPW	Friction Taper Plug Welding
FTSW	Friction Taper Stud Welding
HAZ	Heat Affected Zone
HCF	High Cycle Fatigue
LASER	Light Amplification by Stimulated Emission of Radiation
LMP	Laser Materials Processing

List of Abbreviations

LSA	Laser Surface Alloying
LSH	Laser Surface Hardening
LSM	Laser Surface Melting
LST	Laser Surface Treatment
HAZ	Heat Affected Zone
HMI	Human Machine Interface
Pd	Power Density
RFW	Rotary Friction Welding
SEM	Scanning Electron Microscope
SS	Scanning Speed
SN	Stress Cycles
TWI	The Welding Institute
UNSM	Ultrasonic Nanocrystal Surface Modification

Nomenclature

keV Kilo electron volt

Kt Stress concentration factor

σ Stress

σ_a Axial stress

σ_θ Tangential stress

σ_r Radial stress

λ Wavelength of the beam

D Distance between the lattice planes inside the material

R Stress ratio

N Number of cycles

Nf Number of cycles to failure

n Order of diffraction

$\hat{\sigma}$ Variance

θ Angle of diffracted beam

E Young's Modulus

ε Strain

Nomenclature

ε_a Axial strain

B Bending

rpm Revolutions per minute

m Mass

Ra Average surface roughness

ν Poisson's ratio of the material

Glossary of Terms

A

Alloy: A substance with metallic properties composed of two or more chemical elements, both a metal.

Alloying element: An element added to a metal, which remains in it and changes its structure and properties.

Alpha, α : The low temperature allotrope of Titanium with a hexagonal close packed crystal structure, occurring below β -transus.

Alpha stabilizer: An alloying element that dissolves preferentially in α phase and that raises the α - β transus temperature.

Alpha-Beta Structure, α - β : A microstructure containing both α and β as the principle phase.

Annealing: Heating and holding at a suitable temperature, followed by cooling at a suitable rate to produce the desired properties and microstructure.

B

Beta, β : The high-temperature allotrope of Titanium with a body-centred crystal structure, which occurs above β -transus.

Beta stabilizer: An alloying element that dissolves preferentially in β phase and that lowers the α - β transformation temperature without eutectoid reaction.

β -Structure: Structurally analogous body-centred cubic phase.

β -Transus: The minimum temperature above which equilibrium α does not exist.

Brittle fracture: Rapid fracture preceded by little or no deformation.

Braking phase: Sudden increase in torque response as rotation of consumable tool slows from welding speed to stop.

C

Consumable tool: The tool used in specific friction welding processes that is rotated against a work piece or inside a hole. The tool material is deposited and bonds to the parent material.

Coherent: Waves of one wave length all in phase.

Cold-worked structure: Microstructure resulting from plastic deformation of material below its recrystallization temperature.

Cooling rate: Time taken for the risen temperature to drop at specific intervals.

D

Deformation: Change in the form of a body due to heat, stress or other sources of heat.

Defect: A discontinuity that has an accumulative effect on a part or material, preventing the material from meeting the minimum applicable standard or specification.

Down or axial force: The force applied to the Friction Processing tool during the welding process in the direction of the axis of rotation of the tool. Also referred to as the z-direction force or z-force on the FP platform.

E

Equiaxed grain structure: A structure in which the grains have approximately the same dimensions in all directions.

Etchant: A chemical solution used to etch a metal to reveal structure details.

F

Faying surface: The mating surface of a member that is in contact with another member to which it is to be joined.

Fatigue: Localised progressive damage of a material, which can lead to failure under cyclic loading.

Fatigue life: The number of load cycles a component can withstand prior to fatigue failure.

Flash: The material that is displaced from the friction weld interface.

Flash formation: Excess plasticised material ejected during friction processing.

Forging force: A compressive force applied to the faying surfaces after the friction phase of the welding cycle is completed.

Fractography – The study of fracture surfaces.

Friction Hydro Pillar Processing: Friction welding process whereby a consumable tool or stud is rotated concentrically inside a blind hole under an axial load thereby filling the hole and creating a strong bond with the parent plate.

Friction Stir Welding: Solid state welding process whereby abutting parts are joined together by rotating a non-consumable tool along the interface.

Friction Taper Stud Welding: Solid state welding process used to join similar or dissimilar material by rotating a tapered consumable rod co-axially in a taper-sided cavity, of equal or slightly larger included angle than the tool, whilst under an applied load so as to generate a plasticised layer thereby forming a bond.

Fusion welding: A process in which materials are melted together by applying heat to form a bond.

G

Grain: An individual crystal in a polycrystalline metal or alloy, including twinned regions or sub-grains, if present.

H

Hardness: A term used for describing the resistance of a material to plastic deformation under the action of an indenter.

Heat affected zone (HAZ): The area of the base metal in which the structure/properties have been affected due to the heat produced during welding.

High-temperature material: A metal or alloy which can operate at temperatures above 540° C.

Hot working: Deformation under conditions that results in material recrystallization.

M

Macrograph: A graphic reproduction of a prepared surface of a specimen at a magnification not exceeding 10x.

Macrostructure: The structure of metals as revealed by macroscopic examination of the etched surface of a polished specimen.

Martensitic: Microstructure formed by diffusionless phase transformation in which the parent and product have a specific crystallographic relation.

Matrix: The continuous or principal phase in which another constituent is dispersed.

Micrograph: A graphic reproduction of the prepared surface of a specimen at a magnification greater than 10x.

Microstructure: The structure of a prepared surface of a metal as revealed by a microscope at a magnification exceeding 10x.

Micro Vickers hardness test: A static test in which an indenter is pushed into the surface of a material with a specified force, applied for a specified time. The resulting diagonals are measured and referenced to appropriate hardness value according to international standards.

O

Oxidation: The addition of oxygen to a compound.

P

Parent material: Pertains to material in its as-manufactured form and condition.

Plastic deformation: Deformation that remains or will remain permanent after release of the driving stress that caused it.

Plasticised material: Material that is displaced when its yield strength is exceeded and cannot return to its original form.

P-value: The level of marginal significance within a statistical hypothesis representing the probability of the occurrence of a given event

R

Recrystallization: The change from a crystal structure to another structure due to heating or cooling through a critical temperature.

Residual stress: Stress inherent in the material that exists because of the processing history.

Rolling direction: The direction in which the material was rolled during manufacture.

S

Scanning electron microscope (SEM): An electron microscope in which the image is formed by a beam operating in synchronism with an electron probe scanning the object.

Solid state welding: A process whereby materials are joined together by plasticisation and pressure below melting temperature to form a bond.

Strain hardening: An increase in hardness and strength caused by plastic deformation at temperatures below the recrystallization range.

Stress: Load applied to a material to cause deformation that is resisted by internal forces within the material.

Stress ratio (R): The ratio during cyclic fatigue loading as minimum stress divided by maximum stress.

Solid state welding: A group of welding processes which produce coalescence at temperatures essentially below the melting point of the materials being joined.

Spindle speed: The speed of the tool holding device (chuck), measured in revolutions per minute (rpm).

T

Torque stages: The trends of torque responses which are a measure of the resistance to rotation and have identifiable phases.

Tool rotational speed: The rotary speed of the tool, which can be quoted as rotation speed (rpm), peripheral velocity (m/s), or angular velocity (rad/s).

U

Upset: Bulk deformation resulting from the application of pressure in friction welding. It is measured as a percentage increase in interface area or as a reduction in length.

Upset distance: The total loss of axial length of the work pieces from the initial contact to the completion of the weld. Can be separated into the upset during friction phase, friction upset and the upset during the forge phase, forge upset.

UTS – Maximum tensile stress reached achieved during a tensile test.

V

Void: Space that exists between grains and particles of a microstructure, normally a defect in Friction welding.

W

Welding: A process of joining in which materials are allowed to form a metallurgical bond under the action of heat and pressure.

Chapter 1. Project Overview

1.1. Background

Titanium and its alloys are high strength, low weight and corrosion resistant materials, which makes them attractive for the aerospace and medical industries. Ti-6Al-4V alloy is the workhorse of the aerospace industry but the cost of manufacturing Ti-6Al-4V components is expensive due to the complexity of components being manufactured. Friction processing or welding, an advanced joining technique, provides an alternative manufacturing method with the potential to join complex Ti-6Al-4V near net shape components enabling a reduction in manufacturing costs. The Welding Institute (TWI) termed friction welding as a solid-state welding process due to the process being performed at the plasticisation temperature [1, 2].

Friction welding is a process that involves frictional heat being generated by rotating or moving work pieces relative to each other under an axial force. The rubbing of the faying or contacting surfaces generates the frictional heat leading to the plasticisation of material. The plasticised material is displaced from the rubbing or faying surfaces. The plasticised material mixes and some of the material is expelled as flash. As the spindle rotation is abruptly stopped, a forging force is applied to allow for the consolidation of the plasticised material whilst it cools [2].

Preliminary studies performed at the Nelson Mandela University have shown that small high value Ti-6Al-4V extra low interstitials (ELI) components can be successfully welded through friction welding. At the joining surfaces, at least two zones are introduced by the friction welding of Ti-6Al-4V ELI components. The two zones typically have different hardness and microstructure properties when compared to each other and to the parent base material.

Surface treatment or modification techniques are the most effective methods to combat crack initiation. Owing to the need to improve metallurgical and mechanical properties, key industries have looked at material surface improvement by means of laser surface treatment (LST) [3]. LST has been used to improve the surface properties of materials. LST is able to enhance surface dependent properties, for example: hardness, friction, resistance to wear, fatigue and corrosion resistance. Globally, automatic and robotic high-powered lasers have the ability to perform surface treatments on specific areas of interest without affecting the bulk material of a component. These automated robots can be easily integrated into production lines for the purpose of laser surface treatment [3].

Therefore, a thermal post-processing technique, laser surface treatment, is envisaged to help improve the surface properties of the friction welded components. By LST processing, a homogenous and uniform thin surface layer will be introduced aiding in the reduction of microstructural and hardness variation in the friction welded Ti-6Al-4V ELI joints. The study will also analyse the role of residual stress before and after laser surface treatment of the friction welded joints. Currently, the proposed technique, laser surface treatment (LST) is classified into two categories which are thermal and thermo-chemical processes respectively. For this research, the focus is on a thermal process. Thermal processing does not change the chemical composition of the material, unlike thermo-chemical processes i.e., cladding, nitriding and alloying [3, 4]. Examples of thermal LST processes are laser tempering, annealing, melting and phase transformation.

1.2. Research Question

In what way will laser surface treatment influence fatigue life and how does this relate to weld microstructure and distribution of residual stresses in small cylindrical Rotary Friction Welded Ti-6Al-4V ELI components?

1.3. Problem Statement

Most frequently, failure of welded engineering components occurs because of high residual tensile stresses at the surface or around notches. When components are welded, surface tensile residual stresses, arising from plastic mismatch due to the temperature gradient, can accelerate the initiation of fatigue cracks during dynamic testing. Preliminary work has shown that Ti-6Al-4V ELI can be successfully welded with high integrity through RFW, but cracks initiate from the surface [5]. This research will study the effect of laser surface treatment in the modification of surface dependent properties in components exposed to dynamic loading, thereby improving the integrity of Ti-6Al-4V ELI components for medical and aerospace applications.

1.3.1. Sub-problems

The challenges associated with this research work are detailed as follows:

- Establish a strategy for laser surface treatment of cylindrical hourglass specimens.
- Develop an experimental design matrix of laser surface treatment RFW joints to determine the influence of the different LST process parameters and characterise the LST specimens through fatigue, microstructure, and hardness and '*through-depth*' residual stress measurement.
- Quantify the effect of laser surface treatment on Ti-6Al-4V ELI RFW joints by relating residual stresses, fatigue life and microstructure.

1.4. Objective

The objective of this research is to investigate the potential of laser surface treatment as a post-processing technique for RFW Ti-6Al-4V ELI components by relating fatigue, residual stresses and microstructure.

1.5. Hypothesis

The integrity of rotary friction welded joints can be improved by introducing laser surface treatment. The research will further unlock the mechanisms contributing to enhanced mechanical properties by linking interactions of different property changes.

1.6. Significance and Feasibility of Research

Since most engineering components are subjected to dynamic loading environments, the present study proposes to create knowledge that will assist in understanding the influence of laser surface treatment on the dynamic and static behavior of small rotary friction welded Ti-6Al-4V ELI components.

The research study outcomes will thus expand the existing knowledge on RFW and laser surface treatment of Ti-6Al-4V ELI, whilst contributing to understanding FP dynamics in relation to laser processing and fatigue properties of Ti-6Al-4V ELI rods. The outcomes of this research will continue to establish Nelson Mandela University as a leader in the field of solid state welding, both locally and internationally. The knowledge generated will further assist in unlocking new advanced manufacturing opportunities with respect to the manufacturing of near-net-shape Ti-6Al-4V ELI components.

1.7. Delimitations

The material utilised for this research will be Ti-6Al-4V ELI and the geometry of the samples tested will be hourglass in shape. Rotating bending fatigue at stress ratio $R = -1$ will be used during dynamic testing.

The study does not include laser shock-peening in the experimental matrix.

1.8. Research Methodology

Resulting from a comprehensive literature review of the knowledge gap, the following steps to be undertaken are detailed below:

- Determine the process limits of the laser source housed at the Nelson Mandela University.
- Conduct a trial experimental matrix to determine the effect of different laser surface engineering process parameters by conducting LST trials on flat sheet specimens.
- Develop a laser surface treatment strategy for the hourglass specimens.
- Develop a matrix to quantify the effect of laser process parameters i.e., laser power, scanning speed and focus position. The objective of this matrix will be to establish a relationship between each of these process parameters, therefore bridging the existing gap in specifically the LST RFW of small Ti-6Al-4V rods.
- Characterise the effect of LST on rotary friction welded Ti-6Al-4V ELI joints through fatigue and hardness tests, microstructure analysis and residual stress measurement (surface and through).
- Characterise the fatigue fracture surfaces, identify crack initiation sites and determine the number of cycles required to initiate a crack.

1.9. Organisation of Thesis

The thesis is structured as follows:

Chapter 1 introduces rotary friction welding and laser surface treatment as applied to Ti-6Al-4V ELI diameter 6 mm. Furthermore, the chapter details the research question, problem statement, the hypothesis and describes the research methodology of the study.

Chapter 2 introduces a review of relevant literature pertaining to the study. The fundamentals of titanium and its alloys as well as RFW and LST processing are considered in this chapter. Emphasis is placed on an understanding of the influence of microstructure and residual stress on fatigue performance of titanium and its alloys.

Chapter 3 covers the material, platforms and the mechanical and metallurgical techniques utilised for this research. The type of mechanical testing methods utilised are expounded on in this chapter. The RFW process and verification process are also presented.

Chapter 4 presents the LST developmental process. The developmental process demonstrates experimentally that the process of LST can be used to substantially modify microstructural characteristics of Ti-6Al-4V ELI specimens. A full experimental study that forms the bulk of the research follows an initial LST developmental process.

Chapter 5 presents the results of the final matrix which includes the characterisation of the laser processed area, microstructure and fatigue performance of the RFW Ti-6Al-4V ELI specimens. Electron Backscatter Diffraction (EBSD) was used to resolve the microstructure.

Chapter 6 analyses the depth residual stresses distribution and fatigue properties. Synchrotron X-ray diffraction is used to quantify the effect of residual stresses on the LST specimens. Dynamic performance is established through a series of fatigue tests, quantifying the effect of LST processing.

In Chapter 7, the conclusions resulting from the study are presented together with ideas outlining possible future studies.

Chapter 2. Literature Review

2.1. Introduction

The literature review section details relevant literature on the fundamental aspects covered in this study. This section seeks to build an understanding of how laser surface treatment can be used as a post-processing technique to improve the surface-dependent properties of RFW components. Surface properties and microstructural evolution arising from both the processes of LST and RFW respectively are quantified. Literature relating to Ti-6Al-4V and the friction welding of Ti-6Al-4V is also discussed in this section.

2.2. Ti-6Al-4V Alloy

Titanium was discovered in 1791 by William Gregor, a reverend, chemist and mineralogist. Titanium is named after the Titans, the powerful children of the supreme rulers of the Universe in Greek mythology, Uranus and Gaia. Purification of titanium only started in the early 1900s by Wilhelm Justin Kroll from Luxembourg, who is regarded as the father of the titanium industry. Titanium ranks as the ninth most plentiful element and the fourth most abundant structural metal in the Earth's crust, exceeded only by aluminium, iron, and magnesium [6]. The American Government funded research on titanium as a strategic metal for use in the aerospace industry for spacecraft and missile manufacture in the 1960s. In 1964, the Lockheed's SR-71 Blackbird spy plane, predominantly made of titanium, was first flown with at least 93% of its parts, being machined from titanium [7].

Titanium is a high strength, low weight and corrosion resistant material. These properties of titanium and its alloys make it acceptable for use in a wide range of applications which include the following [8]:

- Aerospace industries, i.e. in engines because of high temperature resistance.
- Marine industries because of its high corrosive resistance.
- Chemical and biomedical applications.
- Sports equipment because it is lightweight.
- Power generation and nuclear waste storage.
- Medical implants because of biocompatibility.

The main advantage of using titanium and its alloys is that it has a high specific strength compared at elevated temperatures. Figure 2-1 shows specific strength versus temperature of titanium, Carbon Fibre Reinforced Plastics (CFRP) and selected materials [6]. Titanium applications have increased with each new generation of commercial aeroplanes. The Boeing 777 used titanium alloys in areas that had previously used CFRP structures because of the need to minimise galvanic corrosion on metals connected to the CFRP [6].

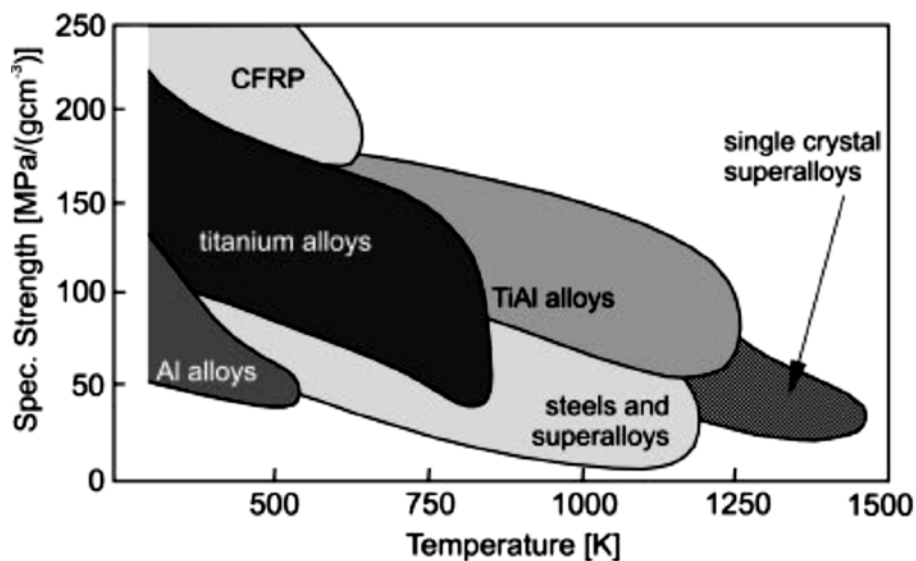


Figure 2-1: Specific strength versus temperature of selected materials [6].

Titanium and its alloys can be divided into four classes which are alpha, near alpha, alpha + beta, and beta. From these four classes, titanium and its alloys were further grouped into grades as defined by the ASTM standards and

ASME codes. Commercially pure titanium grades are alpha in structure whilst titanium alloys have two structures alpha and beta. The majority of the grades are alloys, with alloying elements, for example, aluminium, vanadium and molybdenum. These alloying elements improve certain mechanical characteristics to better suit different applications [8-12].

The most common type of titanium alloy is grade 5, Ti-6Al-4V. It consists mainly of the alpha (α) and beta phase (β). The $\alpha + \beta$ phase in Ti-6Al-4V means that the structure is a mixture of the hexagonal closed packed (α) and body centred cubic structures (refer to Figure 2-2). It experiences an allotropic transformation at approximately 900 °C, whilst it has a melting temperature in excess of 1660 °C. Ti-6Al-4V has a chemical composition of (wrt. %) Al 6, V 4.04, Fe 0.19, N 0.018, O 0.18 and remaining Ti. The alpha stabilisers are Al, O and N while Fe is a beta stabiliser. Ti-6Al-4V alloy can easily be fabricated allowing the mill products to be made into different shapes [8-13].

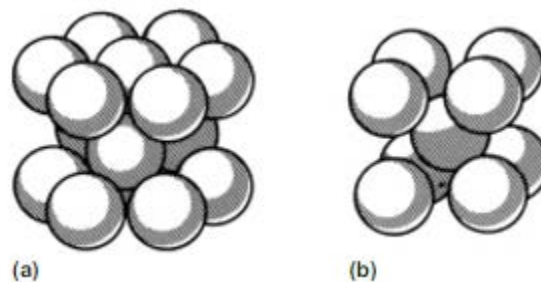


Figure 2-2: Crystal structures at atomic level a) Hexagonal, closed packed b) Cubic, body centred [7].

Ti-6Al-4V is the metal of choice for the highly stressed wing sections as well as the fuselage-wing connections on aeroplanes and jet engines because of its high strength to weight ratio properties [8]. Figure 2-3 shows applications of Ti-6Al-4V in the aerospace industry.

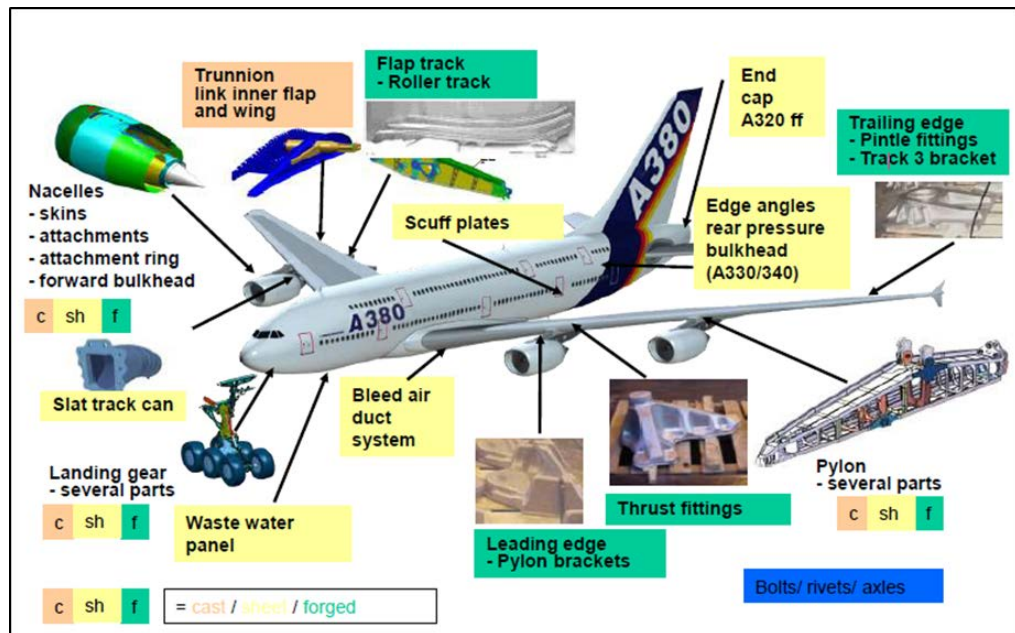


Figure 2-3: Applications of titanium and its alloys in aeroplanes (Airbus A380) [14].

Ti-6Al-4V ELI, grade 23, is similar to Ti-6Al-4V but has reduced levels of oxygen, nitrogen, carbon and iron. ELI is an acronym for “Extra Low Interstitials” with the interstitials improving its ductility and fracture toughness as compared to Ti-6Al-4V. In Ti-6Al-4V ELI, the interstitials content, oxygen, nitrogen, carbon and iron should not exceed 0.13 %, 0.08 %, 0.05 % and 0.25 % respectively. The Boeing 777, used beta-annealed Ti-6Al-4V ELI material for damage tolerant components, for example, the critical fittings in the fuselage. Additionally, it is used in the medical industry, mainly in surgical procedures, for example, as material for bone fixation devices, hip replacements, orthopaedic cables, pins and screws [6, 15].

Figure 2-4 from the Titanium ASM handbook shows the effect of cooling rate on microstructure development in Ti-6Al-4V. In the processing or heat treatment of Ti-6Al-4V, the formation of different Ti-6Al-4V alloy microstructures is closely related to cooling rates with reference to the beta transus temperature of 955 degrees Celsius. There are three distinctive microstructures of $\alpha + \beta$ titanium alloys that can be achieved by varying thermal treatments and cooling rates, which are Equiaxed (globular) fully lamella and bimodal (duplex) [12, 15, 16].

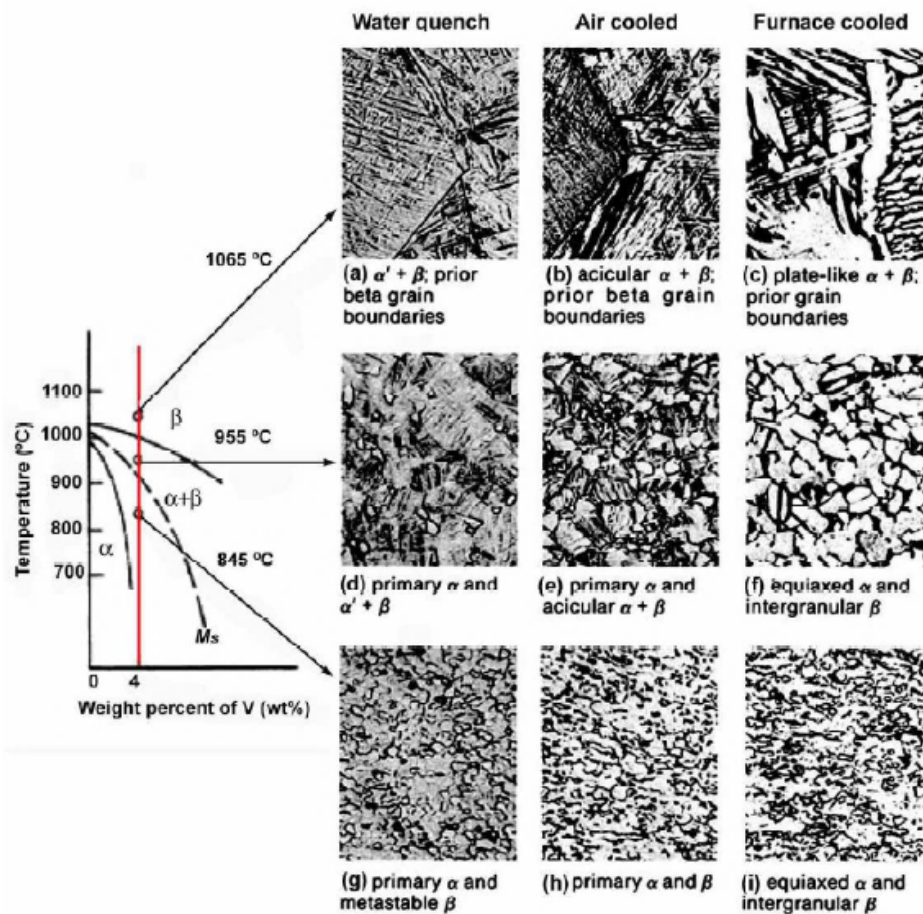


Figure 2-4: Effect of cooling rate on the microstructure of Ti6Al4V a) $\alpha' + \beta$; prior beta grain boundaries b) Primary α and $\alpha' + \beta$ c) Primary α and $\alpha' + \beta$ d) Primary α and metastable β e) Acicular $\alpha + \beta$; prior beta grain boundaries f) Primary α and acicular $\alpha + \beta$ g) Primary $\alpha + \beta$ h) Primary α and β i) Equiaxed α and intergranular β j) Equiaxed α and intergranular β k) Equiaxed α and intergranular β [7].

Equiaxed Ti-6Al-4V microstructure consists primarily of α grains with intergranular β phases. The cooling rate after thermal treatment plays an important role in the formation of this microstructure, and when the cooling rate is sufficiently low, no α lamella is present in the formed grains [16, 17]. An equiaxed microstructure is mainly observed at slow cooling rates, for example, furnace cooling allows for the formation of this microstructure. Figure 2-5 shows equiaxed microstructure in Ti-6Al-4V [16, 17].

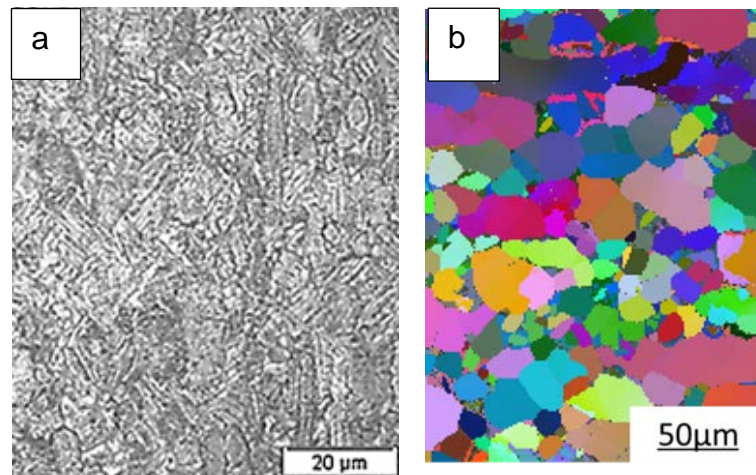


Figure 2-5: Equiaxed Ti-6Al-4V microstructure a) Optical microscope image and b) EBSD image [15, 18].

Lamella or acicular is a microstructure attained by closely controlling cooling rate with transformation occurring above the β -transus temperature. Controlled cooling rate determines the length of the α -colonies and resultant α -lamella width growing from the β grain boundaries [15].

A cluster of acicular or α -lamella aligned in the same orientation plane is called a colony. The α -colony size is the most important characteristic that affects mechanical properties of a fully lamella microstructure. Mechanical properties - namely, fatigue and fracture toughness are greatly influenced by the colony size. The colony size is greatly influenced by cooling rate as shown in Figure 2-6. The colony size determines the effective slip length. An increasing cooling rate effectively decreases colony size and thus decreases slip length which negatively affects mechanical properties. Figure 2-6 also shows the effect of slip length on mechanical properties with increasing α colony size [19, 20].

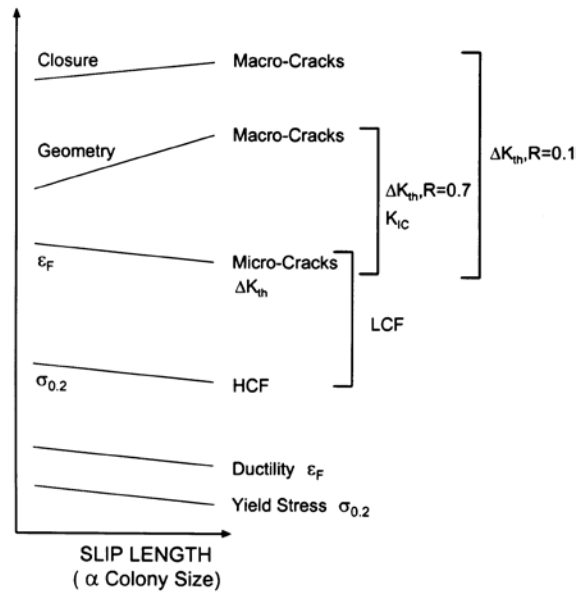


Figure 2-6: Influence of slip length (α colony size) on mechanical properties, (schematically) [20]

According to Gammon et al. [15], as cooling rate increases, the α -lamella becomes finer. At high cooling rates, new colonies also nucleate on the boundaries of other colonies instead of only in the β -phase boundaries. These new colonies grow perpendicular to the lamellae leading to the formation of a basket weave Widmanstätten microstructure. Figure 2-7 shows coarse to fine lamella structures in titanium alloys [15, 19, 20].

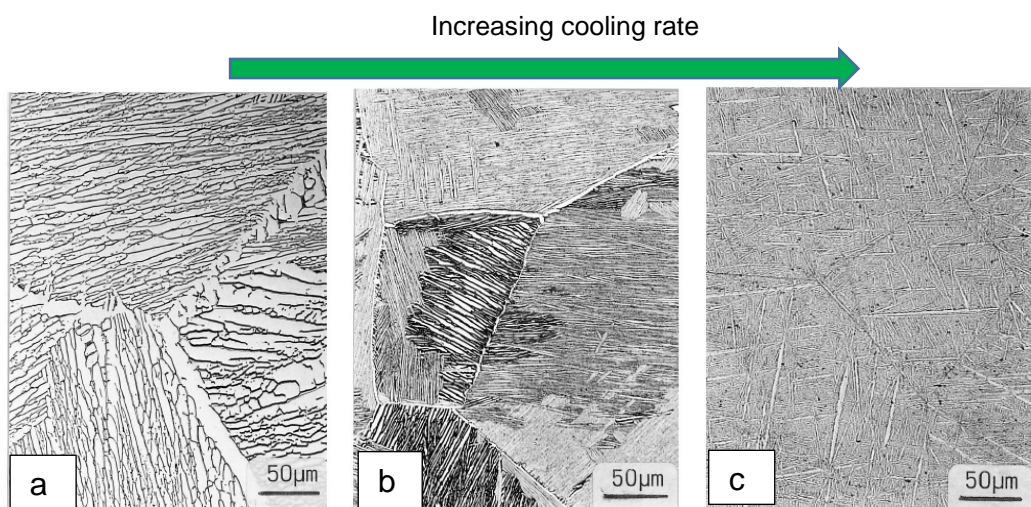


Figure 2-7: α -lamella with different cooling rates a) air cooled ($1\text{ }^{\circ}\text{C}/\text{min}$), b) Furnace cooled $100\text{ }^{\circ}\text{C}/\text{min}$, c) Quenched ($8000\text{ }^{\circ}\text{C}/\text{min}$) [20].

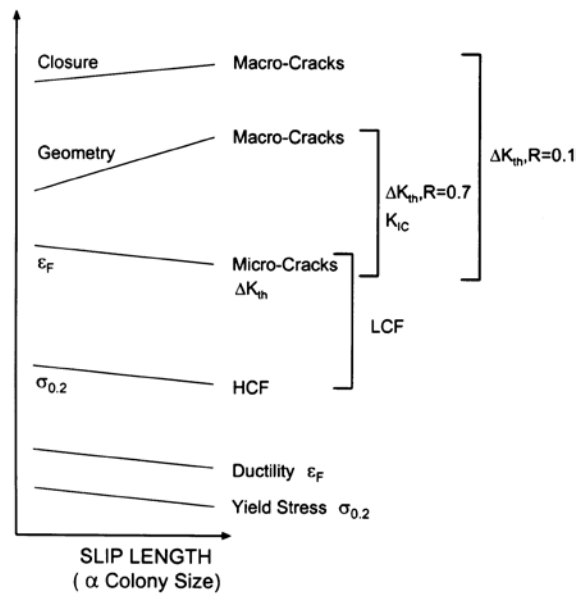


Figure 2-8: Influence of slip length (α colony size) on mechanical properties, (schematically) [20].

A bimodal microstructure contains both equiaxed α and transformed β grains. It has a balanced microstructure of α grains and fine lamella α colonies within relatively small β -grains (10-20 μm in diameter). As with all Ti-6Al-4V microstructures, cooling rate plays an important role in the formation of this kind of microstructure during recrystallization. The cooling rate, determines the size of the primary α , α -lamella and transformed β grains [7, 15]. Figure 2-9 shows an example of a bimodal microstructure.

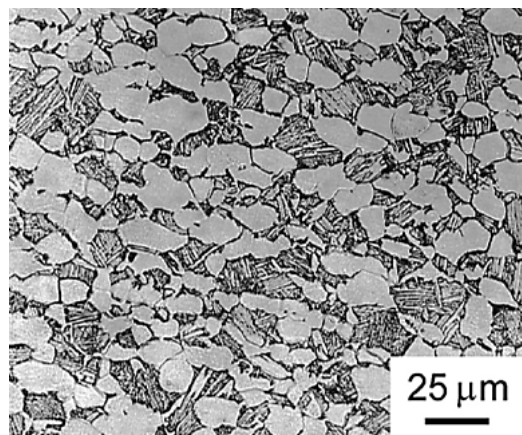


Figure 2-9: Bimodal microstructure in Ti-6Al-4V [21].

Lutjering [20] detailed a processing route to obtain a bimodal structure in four stages. The stages are homogenization in the β phase field (1st), deformation in the $\alpha + \beta$ phase field (2nd), recrystallization in $\alpha + \beta$ phase field (3rd) and aging at lower temperatures (4th). The homogenization stage (1st stage) occurs above the β -transus temperature with the remainder of the stages occurring below the β transus temperature.

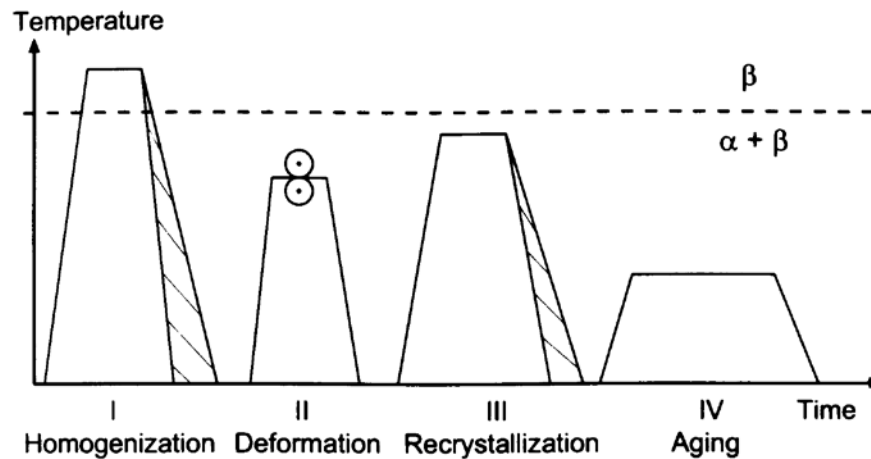


Figure 2-10: Processing route for bimodal microstructures, (schematically) [21].

2.3. Friction Welding

2.3.1. Introduction

Friction welding has been used extensively as a repair and joining technique [1, 2, 22-24]. It has successfully been implemented in the damage assessment and refurbishment of steam turbine blade/rotor attachment holes, and as a joining technique in the nuclear industry [25-26]. Examples of friction welding are Friction Stir Welding (FSW), Linear Friction Welding (LFW), Inertia Friction Welding, Friction Hydro Pillar Processing (FHPP) and Rotary Friction Welding (RFW) [1, 2, 27, 28]. Friction welding has numerous advantages which include:

- Low production time,
- High joint efficiency,
- Fast, repeatable, economic process that does not require an operator with welding skills.

- Flash formed when welding carries out most surface impurities and oxides out from the weld zone.

The main disadvantages of friction welding are that both the process and equipment is expensive, and the welding set-up takes time as compared to the actual welding time.

FSW was invented by The Welding Institute (TWI) and patented in 1991 [29]. In FSW of butt joint configuration, the material is clamped to a backing plate which acts as an insulator to maintain heat generated by the tool shoulder and tool pin as well as a forging anvil to contain the plasticised material. During the process, a rotating non-consumable tool is plunged between fixed or clamped plates. As the tool rotates and moves along the joint line, frictional heat is generated leading to plasticisation of the material in contact. A consolidated solid-phase joint is formed [29]. Figure 2-11 shows a schematic of FSW.

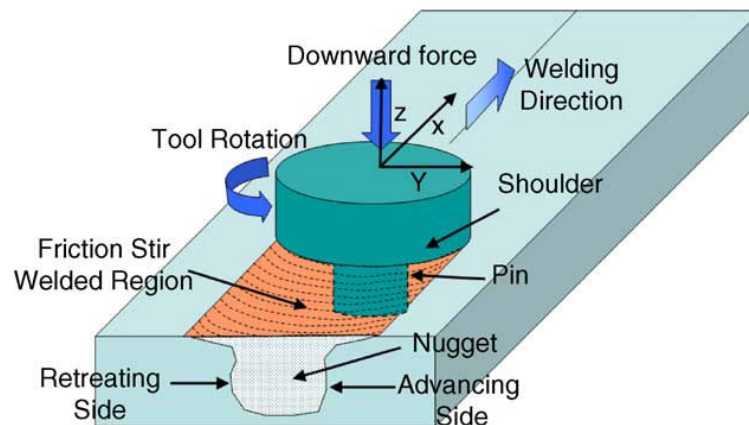


Figure 2-11: Friction Stir Welding schematic [29].

Mashinini [30] successfully employed Friction Stir Welding on 3 mm Ti-6Al-4V alloy. From his research, he found that in the weld zone, there was virtually no β phase for all welds done at high heat input because of the fine microstructure introduced by the FSW process. Figure 2-12 shows the phase map HAZ to weld zone of the FSW joint.

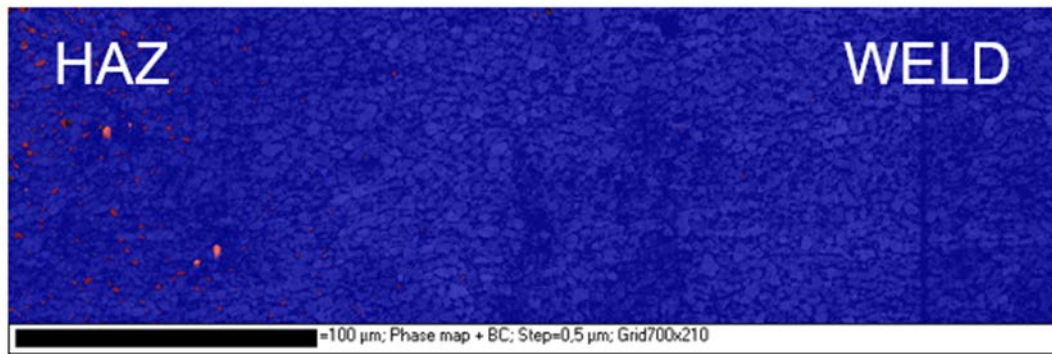


Figure 2-12: EBSD phase maps (α -blue: β -red) of 500 rpm and 120 mm/min (500 J/mm); HAZ and Weld Nugget [30].

Linear Friction Welding (LFW) involves frictional heat generation on the surfaces of a stationary component and one in reciprocating motion. As the two components rub against each other, an axial force is applied leading to some plasticised material being expelled from the interface as flash. Slowly that axial force is removed as the reciprocating motion is gradually stopped, bringing the two components into alignment. The temperature at the interface drops causing the material to fuse as it solidifies [31, 32].

Inertia friction welding is whereby one of the work pieces is connected to a flywheel while the other is fixed. As the drive motor is disengaged, the faying surfaces rub under pressure and are joined together by frictional forces. The kinetic energy in the flywheel is converted to frictional heat and is dissipated at the weld interface. As rotation stops, a forging force is applied for a set time [1].

The TWI inventors, Thomas and Nicholas described FHPP [33] as, “a technique that involves rotating a consumable stud rod co-axially in a hole whilst under an applied axial force”. When rotation starts at the interface between the stud and hole, the temperature at the interface increases. This allows the stud material to plasticise and shear off. Some of the material is pushed to the sides as a result of a decrease in resistance to the axial force. The consumption of the stud continues rapidly, forming shear layers. The first

shear layer forms at the base of the successive shear layer as the first cools and recrystallises. The process is repeated until the last shear layer is formed. The thickness of each shear layer is dependent on the temperature profile, the cross-sectional area and the mechanical properties of the stud. Figure 2-13 shows a schematic of FHPP.

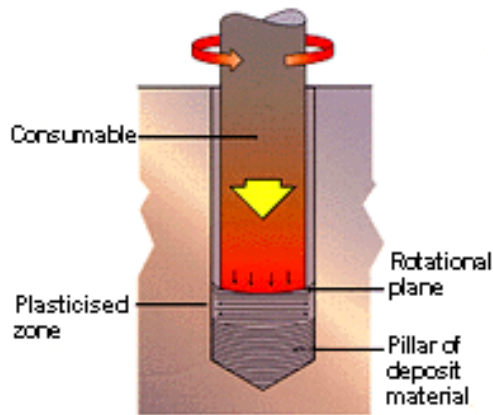


Figure 2-13: Friction Hydro Pillar Processing schematic [33].

2.3.2. Rotary Friction Welding

In this research work, the Rotary Friction Welding technique was used to join the small Ti-6Al-4V ELI components. RFW, one of the many variants of friction welding, occurs when a rotating shaft is joined to a stationary shaft under an axial force for a prescribed upset distance. As the upset distance is reached, the rotation is abruptly stopped, and a forging force is applied to consolidate the material as it cools (refer to Figure 2-14). As a result of the RFW process not exceeding the melting temperature of the material being welded, the process has metallurgical and mechanical benefits as compared to conventional welding methods [1, 23, 34].

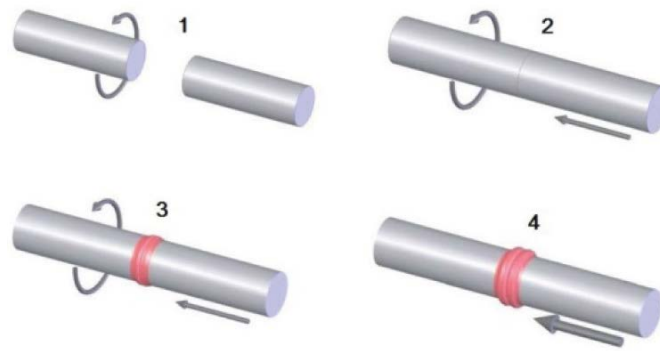


Figure 2-14: RFW process schematic [24].

A typical RFW procedure has four stages defined through analysing the friction torque curve. Kimura et al. [34] explained the four stages using the recorded process torque curve of a similar material joint. The four stages comprise of the following: stage one (1st) – the contacting of the faying surfaces followed by friction torque reaching an initial peak from zero; stage two (2nd) - the friction torque reaches equilibrium; stage three (3rd) – steady state stage and finally stage four (4th) - the forging (upset) stage. In the above-mentioned fourth stage, friction torque increases when a motor brake is applied and then drops to zero when the rotation is stopped (refer to Figure 2-15) [24, 34].

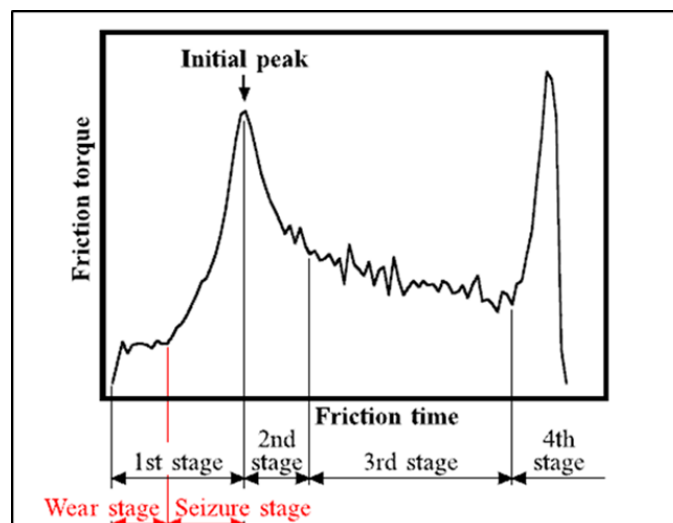


Figure 2-15: Definition of stages on the friction torque curve of RFW [34].

2.3.2.1. Microstructural Analysis of RFW joints

Avinash et al. [35] and van der Merwe [5] successfully joined titanium alloys using RFW. According to their respective research, a Ti-6Al-4V RFW joint has three microstructural zones which have different metallurgical and mechanical characteristics because of the differing temperature gradients and cooling rates. Figure 2-16 below shows the different microstructure zones obtained by van der Merwe [5].

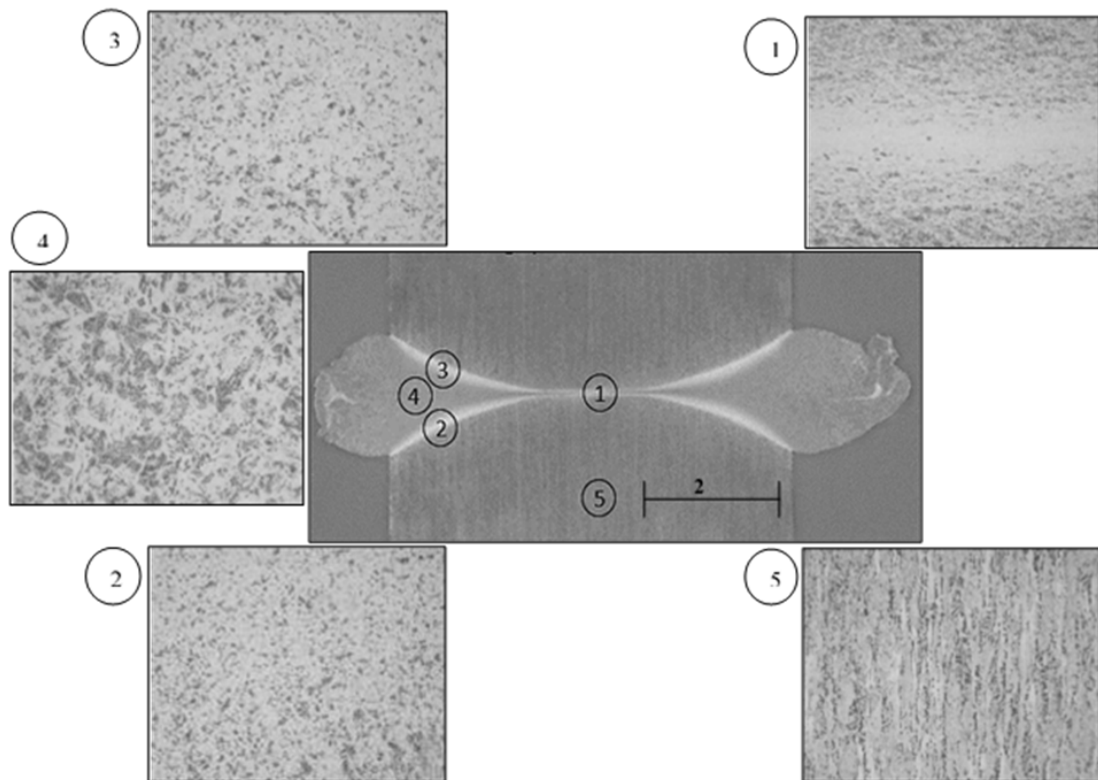


Figure 2-16: Micro image of a RFW Ti-6Al-4V joint [5].

Van der Merwe [5] details the microstructures exhibited in each zone as follows (refer to Figure 2-16):

- a) The weld interface (zone 1) contains predominantly elongated α grains (light) and intergranular β grains (dark) [36] formed by the opposing frictional forces.
- b) The HAZ (zone 2,3) microstructure consists of primary equiaxed α (light) and acicular $\alpha + \beta$ grains relating to a process temperature of 900 °C [39].

- c) The weld zone (4) consists of primary equiaxed α (light) and acicular $\alpha + \beta$ grains and relates to a process temperature of 955 °C after which it is air-cooled, forming the microstructure depicted in (4) [37].
- d) The parent microstructure shows a clear elongated primary α (light) and β (dark) grains which correspond to the annealed state of the received Ti-6Al-4V ELI alloy which was annealed at 760 °C for 1 hour [7].

2.4. Fracture Mode

2.4.1. Introduction

Metals fail in different modes and for different reasons. There are only four principal fracture modes, these being: dimple rupture, cleavage failure, de-cohesive rupture and fatigue failure. Dimple rupture is evident when overload is the principal cause of fracture. This type of failure exhibits cuplike depressions caused by micro void coalescence. This process occurs when micro voids nucleate at regions of localised strain discontinuities i.e., second phase particles, inclusions, grain boundaries and dislocation pile-ups. A common feature of dimple rupture is the characteristic elongated cuplike structure [7, 36].

Cleavage failure is a low energy fracture in comparison to a dimple rupture. It propagates along well-defined low index crystallographic planes called cleavage planes. As a result of a possible mismatch of the low index planes across the grain and sub-grain boundaries, a distinct cleavage fracture surface is produced. The surface produced exhibits cleavage steps, river patterns, feather markings, chevron patterns and tongues [7, 36].

A fracture that does not exhibit dimple-like failure and little or no bulk plastic deformation is known as a de-cohesive rupture. It is mainly ruptured along the grain boundaries that contain the worst melting point constituents of alloys [7, 36]. The fourth and most prevalent fracture mode, fatigue failure, is discussed comprehensively in section 2.4.2.

2.4.2. Fatigue Failure

Fatigue failure accounts for approximately 71% of material failures. Failure due to fatigue often occurs suddenly with catastrophic consequences. According to the ASM international [37], fatigue is defined as:

“The progressive localized change in a material subjected to repeated or fluctuating strains at stresses of maximum value less than the tensile strength of the material”.

Fatigue failure involves three stages: crack initiation, crack growth and final fracture. When a specimen is cyclic loaded, a fatigue crack nucleates or initiates on a microscopically small scale, followed by crack growth to a macroscopic size, and finally specimen failure. Fatigue crack initiation and crack growth are due to cyclic slip bands (i.e., plastic deformation as a result of moving dislocations). Normally, fatigue occurs at a stress amplitude below the yield stress. At these stresses, plastic deformation is limited to a small number of grains at the specimen's surface [37, 38]. Fatigue failure was first observed in Europe in the 1800s when bridges and railway roads exhibited cracks after repeated cyclic loading. A. Wohler proposed a method for analysing fatigue using a SN curve to better understand the fatigue behavior of different materials [37].

The important features of the SN curve as designed by A. Wohler are the following:

- Gradient (k), which governs the decrease of fatigue strength with an increase in cycles to failure and conversely a decrease of fatigue life. The slope is always negative.
- The endurance limit or fatigue limit (S_e), which refers to the maximum stress level below which failure does not occur irrespective of the number of load cycles applied.

Figure 2-17 shows the constituents of a SN curve designed by A. Wohler. Different types of loading exhibit different types of fracture surfaces (refer to Figure 2-18).

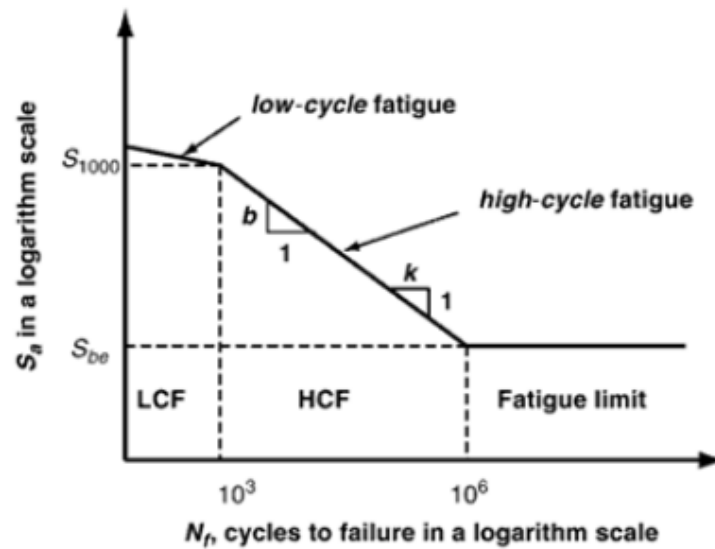


Figure 2-17: SN curve [39].

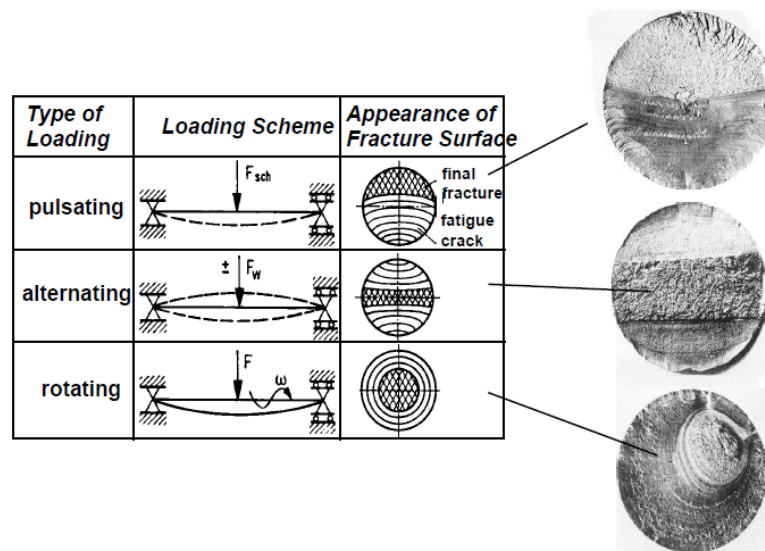


Figure 2-18: Fatigue loadings and the type of fracture surfaces [39].

2.4.3. Fatigue failure in Ti-6Al-4V

As discussed in section 2.2, titanium has superior mechanical properties (high specific strength and high fatigue strength) as compared to steel. Fatigue failure is also a major cause of implant loosening, stress-shielding and ultimate

implant failure together with wear in biomedical applications [40]. Designing to delay both crack initiation and crack propagation is difficult because microstructures in Ti-6Al-4V contradict one another. Titanium alloys with fine grains resist crack initiation better than basket weave structures and coarse grains. The fine grains normally exhibit slow crack propagation rates because of the higher density of grain boundaries. The grain boundaries inhibit crack growth because of the constant changing of the crack path direction thereby restricting the maximum slip length. Very fine acicular or lamella alpha grains also show improved resistance to crack initiation. Fatigue cracks generally nucleate as a result of irreversible slip within the longest crystallographic slip bands available in the microstructure [21, 40-46].

Van der Merwe [5] performed fatigue tests on RFW joints of Ti-6Al-4V extra low interstitials (ELI). From the fatigue tests, it was observed that crack initiation was predominantly in the HAZ region and crack initiation sites were located on the surface (refer to Figure 2-19). The microstructures near the outer surface of the weld were all refined equiaxed structures but their hardness values differed with a variation of 330 HV to 400 HV between WZ and HAZ respectively. This hardness differential is not desirable in fatigue testing; if the gradient is too steep, the joints will inherently have a poor fatigue life as result of the adverse grain boundaries providing loci for the crack initiation and propagation in the HAZ region. The observed microstructure in the Ti-6Al-4V ELI joints was an $\alpha + \beta$ structure as the welding process occurred below the beta transus temperature of 995 °C [5].

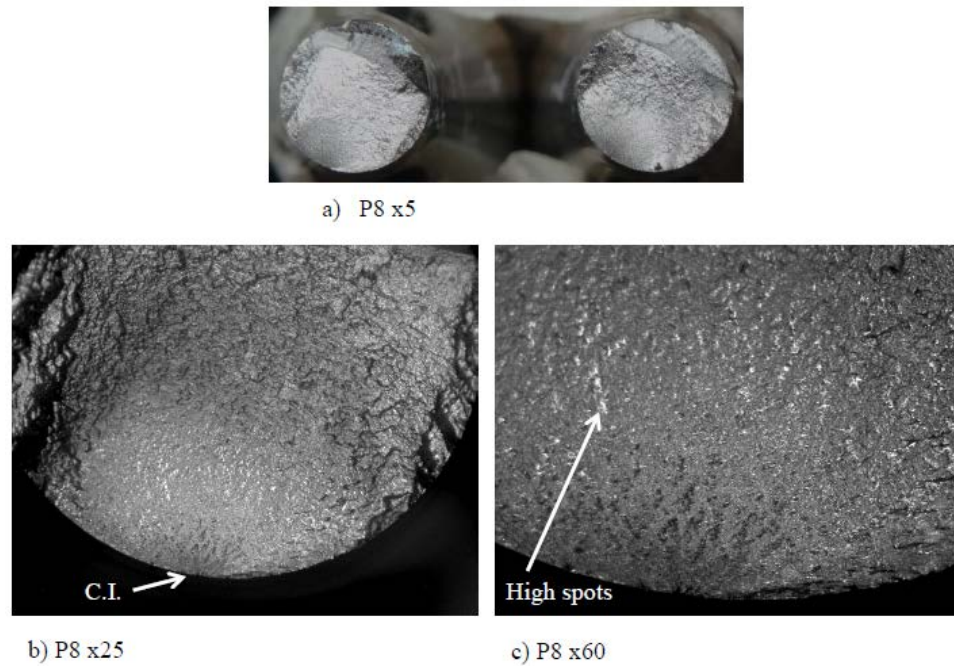


Figure 2-19: Fracture surface of a constant amplitude specimen a) full fracture surface b) crack initiation site c) high spots [5].

Mashinini [30] also discovered that surface geometrical stress raisers reduced fatigue performance in FSW and laser beam welding of Ti-6Al-4V. The as welded specimen had a reduced fatigue life compared to polished specimens as polishing of the specimens reduced or eliminated major surface defects. Crack initiation sites in the polished condition were a result of internal voids or polishing marks instead of surface defects which affected the slope of the curve by making it shallower.

Wu et al. [47] found that at high stresses, the strength of Ti-6Al-4V can be controlled by the size of the α grain or colony and the α lamella width in equiaxed and lamella microstructures. They observed that there is a decrease in the properties from bimodal, lamella and equiaxed microstructures in Ti-6Al-4V. The fatigue strength was noted to be dependent on microstructural parameters – namely, α_p content and α_p grain size in the bimodal microstructure, lamella α width size in the lamella structures and α grain size in the equiaxed microstructure [21, 47].

Figure 2-20 shows a SN curve at $R = -1$ for Ti-6Al-4V. In this figure, there is a clear variation in the slope of the curve for the four specified conditions. This gives an indication that surface treatment has the possibility to change the fatigue characteristic behaviour of materials. The untreated material has a run-out from 45 000 cycles at an endurance limit of 400 MPa [48].

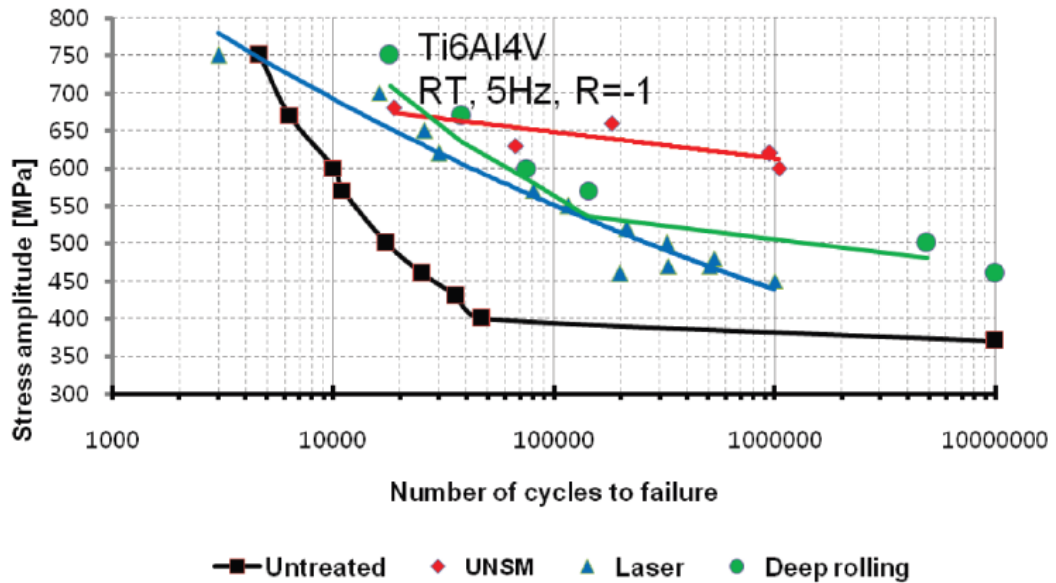


Figure 2-20: SN curve for different conditions of Ti-6Al-4V [48].

2.5. Residual Stresses

2.5.1. Nature and Origin

Residual stresses occur mainly as a result of manufacturing and fabrication processes. They arise due to shape misfits (called *eigenstrains*) between the unstressed shapes of different parts, regions, or phases of a component [49, 50]. Residual stresses may be classified into three categories as follows:

- By cause i.e. thermal or elastic misfits;
- By the scale;
- And, according to the way in which they are measured.

2.5.2. Measuring Technique and determination of residual stresses

There are three different techniques for measuring residual stresses: non-destructive, semi-destructive and destructive [49-51]. Of interest in this research are non-destructive techniques which do not alter the physical state of the component, for example, X-ray diffraction and neutron and synchrotron diffraction. Table 2-1 illustrates the differences in residual measurement techniques.

Table 2-1: Comparison of residual stress measurement techniques [50].

Residual stress measurement technique	Destructive	Contact	Speed	Reliability	Cost
Layer removal	Yes	Yes	Medium	Poor/medium	Low
Hole drilling	Yes	Yes	Fast	Poor/medium	Low
Synchrotron	No	No	Fast	High	Medium
Neutron diffraction	No	No	Slow	High/medium	High
X-ray diffraction	No	No	Fast	Poor/medium	Medium
Ultrasonic	No	No	Fast	Poor	Low
Raman	No	No	Fast	Poor	Medium
Magnetic	No	No	Fast	Poor	Medium

Diffraction only occurs in a material with a crystalline structure and once all the conditions of Bragg's law have been satisfied. A crystalline structure has periodic planes of atoms which can cause constructive and/or destructive interference patterns by diffraction. As stated in the NPL guide [52], the nature of the interference depends on the inter-planar spacing d , and the wavelength of the incident radiation λ . Figure 2-21 shows the principle of Bragg's law which is used in the measuring of residual stresses.

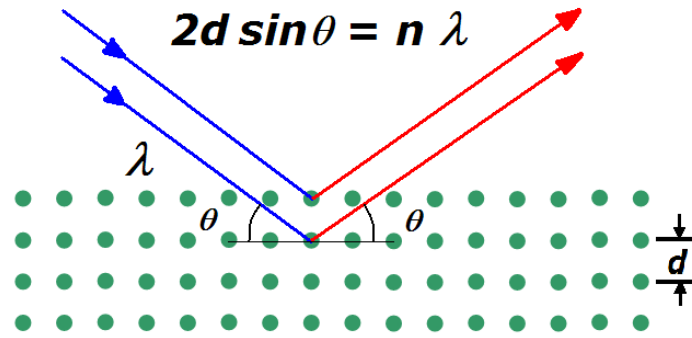


Figure 2-21: Principle of Bragg's law [52]

One method of calculating residual stresses from Hooke's law is using the $\sin^2\psi$ method as it is the most prevalent method used to calculate stress especially at different psi tilts angles [52-55]. Therefore, for any given lattice spacing the stress is calculated using the Equation 1 below:

$$\sigma_{\phi} = \frac{E}{(1 + \nu)\sin^2\psi} \left(\frac{d_{\psi} - d_0}{d_0} \right) \quad (1)$$

Where;

- s_{ϕ} Single stress acting in a chosen direction i.e. ϕ (MPa)
- E Elastic modulus (GPa)
- ν Poisson's ratio
- ψ Angle between the normal plane of specimen and normal of the diffracted plane ($^{\circ}$)
- d_0 Inter-planar spacing at free strain (\AA)
- d_{ψ} Inter-planar spacing of planes at angle ψ to the surface (\AA).

The technique utilised in this research to analyse residual stresses, energy dispersive synchrotron X-ray diffraction (EDXRD) After EDXRD measurements on the specimens were taken, the radial and axial strains were converted using a method proposed Olson and Bert (56) is discussed in section 6.2.

2.5.3. Effect of residual stresses on fatigue life

One of the main contributors to fatigue failure are residual stresses in a material. The effect of residual stresses on fatigue life can be both positive (life enhancing) or negative (life reducing). Table 2-2 illustrates the dependency of the effect of residual stresses on the mechanism of failure and on their magnitude, sign, and extent [55].

Table 2-2: Effect of residual stresses [55].

Magnitude	Sign	Extent	Primary Effect	Induced Effect
Moderate to high	Positive (+ve) or negative (-ve)	Component dimensions	Distortion during machining	Higher scrap rate fretting and fatigue crack initiation
	+ve or -ve	Localised microstructure	Increase in dislocation density	Higher corrosion rates e.g. in HAZ of welds in marine environment
	+ve or -ve	Component dimensions	Change in eccentricity of stress application along column	Change in buckling mode and load for welded columns
	-ve	Critical zone for crack initiation	Increase in resistance to fatigue cracking or fracture	Enhanced service life
	+ve	Component dimensions	Adds to tensile applied stress	Increased possibility of fast fracture in service
	+ve	Local defects. E.g. inclusions. Weld defect	Decrease in resistance to fatigue cracking	Decreased service life
	+ve	Critical zone for crack initiation	Possibility of environment assisted cracking	Decreased service life

Tensile residual stresses are mostly detrimental and are associated with the life reduction of material components. In welded components, the surface residual stresses are normally tensile. A compressive residual stress field, at the metal surface where cracks initiate and propagate, reduces the magnitude of applied tensile stresses. Mechanical surface treatment introduces a plastically deformed layer up to a certain depth from the metal surface. In a plastic environment, cracks do not initiate due to crystallographic defects (dislocations), therefore, the crack initiation point is driven further below the surface where bending stresses are not at a maximum [15, 50-55].

Bhadeshia [57] details the importance of metallurgical phase transformations and associated shape changes in affecting the development of residual stresses. He observed that fatigue life could be affected by deformation caused by bainite and martensitic transformations. These transformations lead to the elimination of residual stresses.

Mechanical surface treatments have been used to achieve improved fatigue performance of components. A compressive residual stress field is introduced using methods such as shot peening. Novel mechanical surface treatments i.e., laser shock peening and ultrasonic shot peening induce plastic deformation and compressive residual stress in a surface layer. This compressive residual stress is balanced by tensile residual stresses generated below compressive layers [56].

Peel et al. [58] studied the effect of residual stresses as a function of welding speed on FSW aluminium joints. They found that the weld zone was in tension both in parallel and perpendicular directions in relation to tool travel. By increasing the transverse speed, peak stresses formed closer to the weld line. The magnitude was approximately 40 MPa at 100 mm/min and increased to approximately 60 MPa at 200 mm/min. Steuwer et al. [59] used synchrotron X-ray diffraction to analyse residual stresses in Ti-6Al-4V FSW plates. They found that the transverse residual stress almost vanished in FSW Ti-6Al-4V

joints as shown in Figure 2-22. In the longitudinal residual stress profile, the state of the stresses were typical of FSW.

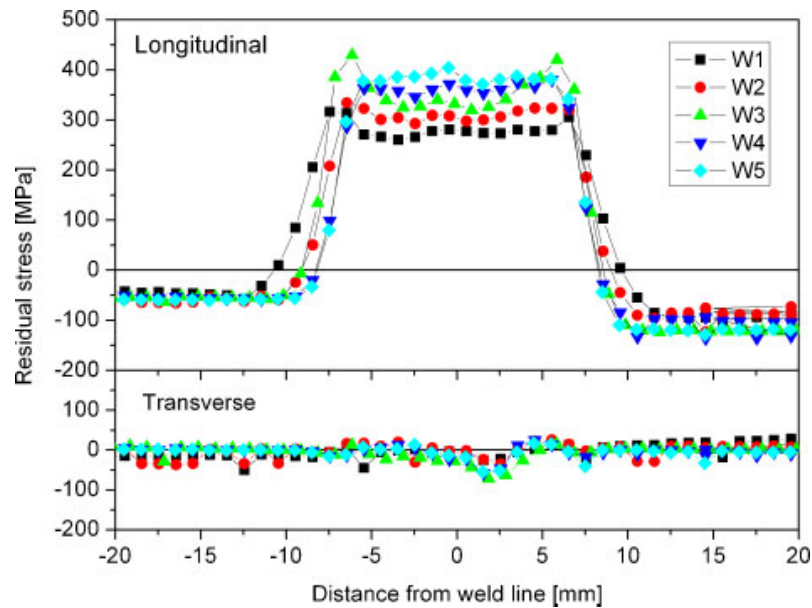


Figure 2-22: Longitudinal (top) and transverse (bottom) residual stress profiles of Ti-6Al-4V FSW joints [59].

Post weld heat treatment is normally performed on welded components to reduce the effect of tensile residual stresses by placing welded specimens into an oven. This method is only practical for small components and is not necessarily adaptable to in-service components. Moat et al. [60] observed that after post weld heat treatment of IFW dissimilar high strength steels, there was a minimal reduction (less than 100 MPa) in the high tensile stresses of the S/cmv side of the inertia friction welded specimen. On the Aermet side, PWHT entirely relieved the tensile in the HAZ of the joint.

PWHT in Ti-6Al-4V has shown that if the tensile residual stresses are very high, the amount of time spent on stress relief may not necessarily produce the desired effect on the material surface residual stresses state. Figure 2-23 shows the effect of stress relief on time for Ti-6Al-4V [60]. This study will expound further on the relationship between residual stresses, microstructures and fatigue in Ti-6Al-4V ELI.

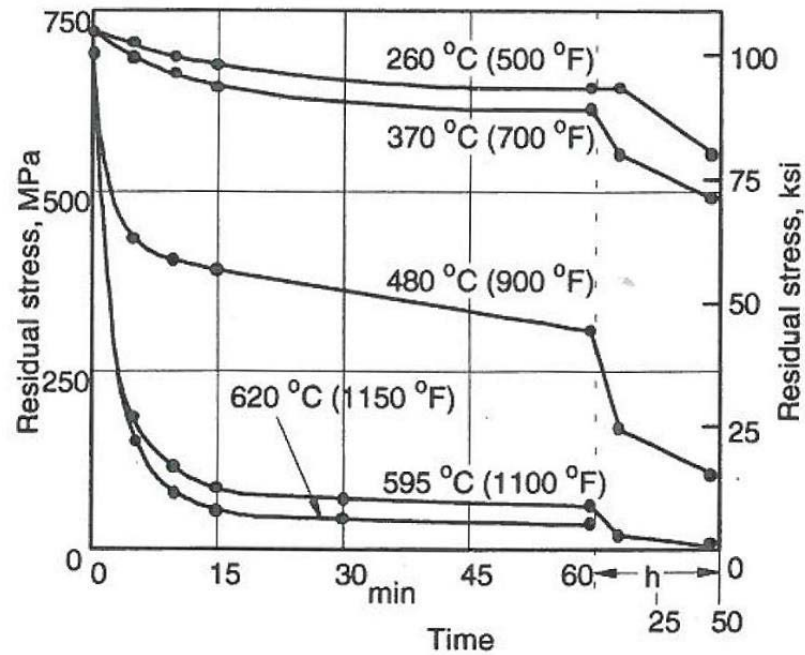


Figure 2-23: Stress relief versus time of Ti-6Al-4V [59].

2.6. Laser Material Processing

2.6.1. Introduction

Laser material processing has been used extensively in the manufacturing industry as a joining and post-processing technology. The acronym LASER is derived from: Light Amplification by Stimulated Emission of Radiation. A laser beam consists of monochromatic coherent radiation. It emanates from a source (called a Resonator) that produces (emits) radiation (light or even in the invisible spectrum) of in-step waves of identical frequency, phase, and polarization. Laser systems produce a collimated and coherent beam of light. Coherent light is different to the light emitted from the sun or from household light bulbs, which is incoherent due to the light being radiated in all directions [15, 61, 62]. Figure 2-24 shows the difference between incoherent and coherent light.

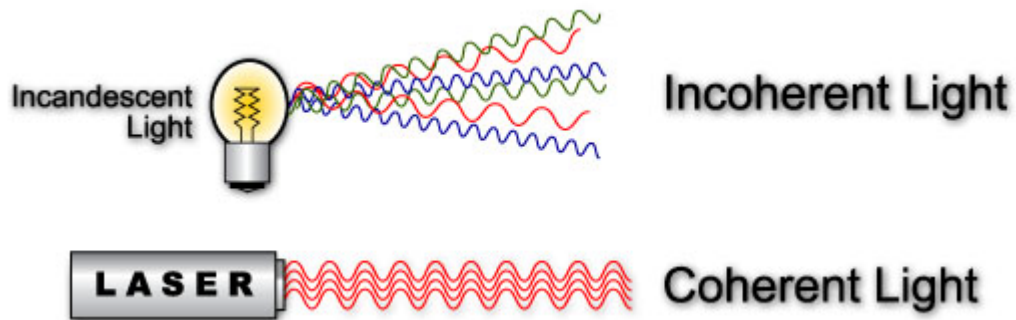


Figure 2-24: Coherent and incoherent light [75].

Laser light is generally a narrow wavelength light; yet, there are lasers that emit a broad spectrum of light or emit different wavelengths of light simultaneously [61, 63]. Lasers are a source of concentrated thermal energy. To transfer this thermal energy, compatibility is required between the laser beam and the material. The relationship between the material and laser beam is dependent on the laser beam wavelength [61]. The basis of the process is formed by the interaction of the laser beam and the work piece.

The main advantages of laser systems are as follows:

- Low heat input on the work piece due to focussed or concentrated energy density at the work piece;
- Flexibility when automated;
- Easy incorporation into conventional manufacturing processes;
- High processing speeds with good repeatability;
- Lack of tool wear as it is a non-contact manufacturing process.

Laser processing is used in industrial applications, such as cutting, welding and surface treatments (annealing, melting and hardening). A number of laser systems are commercially available, examples of which are ND: YAG system and CO₂. Laser systems that produce beams with a top-hat intensity distribution have a constant and well-defined beam size throughout the scanned area as compared to those of the Gaussian intensity distribution. A top hat profile enables optimum power to be distributed uniformly throughout the whole scanned area leading to the homogeneity of the microstructure [61].

Laser processing can be grouped into three different classes by making use of power densities (irradiance) and exposure/interaction time [61]. The three categories are as follows (refer to Figure 2-25):

- I. Heating (transformation hardening, bending and magnetic domain control – processes require low-power density).
- II. Melting (surface melting, glazing, cladding, welding and cutting – processes require high-power density).
- III. Vaporization (cutting, drilling, ablation – processes require substantially high-power density within a very short interaction/pulse time).

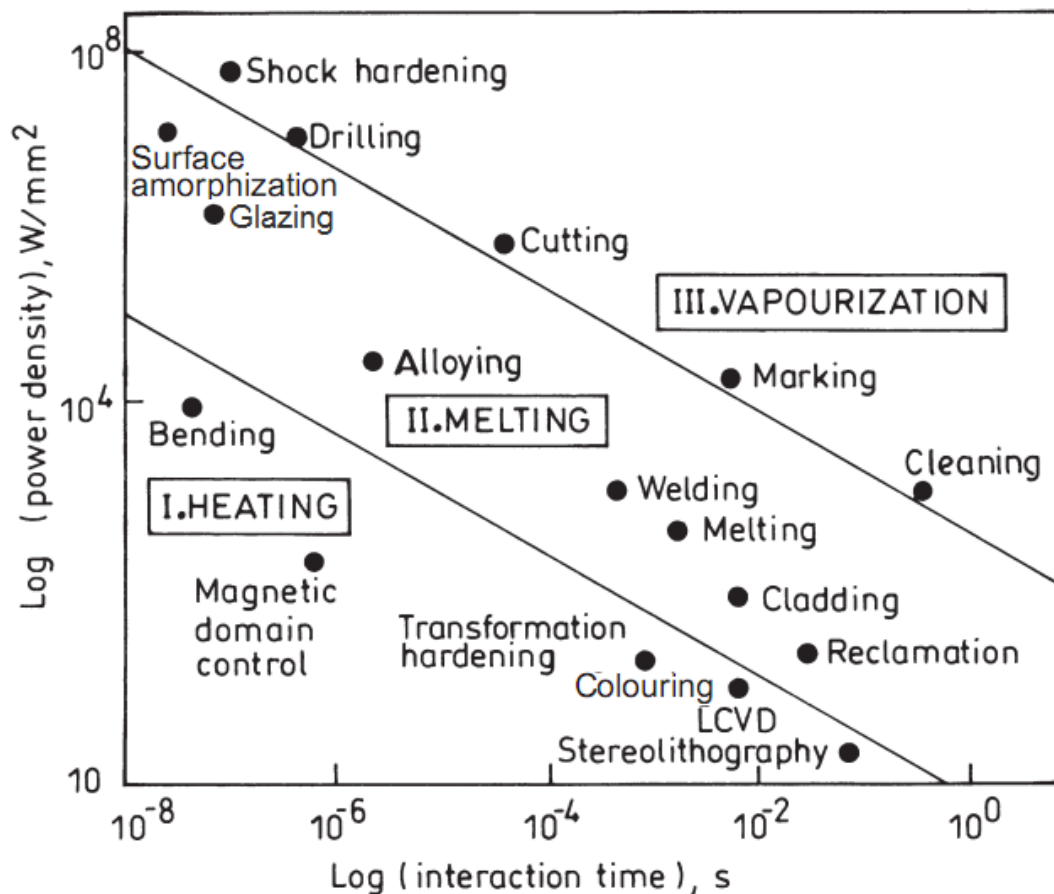


Figure 2-25: Different laser processing techniques [63, 64].

2.6.2. Laser surface treatment

Laser surface treatment or engineering is one of the variants of laser materials processing or engineering. It is termed surface treatment, as the laser

radiation does not penetrate through the material. LST is classified into two categories these being thermal and thermochemical processes [3, 62]. The thermal LST is a process in which a defocused beam scans across the specimen or component, rapidly heating the material above the phase change temperature. When heating is above or below the melting temperature, the process is either termed laser surface melting or laser surface hardening respectively. The unaffected bulk material acts as a heat sink causing rapid cooling. The main benefit of this process is that material hardness, strength, fatigue, and wear can be improved. In the steel manufacturing industry, laser surface hardening is applied extensively to improve surface dependent properties [66-68].

An example of a thermal process is laser surface melting (LSM) in which the material surface is laser melted and rapidly re-solidified without any direct addition of alloying elements that would modify the chemical composition of the surface. The main advantages of LSM, an example of thermal LST, are the following:

- It is a homogenous surface treatment process.
- LSM is easily repeatable which is crucial for the biomedical industry.
- It is a cheaper process as compared to other laser modification techniques as less material and energy are required.
- LSM more easily creates a crack-free modification as compared to laser nitriding and cladding processes.

Thermochemical LST processes change the material's microstructure and composition. Thermochemical processes involve the addition of alloying elements for example laser surface alloying (LSA) and laser cladding to name a few. Figure 2-26 shows the different laser processing methods [65].

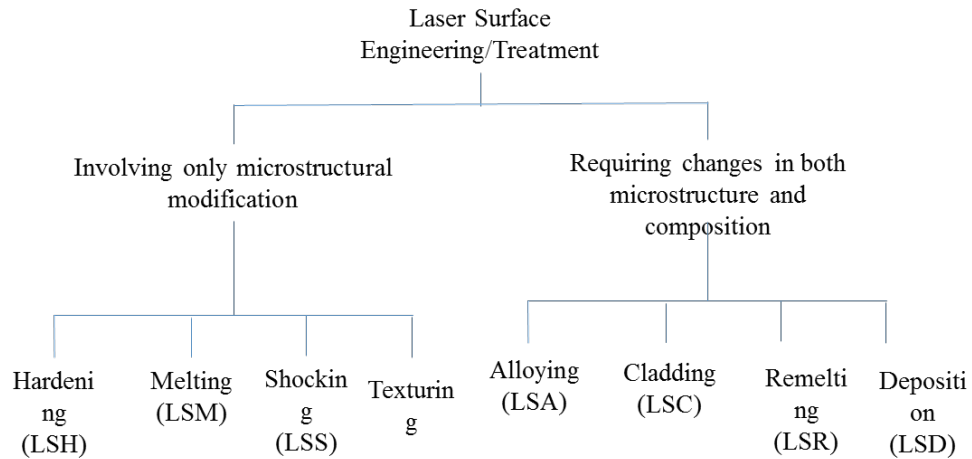


Figure 2-26: Laser surface treatment/engineering process [64].

Chikarakara [69, 70] conducted high-speed laser melting on Ti-6Al-4V in an inert environment to improve corrosion and wear properties. It was observed that a well-bonded 20 to 50 μm region could be attained, with no cracks, voids or surface asperities by the process of LSM. Typical $\alpha + \beta$ microstructure in the as-received Ti-6Al-4V was transformed to acicular α embedded in the β matrix due to the high cooling rates experienced. Figure 2-27 reveals a typical crack-free cross sectional microstructure of the laser melted region in Ti-6Al-4V and highlights the phase transformation in the modified layer.

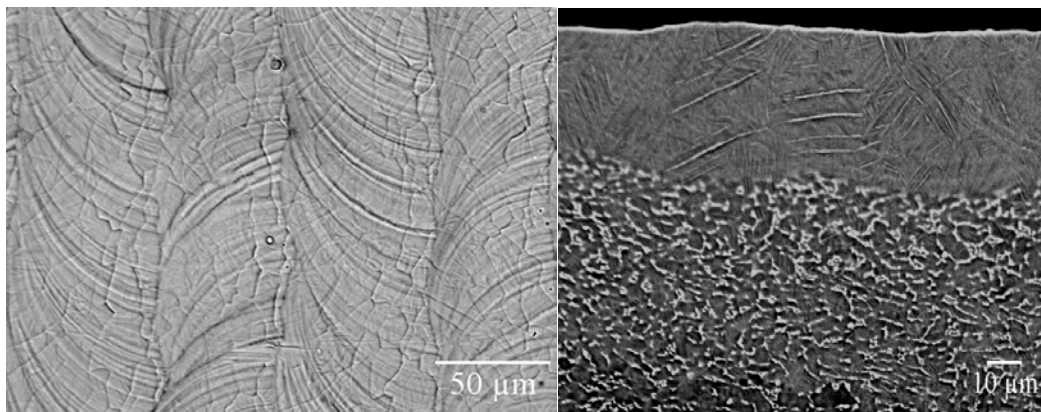


Figure 2-27: Top view and cross sectional micrograph of laser modified Ti-6Al-4V [69].

Singh et al. [71] observed that the transformed β (or acicular α) is more prominent at high laser powers. The size of each colony increased from 65

μm to $89 \mu\text{m}$ with an increase in laser power from 800 W to 1500 W. The increase in grain / colony size was correlated to an increase in the temperature as power increased [70]. Figure 2-28 shows the microstructure of Ti-6Al-4V processed at different laser powers.

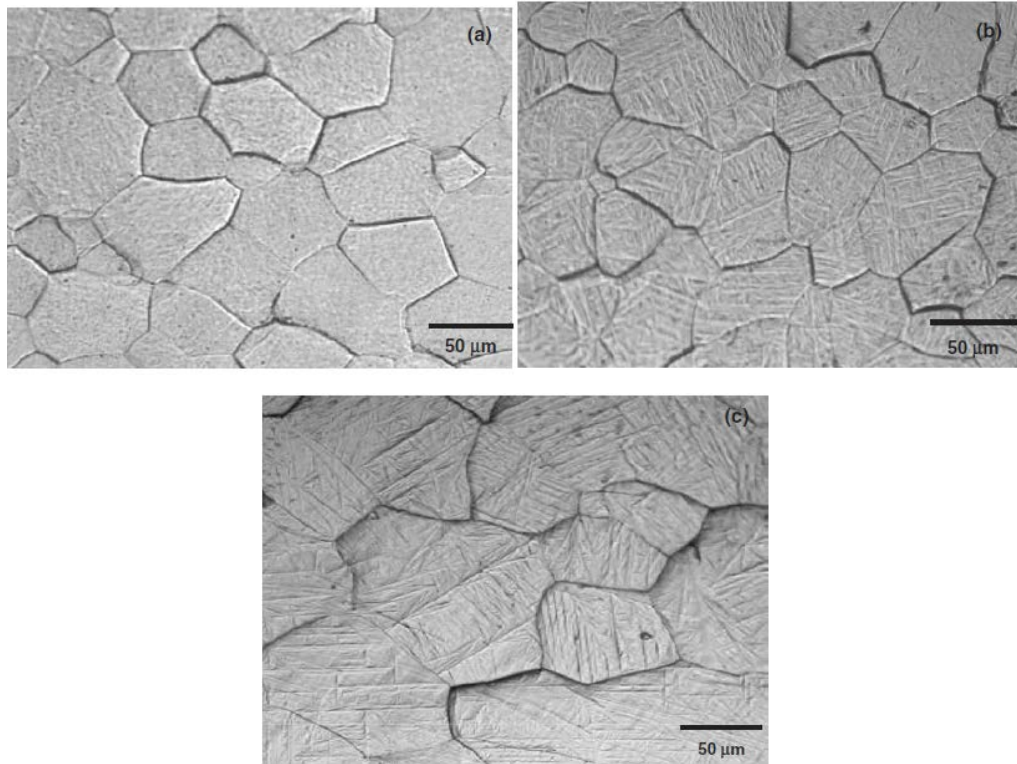


Figure 2-28: Microstructure of Ti-6Al-4V after laser surface treatment at a) 800, b) 1200, and c) 1500 W powers [71].

Badkar et al. [72] conducted laser surface transformation hardening (LSTH) on unalloyed titanium (Grade 3). LSTH introduces a hardened layer on the surface material. Their main observation was that heat input plays an important role in the hardened bead parameter dimension. Figure 2-29 shows the observed microstructure from LSTH with measured parameters i.e. bead width and hardened depth.

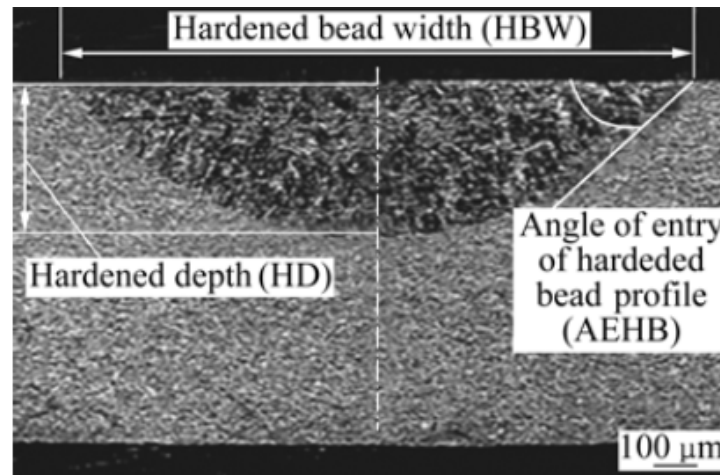


Figure 2-29: Microstructure appearance [71].

Akgun et al. [73] performed hardening of Ti-6Al-4V alloy with LSM and laser surface alloying (LSA) in a nitrogenous atmosphere to improve the wear characteristics of Ti-6Al-4V. For LSA, niobium, molybdenum and zirconium were used as alloying elements. Both LSM and LSA increased microhardness by almost threefold in comparison to the as-received material.

Steam turbine moving blade failures are mainly due to stress corrosion and cracking, wet erosion and fatigue. Fatigue failures occur because of resonant conditions where the blades deflect and stresses rise leading to failure. In an attempt to combat stress corrosion cracking and wet steam erosion, Majumdar et al. [62] studied the influence of laser power on the hardening of Ti-6Al-4V low steam turbine material. The results of the study show that the LST of Ti-6Al-4V alloy improved the water droplet erosion resistance. LST processing between temperatures of 1700 °C and 1800 °C led to the formation of a fine-grained martensitic (α') phase. The formation of this microstructure was due to the heating and rapid cooling associated with LST. X-ray diffraction analysis showed an increased α phase with a balance of mechanical properties, for example fatigue, while the ductility of the material was not affected [62].

Biswas [68] conducted laser surface remelting on Ti-6Al-4V in a nitrogen environment to improve surface-dependent properties namely, surface wear resistance. Laser surface remelting in a nitrogenous environment improved

hardness from 250 HV for the as-received material to a maximum of 450 HV. This hardness increase correlates to the microstructure observed in the remelted zone, which was martensite.

2.6.3. Laser surface treatment process parameters

The principles of LST are closely interlinked with that of laser welding. LST of materials requires precise control of the laser power in comparison to drilling and cutting. The main input process parameters to consider are focus position, scanning speed and laser power. These input primary process parameters influence energy input and power density of the process. The LST parameters are explained below [61].

Focus position (FPn) is the position of the laser beam with respect to the specimen. The units for the focus position are millimetres (mm). In welding, it is the position that gives the maximum penetration depth allowing for maximum joint penetration i.e.

- Focus position = 0: Focus is located on the specimen.
- Focus position < 0: Focus is located underneath the specimen.
- Focus position > 0: Focus is located above the specimen.

The focus position directly affects the spot size. Figure 2-30 shows the configuration of focus spots obtained with varying distances between the lens and the specimen.

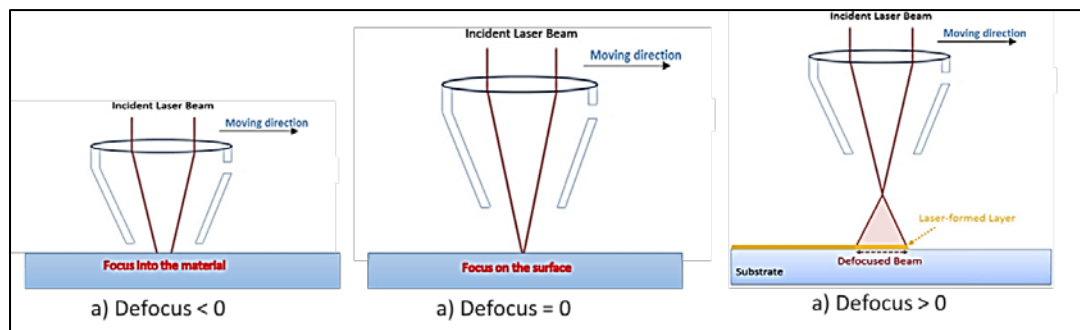


Figure 2-30: Focus position: a), beam into the material, b) beam on the work piece surface, c) beam defocussed.

Figure 2-30 illustrates a schematic of different focus position locations in relation to the material surface. During laser welding, the focus position is normally on the material surface or below the surface of the material being joined or welded. In welding, a focus position is a position that gives the maximum penetration depth. In the LST process, the beam is normally defocussed above the material being processed. Defocussing generally means that instead of the focus being on the material or below the material surface, it is a few millimetres above the material surface. Defocussing allows an increase in the area being irradiated by the laser beam [61].

Laser power (LP) is defined as the amount of power irradiated on the surface. It primarily refers to an optical power output, measured in Watts, of the laser beam in a continuous wave, pulsed, or modulated laser.

Scanning Speed (SS) is the speed, in millimeters per second (mm/s), at which the laser beam is irradiated on the surface. Both laser power and scanning speed are considered primary LST parameters. When these two are combined, a secondary parameter, energy input is established (refer to Equation 2).

$$\text{Energy Input} \left(\frac{J}{mm} \right) = \frac{\text{Laser Power (W)}}{\text{Scanning Speed} \left(\frac{mm}{s} \right)} \quad (2)$$

Energy input affects laser penetration depth and width. Increasing scanning speed whilst maintaining constant laser power leads to a decrease in penetration depth in LST. The bead width is critical when conducting multiple surface treatments as this determines the required overlap. An overlap of 50% is desirable for both LST and laser seam welding. Figure 2-31 depicts a 50% weld overlap in seam welding.

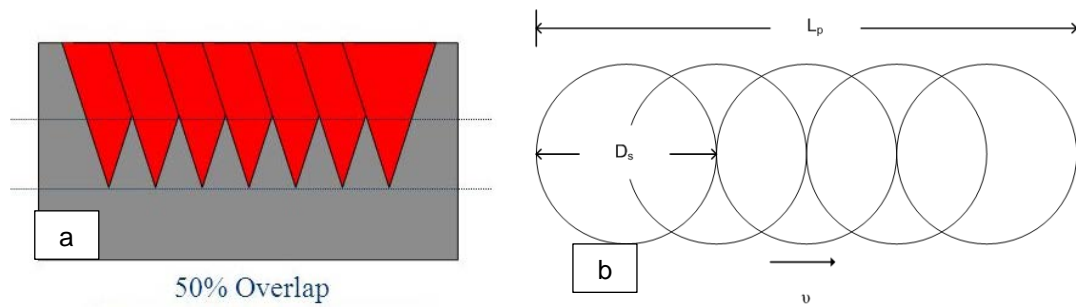


Figure 2-31: An example of 50% overlap in: a) seam welding, b) LST using a pulsed laser.

Power density (Pd), is also a secondary process parameter in laser processing. It is defined as the laser power over the area on the upper surface of the specimen (laser beam spot size). The spot size is related to the focus position (refer to Figure 2-30). Equation 3 gives the power density formula.

$$\text{Power density} \left(\frac{W}{mm} \right) = \frac{\text{Laser Power (W)}}{\text{Beam spot size (mm}^2\text{)}} \quad (3)$$

2.7. Summary

This chapter discussed the characteristics of Ti-6Al-4V and its behaviour under friction welding. The types and different microstructures of Ti-6Al-4V were discussed in detail. The literature investigation also analysed the fatigue behaviour of different Ti-6Al-4V microstructures. It was noted that predicting fatigue failure of different Ti-6Al-4V microstructures is difficult as the microstructural properties contradict one another between crack initiation and propagation. A successful joint using Ti-6Al-4V ELI rods can be achieved by friction welding. Fatigue failure was mainly as a result of crack initiation in the HAZ of the RFW joint. Crack initiation in the HAZ is as a result of hardness and microstructural variation, which is due to varying cooling rates across the RFW joint.

LST has been used extensively in manufacturing industries to improve surface-dependent properties of components. There are two main variants of LST, which are thermal and thermochemical processes respectively, as discussed in this literature review section. For the purposes of this research, a thermal process of LST was considered, which consists of two types of thermal processes, namely laser surface hardening and laser surface melting. These two processes mainly differ in respective process temperature with melting requiring higher power densities than hardening. Both thermal processes of LST have been used extensively for improving the wear and corrosion characteristics of steels.

LST is not a new process but the bulk of modification studies on Ti-6Al-4V have previously been conducted using laser nitriding. This research proposes a systematic way of improving surface-dependent properties by using thermal laser processing techniques. Therefore, to the researcher's knowledge, no research work has been published in which the mechanical properties of Ti-6Al-4V RFW joints have been enhanced using a LST technique.

Chapter 3. Research Material, Testing and Processing Platforms

3.1. Introduction

This chapter introduces the research material, testing and processing platforms utilised for the welding, laser surface treatment and testing of specimens. The main platforms utilised are discussed, these being the Weldcore III friction welding platform, Trumpf 5020 (TruDisk) laser system and the rotary bending fatigue machine. Details of the experimental work and weld verification conducted during the RFW process are also discussed.

3.2. Research Material

The material used in this investigation was a commercially available diameter 14 mm Ti-6Al-4V ELI bar. Ti-6Al-4V ELI (Grade 23) is similar to Ti-6Al-4V (Grade 5) as shown in Table 3-1, with the exception that Ti6Al4V ELI contains reduced levels of interstitials (Ti-6Al-4V ELI, oxygen content should not exceed 0.15 %). ELI is an acronym for Extra Low Interstitials. These lower interstitials provide improved ductility and better fracture toughness as compared to the Ti6Al4V material. From three tensile test results, the average yield and ultimate tensile strength of the research material was 901 MPa and 1029 MPa respectively. The Modulus of elasticity and Poisson's ratio used for Ti-6Al-4V ELI were 114 GPa and 0.3 respectively.

Table 3-1 details the chemical composition of Ti-6Al-4V ELI. The as supplied material, diameter 14 mm, was machined to the desired shape.

Table 3-1: Chemical composition specification % wrt.

	Ti-6Al-4V ELI	Ti-6Al-4V
Aluminum, Al	6%	6%
Vanadium, V	4%	4%
Carbon, C	0.03%	0.03%
Iron, Fe	0.1%	0.1%
Oxygen, O	0.1%	0.15%
Nitrogen, N	0.01%	0.01%
Hydrogen, H	<0.003%	0.003%
Titanium, Ti	Balance	Balance

3.3. Research Platforms

3.3.1. Weldcore III Friction processing platform

RFW was conducted using a Nelson Mandela University developed Weldcore III platform. The Weldcore is the third generation of developed Weldcore platforms at the university. The machine was intentionally designed for process research on FHPP. The platform was designed to allow the operator to independently control process parameters, for example, rotational speed, axial force, upset distance and forge force.

The Weldcore III platform makes use of the Human Machine Interface (HMI) to monitor and control process parameters before and during welding. Before the start of each weld, input process parameters are programmed into the HMI weld programme, which is then used to control and monitor the whole joining process.

The platform output feedback data is analysed to determine the quality of the process. The Friction Processing Weldcore III platform is shown in Figure 3-1. Table 3-2 lists the platform capabilities.

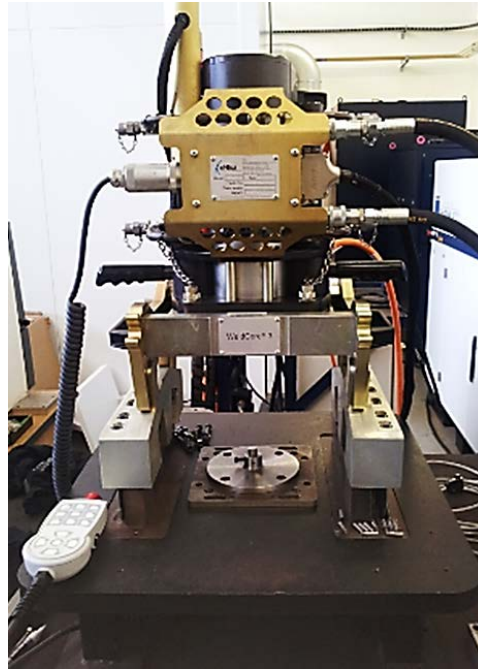


Figure 3-1: Weldcore III Friction Processing platform.

Table 3-2: Weldcore III platform capabilities.

Process Parameter	Weldcore III range
Rotational Speed	0-5250 rpm
Axial force	0-40 kN.

3.3.2. Trumpf TruLaser5020 laser cell

The laser cell or system utilised for the process of LST was the Trumpf Laser cell 5020. This platform is able to combine high precision engineering, which includes cladding, welding, cutting and surface treatment. To perform these different techniques, the platform is equipped with three interchangeable heads for cladding, welding and cutting. Figure 3-2 and Figure 3-3 show the laser robot with the welding head used for the process of LST. The laser system can adequately weld 3-dimensional configurations and has six travel axes. The laser robot is able to travel in the x, y and z-axis and tilt the head while the bed can rotate and tilt at an angle.

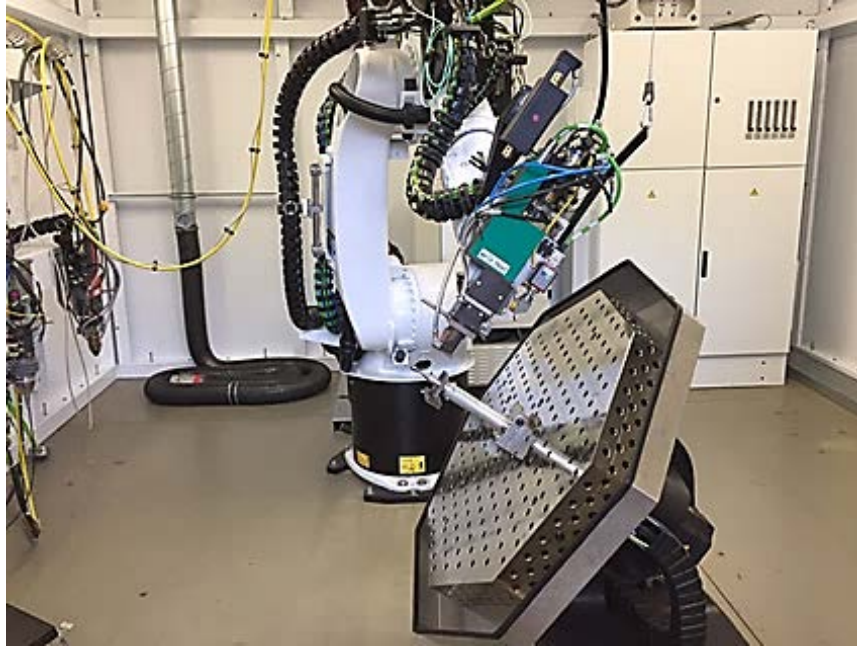


Figure 3-2: Laser Kuka robot.

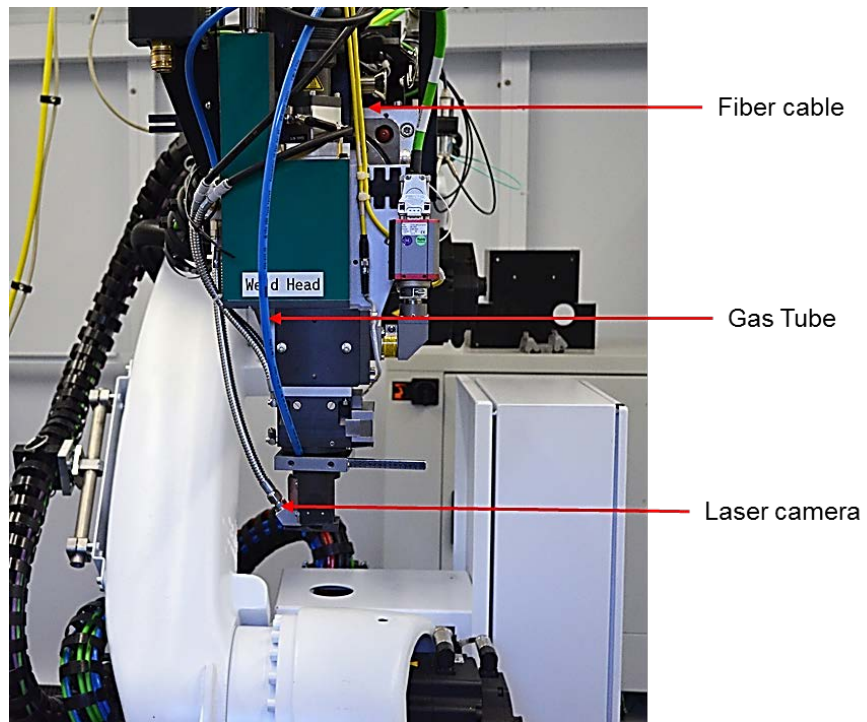


Figure 3-3: Laser welding head.

The laser source utilised was a Trudisk 4001. The laser source is located behind the laser cell and provides laser power for the three different laser processes. The source has a wavelength of 1030 μm and is able to provide continuous laser power from 80 W to 4000 W. The source can operate in both continuous and pulsed modes. Appendix A lists the characteristics of the laser source in detail.

The laser system has two gas outlets, which can be integrated into cutting, welding or cladding processes. A shielding strategy was implemented in the set-up of the LST experiment, with one making use of a Perspex shielding box and the other using the as-supplied laser nozzle. The experimental set-up configurations utilised during the LST process will be discussed extensively in the chapters to follow. Appendix A shows the focus graph of the laser source. This was used in calculating the spot diameter.

3.3.3. Temperature measurement

Temperature measurement was undertaken using a Data Translation DT9871 Temp-point amplifier. Measurements of temperature were collected during the LST process. The experimental procedure is detailed in section 4.3.2 Figure 3-4 shows the temperature measuring device utilised.

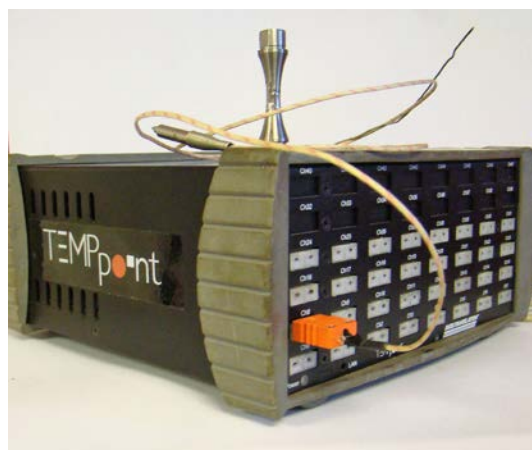


Figure 3-4: Temperature point amplifier.

3.3.4. Rotating bending fatigue machine

Fatigue testing was the main mechanical evaluation technique conducted. A rotating bending fatigue machine was used to ascertain the fatigue strength of the parent material, RFW and LST specimens. The type of rotating bending fatigue machine at the Nelson Mandela University is a Punz. A Punz type fatigue machine has a constant bending moment over the whole sample's length as opposed to the Punn type, which has the bending moment proportional to the distance of the strain. The design of the straining device makes it possible to hold the alternating bending stress constant for the samples during the experiment, but it cannot create an additional constant preload. Samples in a polished condition, are stressed over the test length with a constant bending moment. Figure 3-5 shows the Punz rotating bending fatigue machine at the Nelson Mandela University.

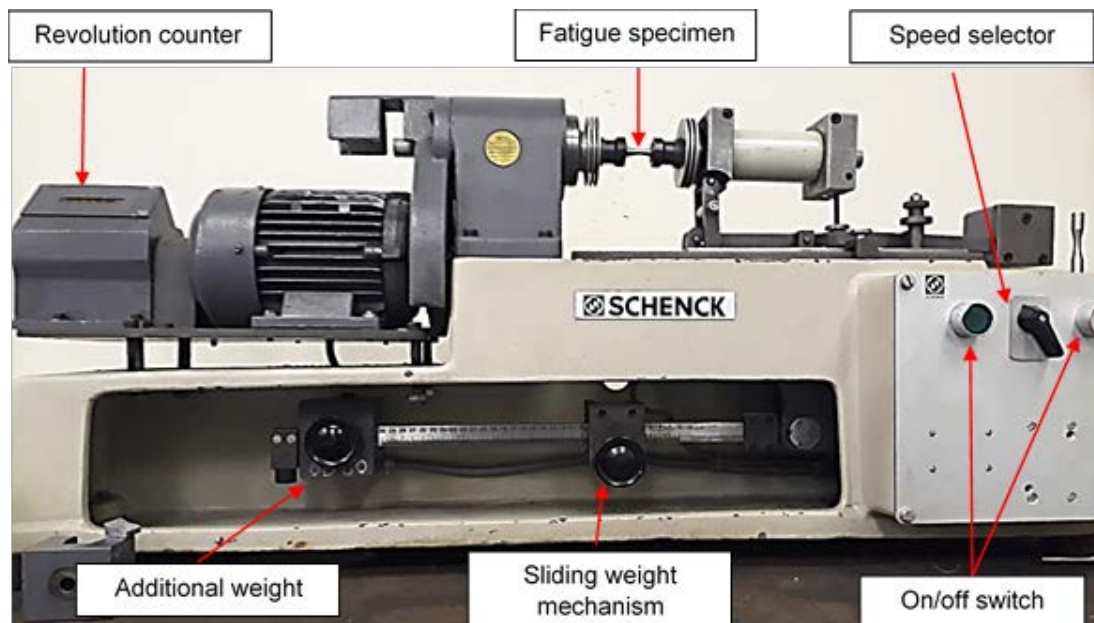


Figure 3-5 Rotating bending fatigue machine.

The two clamping spindles are driven by a toothed belt transmission. Two rotational speeds of 6000 rpm and 12000 rpm are easily selected using a speed selector. When the specimen breaks, a switch-off contact stops the machine. The revolution counter or the load cycle counter is directly connected to the drive motor with a rubber coupling. It has the same

transmission ratio as the toothed belt drive. On the PUNZ, the strain on the samples is created via a sliding weight system and a deflection device that generates a bending torque in the sample, which is constant between the fixed points.

The loading system or strain system was verified using strain gauges mounted on a fatigue specimen. Resistance strain gauges were attached to the fatigue specimen at the smallest diameter which corresponded to the area of maximum stress. A full bridge configuration was utilised and the specimen was attached to the fatigue machine. Figure 3-6 shows the loaded strain gauged specimen. The specimen was loaded and unloaded with corresponding strains recorded and tabulated as shown in Table 3-3.



Figure 3-6: Load verification on the Punz

Table 3-3: Strain measurements vs sliding weight movement.

Sliding loading (mm)	Strain measurements ($\mu\text{m}/\text{m}$)				Stress (MPa)	Error
	1	Average	3	Average	Average	
0	0	0	0	0	0	0
5	304	260	200	254.7	29	6
10	899	818	700	805.7	92	11
15	1162	1134	1174	1156.7	132	2
20	1637	1722	1581	1646.7	188	8
25	2017	2030	2092	2046.3	233	5
30	2418	2508	2540	2488.7	284	7
60	5075	4840	5016	4977.4	567	14

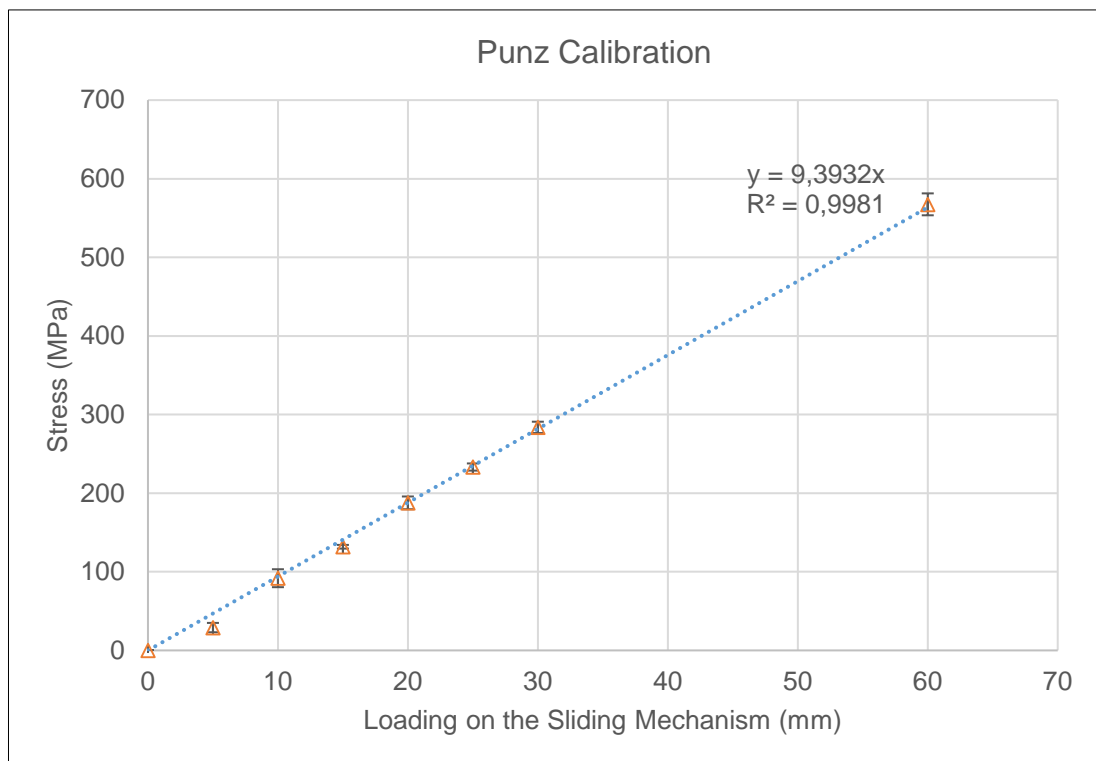


Figure 3-7: Calibration curve.

3.3.4.1. Experimental set-up and procedure

The fatigue tests were conducted using the rotary bending machine housed at the Nelson Mandela University. The platform (refer to Figure 3-5) utilised for fatigue testing was discussed in section 3.3.4, which detailed the method used to calibrate the platform. Before the commencement of each fatigue test, the procedure outlined below was followed:

- The ends of the fatigue specimen were reduced from an $\text{Ø}12$ mm to an $\text{Ø}10$ mm to fit the collet sizes of the specimen.
- The fatigue specimens were polished in the sequence shown in Table 3-4. After polishing, the fatigue specimen's surface roughness was measured using the surface roughness measurement machine. The driving factor in conducting surface roughness tests is that titanium is very sensitive to surface finish when being fatigue tested. Any surface defects or scratches tend to become sites for crack nucleation. The average surface roughness of the specimens was $R_a = 0.42$, which indicated a polished surface finish.

Table 3-4: The fatigue specimen preparation polishing sequence.

Polishing sequence	Sandpaper roughness	Time (min)
1	P180	1
2	P360	1
3	P600	1
4	1200 grit	2

- The fatigue specimen's dimensions were checked and verified to be within specification.
- The reduced section's diameter was checked and noted.
- The ends of the specimen were greased slightly before insertion in the collet.
- The specimen was clamped by tightening the nuts in the collets.
- The concentricity was checked by rotating the specimen slowly with the overall run-out not to exceed 0.06 mm. A high run-out would affect the load distribution on the sample.

- The specimen was loaded, the revolution counter read, and the revolutions noted to signal the start of testing.
- A speed of either 12000 rpm or 6000 rpm was selected using the speed selector. For high stresses, a speed of 6000 rpm is recommended (No temperature monitoring or controlling of specimens was done but using a low speed, 6000 rpm would lower the temperature of the specimen).
- The “Ein” (On) button was pressed to start the machine.
- When the specimen broke, the machine stopped automatically. The revolution counter was read again and the value noted.
- The machine was switched off by turning the selector to position ‘O’ off.
- The specimen was removed by loosening the nuts, and pushing the collets out using a bolt.
- The broken fatigue specimens were immediately marked and stored in a desiccator.
- The spindle and collets were cleaned and greased.
- The steps above were repeated for each specimen.

3.4. RFW Processing of Ti-6Al-4V ELI Samples

3.4.1. Introduction

This section details the process of RFW of Ti-6Al-4V ELI. The experimental set-up and the weld verification are explained.

3.4.2. Rotary Friction Welding of Ti-6Al-4V set-up

The set-up utilised in the RFW development is shown in Figure 3-8. The set-up consists of the two studs machined from the as received Ø14 mm Ti-6Al-4V ELI bar, load cell, and a shielding mechanism (discussed in the sections to follow).

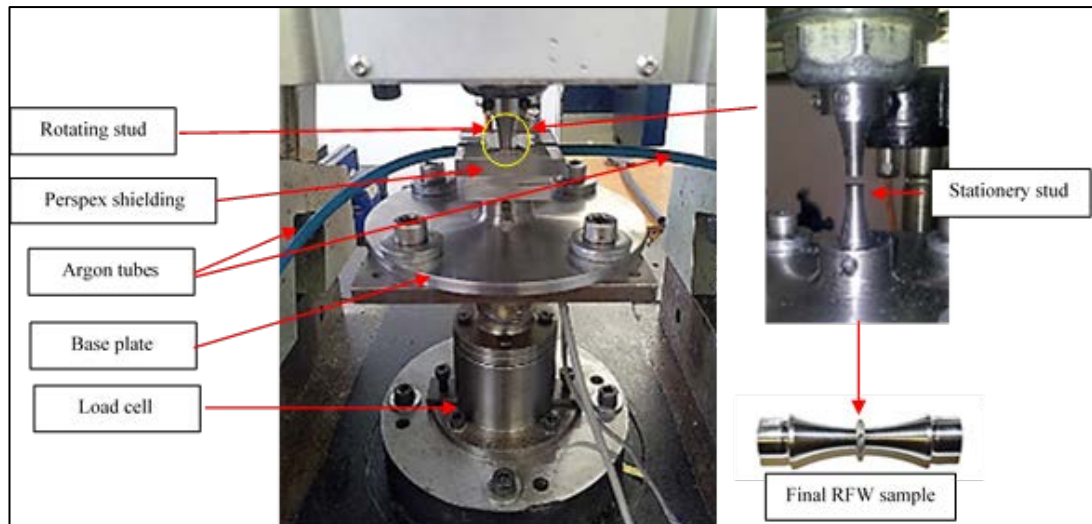


Figure 3-8: RFW set-up.

3.4.3. RFW consumable stud design

The RFW specimen was successfully used by van der Merwe [5] and was designed according to the ASTM E 466 – 96 Standard of force controlled fatigue tests. This type of design was beneficial as it was easily implementable and compatible with the Weldcore III and the rotary fatigue machine. The standard provides guidelines for the design of high cycle fatigue specimens. Figure 3-9 shows one half of the stud design and the parent fatigue specimen geometry.

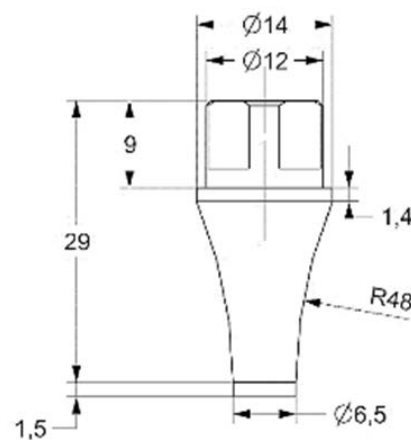


Figure 3-9: Stud design for RFW process.

3.4.4. RFW shielding mechanism

The welding of high temperature materials such as titanium alloys requires a shielding strategy to protect the weld from oxidation, as oxidation decreases the ductility of these high temperature materials. Additionally, titanium is a highly reactive material at temperatures above 650 °C, it is essential to shield it from oxidation. The amount of oxidation at these elevated temperatures should not exceed 200 ppm. When performing any of the RFW and LST processes, an adequate shielding strategy is required. Therefore, a purposely designed shielding mechanism was integrated into the system as illustrated in Figure 3-8. During welding, an inert gas (for the purpose of this study - argon) is used as a shielding gas. The resultant welds had a shiny metallic flash with no evidence of discolouration by oxidation.

Table 3-5 shows the process parameters utilised for the RFW process. The process parameters used for the RFW process were similar to the final parameters established by van der Merwe [5] and Tsikayi [18].

Table 3-5: Input RFW process parameters.

Process parameter	Magnitude
Axial force (N)	4000
Rotational speed (rpm)	2500
Upset distance (mm)	1
Forge force (N)	6000
Forge time (sec)	9

A typical RFW process of Ti-6Al-4V ELI as conducted in this research, involved pre-machined studs aligned to each other with a maximum clearance of 10 mm between them. The stud in the welding head collet travelled in the z-direction at a specified feed rate of 100 mm/min until it probed the surface of the bottom fixed stud at a specified probe force. The specified probe force was equal to the axial force of 4 kN. After the probing command was complete, the moving stud moved up 0.5 mm and then started rotating until the set rotational speed of 2500 rpm was achieved.

The welding process started as the stud moved and contacted the surface of the fixed stud and an axial force of 4 kN was applied. On initial contact with the fixed stud, the temperature of the stud material rises sharply with an associated torque peak due to rubbing of the facing surfaces (rotating stud and fixed stud). When the pre-set upset distance to form a RFW joint was achieved, the rotation was stopped abruptly and the final forge or forming sequence was completed allowing the plasticised material to consolidate during the cooling phase. The forging stage refined the grain size while the material consolidated forcing out excess plasticised material as flash. A typical RFW torque curve for the welding of Ti-6Al-4V ELI specimen is illustrated in Figure 3-10 and has four stages similar to the stages explained by Kimura [34] (refer to section 2.3).

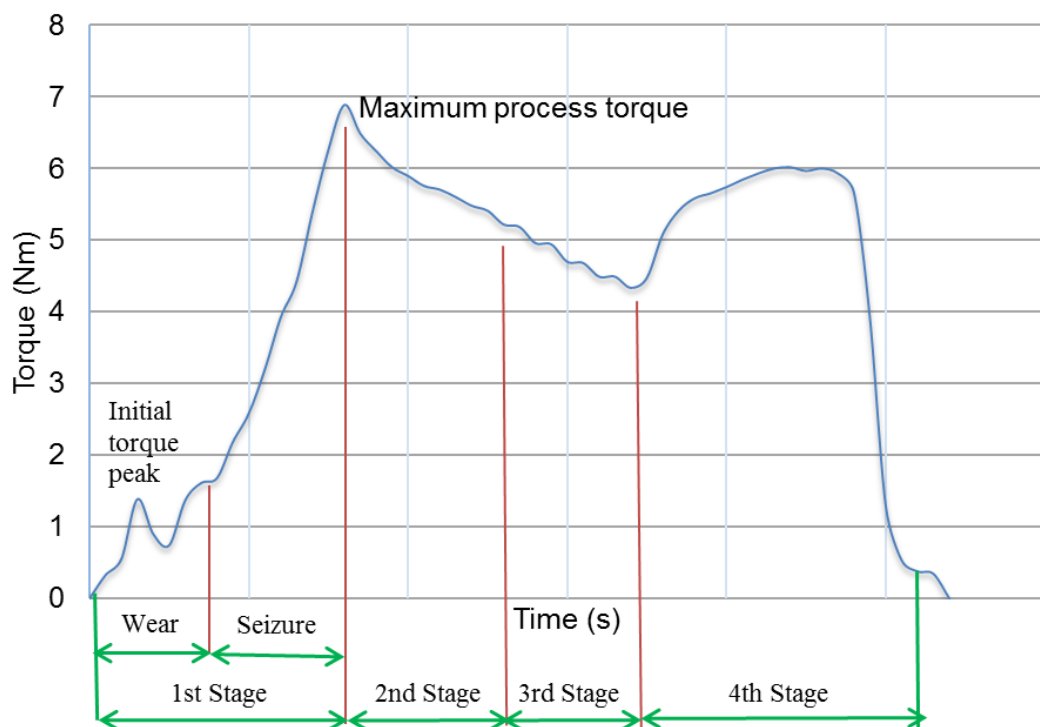


Figure 3-10: A torque curve of RFW Ti-6Al-4V ELI.

When RFW small coupons, it is important to verify the weld quality by looking at the feedback data. In this research, weld quality verification was conducted using the RFW upset process feedback data. Owing to the volume of friction

welds that were conducted, analysis mainly focused on upset distance. The upset distance (upset) was used as a tool to verify whether the weld was successful or not. The input upset distance was 1 mm and, from the feedback data, it was decided that a final upset of between 1 to 1.5 mm would be deemed a good weld. Figure 3-11 graphically represents the feedback (upset and speed) data obtained from the RFW of Ti-6Al-4V ELI. Refer to Appendix B for the friction weld upset verification and an analysis of the upset distances of the 40 friction welds conducted.

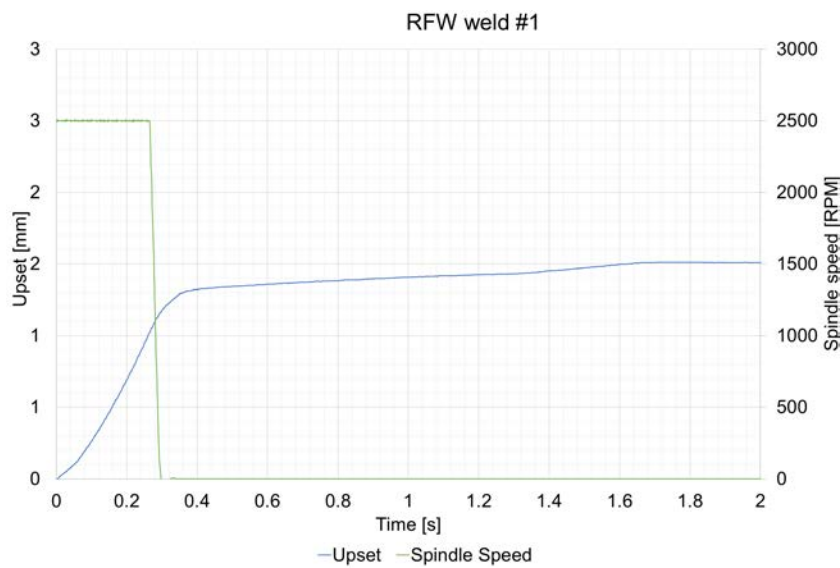


Figure 3-11: Example of the RFW weld upset process feedback data analysis.

3.5. Summary

This chapter described the platforms used in the RFW process and the LST process development. The main method of mechanical evaluation, which made use of the fatigue rotary bending platform, was discussed. Additionally, the physical and chemical characteristics of the research material were discussed. The RFW process was presented in conjunction with analysed process data to determine upset limits for a good weld.

Chapter 4. Laser Surface Treatment

4.1. Introduction

The process development of laser surface treatment of Ti-6Al-4V ELI friction welded specimens is detailed in this chapter. The process development was divided into three stages. The first stage involved conducting experiments on 3 mm Ti-6Al-4V sheets by performing single laser treatment experimental runs. The first stage gave an understanding on the envisaged process of laser surface treatment and its process parameters, such as focus position and the influence of laser power. The observed macrographs were quantified in terms of LST zone's depth of penetration and laser bead width. A relationship was established between the process parameters, LST zone's depth of penetration and width. A hardness and microstructure analysis was also conducted on selected specimens of the LST flat sheet trials to understand the microstructure modification introduced by this treatment process.

The second stage involved treatment of the surface of parent specimens of the fatigue hourglass specimen geometry. It was decided to conduct preliminary work on parent material as it would reduce costs related to RFW and the machining of the welded specimen to the correct fatigue specimen geometry. This preliminary work allowed for the type and influence of treatment strategy to be analysed, particularly on cylindrical fatigue hourglass specimens. The influence of treatment strategy on the LST zone's depth of penetration was established with emphasis on achieving homogeneity of LST zone's depth around the whole cylindrical specimen's diameter.

The third stage involved the final matrix development. In the developed matrix, treatment was performed on the RFW fatigue hourglass specimen detailed in the section 3.4.3. The developed matrix was used to establish statistically the effect of the main LST process parameters by making use of three variable

Central Composite Design matrix. The three variables or process parameters analysed were laser power, focus position and scanning speed. For the LST process, a non-continuous treatment strategy, as opposed to a continuous treatment strategy, was the method used for LST on the RFW specimens. Figure 4-1 shows details an overview of the process development methodology that was applied during the LST process development.

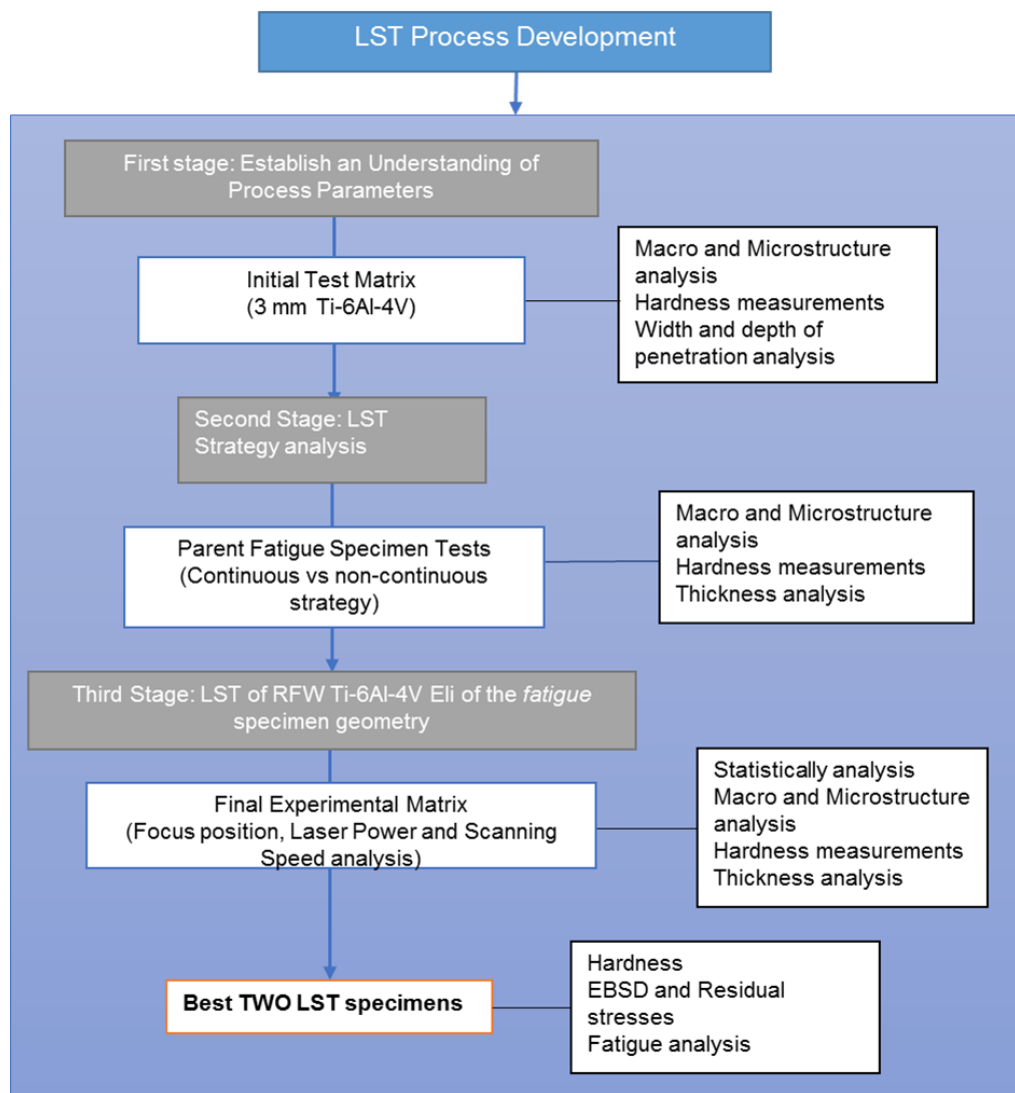


Figure 4-1: LST development methodology.

4.2. Stage 1: Process Development on 3 mm Ti-6Al-4V Sheets

4.2.1. Introduction

As stated in the chapter introduction, this section or first stage was undertaken to understand the characteristics of the process of LST which included depth of penetration and bead width and to define the process limitations of the laser system or platform utilised for this research. The experimental procedure, methodology and results of the first stage are explained.

4.2.2. Experimental set-up

Although the main study was performed on round bar Ti-6Al-4V ELI material, this initial development process made use of Ti-6Al-4V 3 mm sheets. The 3 mm flat sheets used were readily available Ti-6Al-4V offcuts, previously used in FSW at the Nelson Mandela University. These offcuts allowed for a cost-effective method for initial characterisation and understanding of the process limits of the LST and the laser system being utilised for this work.

Figure 4-2 shows a schematic of the experimental set-up used for the LST of the 3 mm Ti-6Al-4V sheets. In order to shield the surface from oxidation, the experimental set-up incorporated the shielding gas nozzle located on the laser system robot (refer to Figure 3-2). Argon gas was blown onto the surface of the specimen during the process of LST.

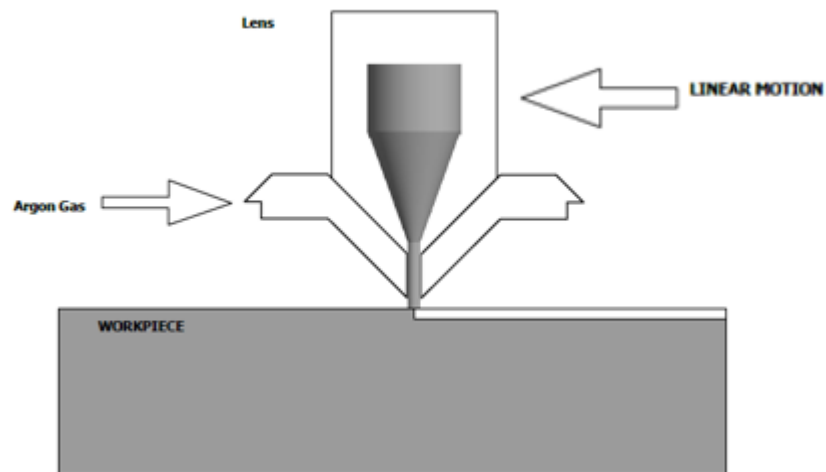


Figure 4-2: Schematic of LST of 3 mm Ti-6Al-4V sheets.

Table 4-1 shows the experimental trial runs that were performed, highlighting the initial process parameters utilised. The process parameters that varied were laser power and focus position with scanning speed being kept constant at 41.7 mm/s.

Note: In this work, a defocus of 5 mm is denoted as positive (+) 5 mm. This indicates that the laser beam is not focussed on the material but 5 mm above the material surface (refer to section 2.6.3).

Table 4-1: First stage analysis: 3 mm Ti-6Al-4V.

LST	Laser Power (W)	Focus position (mm)
1	1000	0
2	1000	+5
3	1000	+10
4	2000	+0
5	2000	+5
6	2000	+10

4.2.3. Results

Figure 4-3 and Figure 4-4 shows the resultant macrograph and the measurements of the LST zone's depth of penetration and bead width of the flat LST specimen trials.

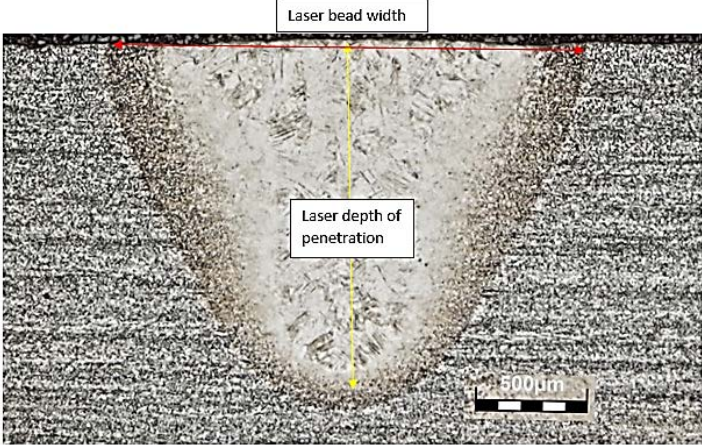


LST Specimen No	Macro	Bead width(mm)	Depth of penetration (mm)	Comment
1 (1000 W; 0 mm)		2.01	1.58	The bottom of the LST macro exhibited a narrow, almost pointed shape. The shape is because of the laser beam being focused on the material surface.
2 (1000 W; 5 mm)		1.88	0.571	Oval-shaped at the bottom. Reduced depth of penetration when compared to LST due to the +5 mm focus position
3 (1000 W; 10 mm)		1.98	0.42	Oval-shaped and with the least depth of penetration

Figure 4-3: Results of first stage analysis.



LST Specimen No	Macro	Bead width(mm)	Depth (mm)	Comment
4 (2000 W; 0 mm)		2.85	3	Processed the whole 3 mm sheet. The profile of the macro is similar to that exhibited in laser beam weld.
5 (2000 W; 5 mm)		2.89	2.059	Not oval-shaped at the bottom. Profile similar to that of LST at a laser power of 1000 W and focus position of 0 mm.
6 (2000 W; 10 mm)		3.01	0.8	Oval-shaped at the bottom.

Figure 4-4: Results of first stage analysis (continued).

Figure 4-5 graphically represents the results of focus position against the laser depth of penetration. For both the 1000 W and 2000 W trials, it was observed that with an increase in positive focus position (defocus), there was a reduction in the depth of penetration. At a focus position of +10 mm, the reduction in the depth of penetration was minimal as compared to focus positions of 5 mm and 0 mm. Theoretically, by increasing the focus position (defocussing the laser beam), the depth of penetration decreases because the laser beam is moved upwards from the material surface. The reference position (0 mm) is at the material surface (refer to section 2.6.3).

At a constant focus position but different laser power, there was also a difference in the attained LST depth. For example at focus position of 0 mm and laser powers of 1000 W and 2000 W, the LST depth increased by 1.48 mm, showing that the amount energy input irradiated by the laser beam into the surface increased.

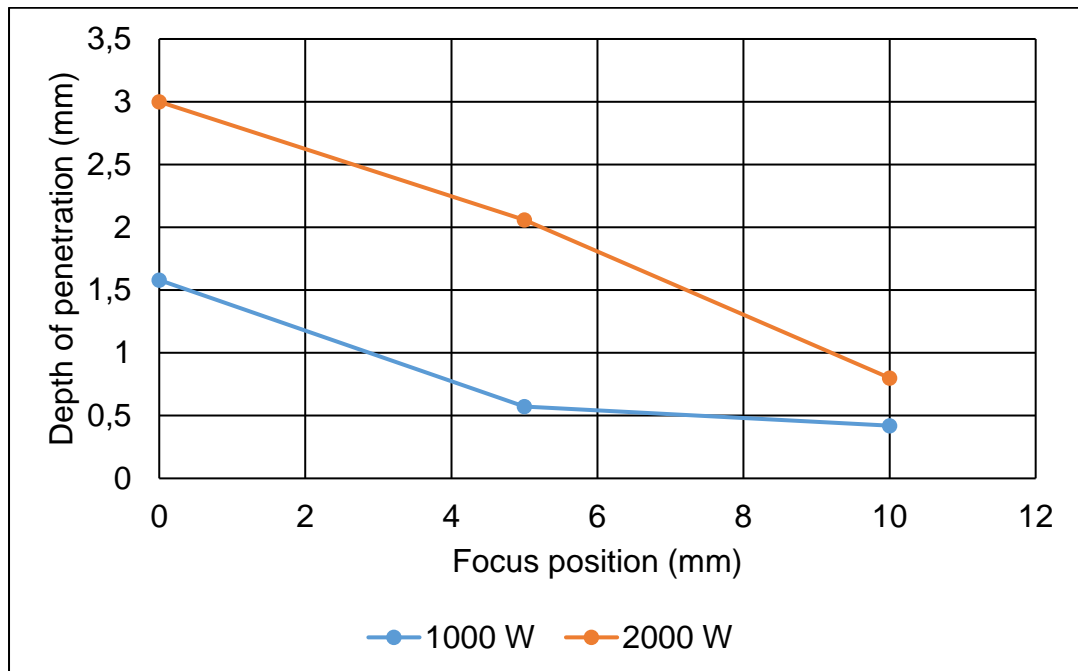


Figure 4-5: Analysis of focus position vs depth of penetration.

Figure 4-6 shows the graph of focus position against bead width. From the results, it was observed that at the same laser power, the LST zone's bead width was not significantly affected by changing the focus position unlike the focus position's effect in the depth of penetration.

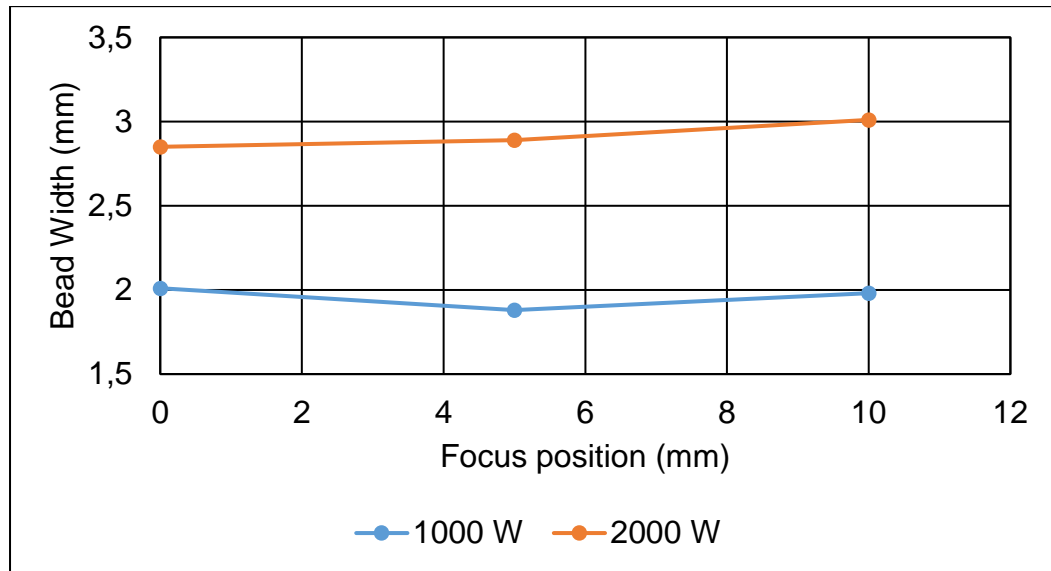


Figure 4-6: Analysis of focus position vs width.

These observations could hypothetically be used for the prediction of both depth and bead width for LST of 3 mm thick sheets, but it must be noted that these results were not definitive, as the process was only undertaken to derive a general understanding of the LST process. The whole effect of the LST process parameters on the hourglass fatigue specimens is expounded fully in the following sections. Additional LST experiments were performed at laser powers of 2000 W and 3000 W and at a focus position of 15 mm and scanning speed of 41.7 mm/s (same as previous experiments) to determine the effect of high powers on the two variables, depth of penetration and bead width. It was observed that the increase in power had minimal effect on the bead width and depth of penetration at these parameters. Figure 4-7 shows the results of the additional LST experiments at the above-mentioned parameters. The macrographs of both specimens showed an oval shaped bottom of the LST processed zone.

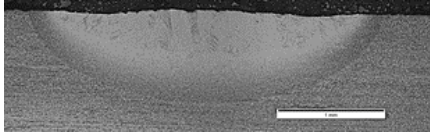
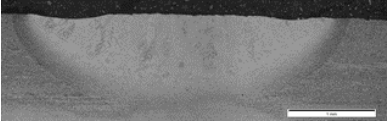
Laser Power, W	2000	3000
Focus position	15	15
Macrograph		
Depth of penetration	0.88	0.7
Bead width	3.11	3.17

Figure 4-7: 2000 W and 3000 W results

4.2.3.1. Hardness analysis

Micro Vickers hardness indentations were made using a 0.5 kg load on the specimens to quantify the hardness differential between the introduced LST region/zone and the parent material. Micro Vickers hardness indentations were made both parallel and perpendicular to the surface, in order to quantify hardness properties in both bead width and depth properties of the LST zone. Figure 4-8 depicts the hardness indentation profile or map. A single hardness indentation was performed for each point.

Note: For all the hardness measurements, the error in the data as a result of operator and machine was calculated to be 1.9 HV.

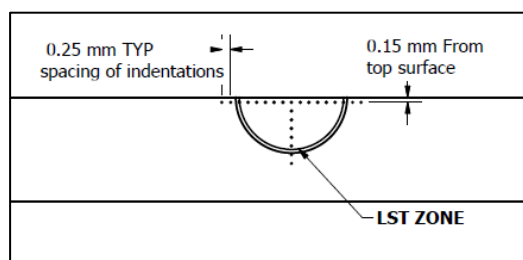


Figure 4-8: Hardness indentations map.

Figure 4-9 illustrates the hardness distribution of the 1000 W; 0 mm (laser power: focus position) in the direction parallel to the surface (horizontal) and the (vertical) perpendicular direction. The hardness distribution in the LST region showed interesting variations. There was a general increase in the hardness distribution in the LST zone from the parent at an average hardness of between 320 and 330 HV to values of above 400 HV in the LST zone. There was also a distinctive hardness peak which coincided with the transition between the LST zone and parent material, therefore in the HAZ. The hardness distribution in both profiles (parallel and perpendicular to the surface) pointed to a quenching effect and high cooling rates during the process of LST.

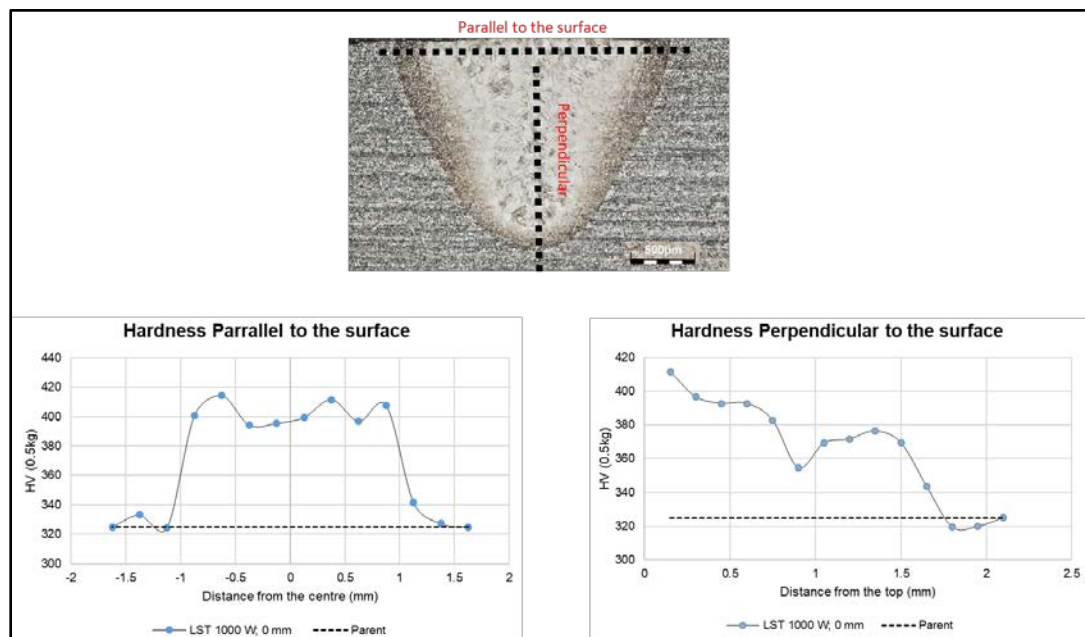


Figure 4-9: Hardness of LST specimens at 1000 W and 0 mm focus position (parallel and perpendicular to the surface).

Figure 4-10 shows the hardness profiles of samples performed at the same laser power but at differing focus positions. It was observed that there was no significant difference in the hardness profile as a result of changing the focus position across the horizontal direction, parallel to the top surface. There was a characteristic hardness peak or increase observed in the HAZ at all hardness profiles of the different focus positions. Figure 4-11 illustrates the 2000 W

hardness profiles at different focus positions. The trend observed for 2000 W trials at different focus positions was similar to that of the 1000 W trials at different focus positions.

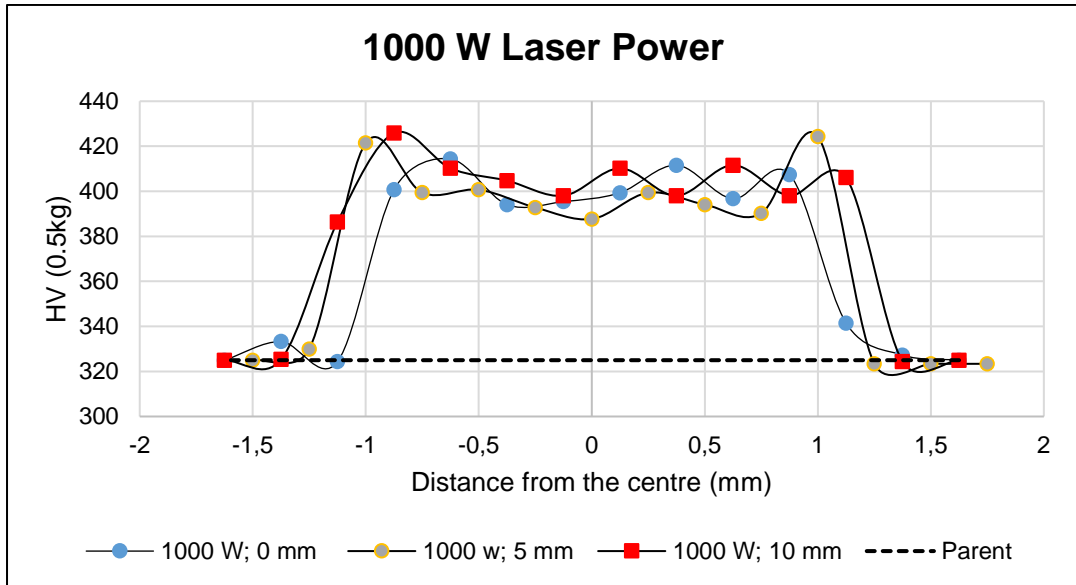


Figure 4-10: Micro hardness profiles of the 1000 W LST specimens at different focus positions.

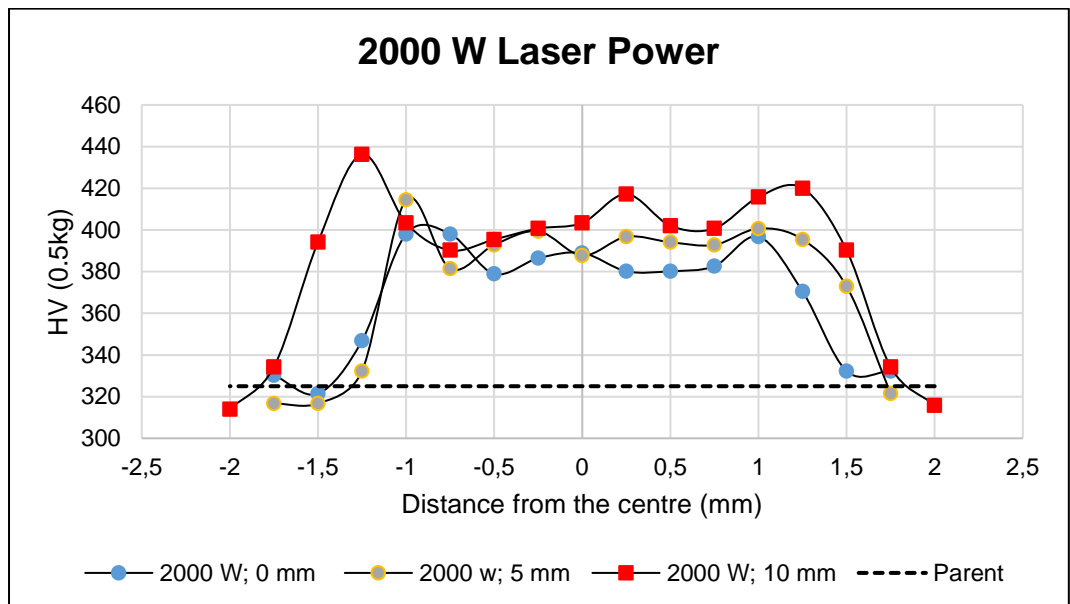


Figure 4-11: Micro Vickers hardness profiles of the 2000 W LST specimens at different focus positions.

Comparing the hardness of both the 1000 W and 2000 W specimens at different focus distance, it was observed that the hardness profiles in the 1000 W specimens followed a similar.

4.2.3.2. Microstructural analysis

Figure 4-12 illustrates the microstructure of the as-supplied Ti-6Al-4V material before the LST process. The microstructure of the parent material shows clear elongated primary $\alpha + \beta$ grains, which corresponds to the annealed state of the received Ti-6Al-4V ELI alloy. The grains show an equiaxed structure, which relates to the as-supplied specifications of the material. This microstructure is a result of cooling from below the beta region.

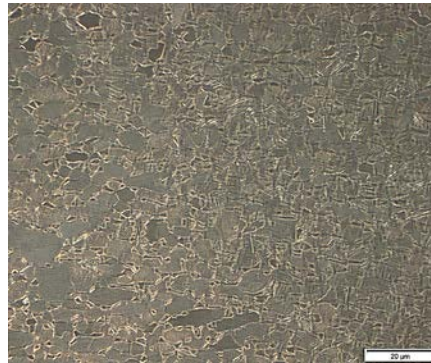


Figure 4-12: Ti-6Al-4V parent microstructure (Polarised light).

After the process of LST, a microstructurally modified track was obtained. The microstructure changes as a result of LST processing were mainly dependent on the temperature conditions during the heating and cooling cycles. In all the cases of the stage one analysis, it was observed that a single characteristic microstructure was obtained. Figure 4-13 shows the attained microstructure of the LST 3 mm sheet at a laser power of 1000 W and defocus of 0 mm. It was noted that the observed microstructure was a fully lamella.

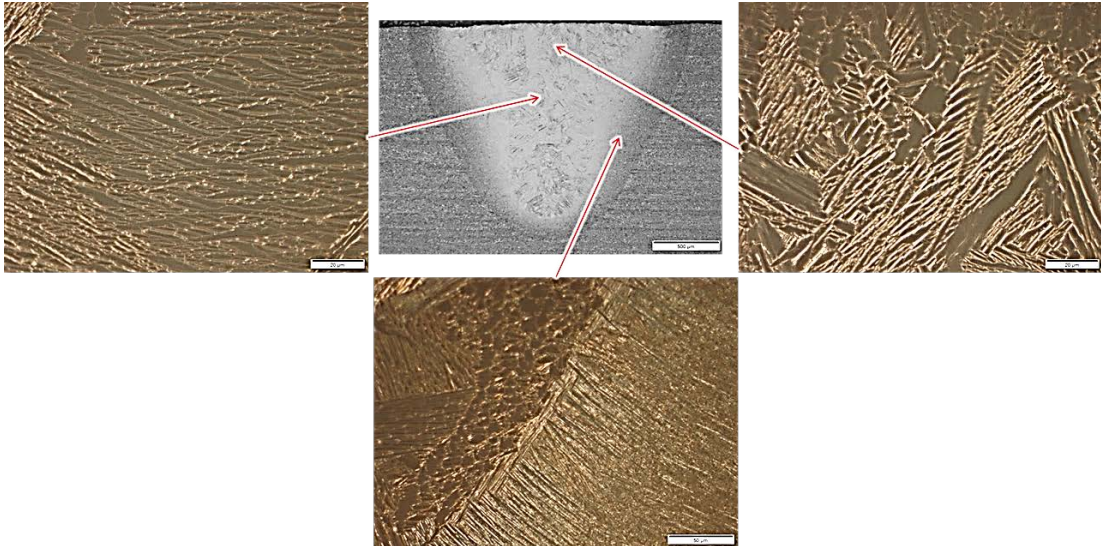


Figure 4-13: Attained microstructure for LST specimen power; 1000 W and focus position, 0 mm.

LST processing introduced two distinct microstructural zones on the 3 mm Ti-6Al-4V sheets. The two microstructural zones were the HAZ and the LST zone and these were compared to the parent material. The microstructure varied between the three zones because of the heat treatment induced on the surface and the cooling rate thereafter. The parent, as shown in Figure 4-12, exhibited equiaxed $\alpha + \beta$ grains while the HAZ displayed coarse lamella grains and the LST fine lamella grains. When cooling occurs from above the β -transus temperature, the resultant microstructure is fully lamella or basket weave structure. The bead width of the α -lamella was measured using Stream software, and the average grain size was found to be 2 μm . These very fine grains, when related to available literature on titanium alloys, show that high cooling rates were involved in this process.

4.2.4. Summary

The results of this section are summarized below:

- Focus position plays a critical role shape of LST region with a high focus position of 10 mm exhibiting an oval shape at the bottom regardless of whether of the laser power. This will be critical especially when performing LST of the cylindrical hourglass specimens. The depth of

penetration decreased with increasing focus position while the bead width was fairly constant with increasing focus position. Due to the specimens being flat this would also have to be studied to show if the same effect would be true for cylindrical specimens. It was therefore concluded that the limits should be 1000 W for laser power while focusing position would be studied further for cylindrical samples.

- The hardness profiles of all the specimens showed a similar profile with an increase in hardness in the LST region compared to the parent material. The microstructure observed after LST processing was fully lamella which related to the hardness increase in the LST region and also indicated that the cooling occurred from above the beta transus temperature.

LST of cylindrical samples would require multiple surface treatments which might affect the homogeneity of the microstructure and hardness around the specimen. The following sections will study this further.

4.3. Stage 2: Laser Surface Treatment Strategy

4.3.1. Introduction

This section details the second stage of the LST process development. At the inception of this project, one of the main considerations was how to conduct LST on cylindrical “hourglass” fatigue geometry specimens. In this second stage, two types of strategies were analysed. The first strategy utilised was a continuous treatment strategy, which involved having the laser beam follow a continuous profile or path. A second novel strategy was also implemented that gave varying results to the continuous treatment sequence. This second strategy involved the use of a non-continuous strategy. The following sub-sections explain both these strategies in detail.

4.3.2. Experimental set-up

The experimental set-up utilised for both the continuous and non-continuous strategy was similar. The LST process was performed on the parent “hourglass” fatigue test geometry specimens purposely designed for this research. Figure 4-14 shows the experimental set-up utilised for the LST process.

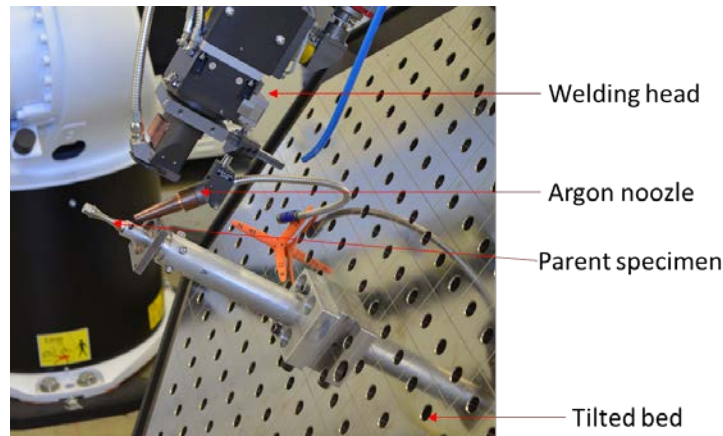


Figure 4-14: Weld experimental set-up.

4.3.3. LST strategy 1: Continuous

Figure 4-15 shows the continuous treatment strategy. Continuous treatment meant that the laser surface treatment runs followed each other around the full diameter of the hourglass specimen. For example, the laser beam starts treatment at point A to point B, and then stops while the bed rotates 20 degrees to point C. From point C, the laser beam does the second treatment run, C to point D and this process continues until 360 degrees has been covered. It was envisaged that for every 20 degree bed rotation, the desired 50% overlap at specified laser power and focus position would be achieved.

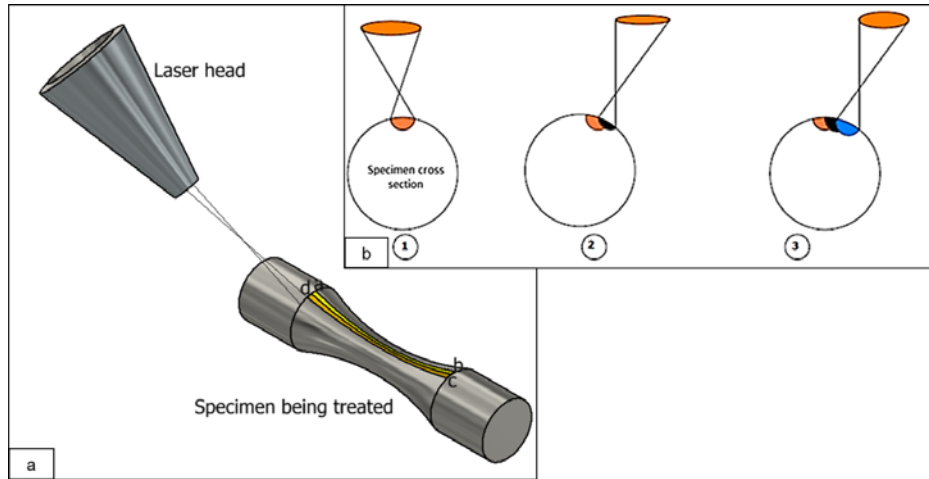


Figure 4-15: LST strategy 1 a) profile followed on the specimen b) expected cross section of LST strategy 1.

Figure 4-16 shows visual images of the specimens that were processed using LST. From the visual images, the specimens displayed a surface finish of brown appearance. The brown discolouring observed on the specimens was due to high energy inputs of 16.2 J/mm and 24 J/mm corresponding to laser power of 675 W and 1000 W respectively at a scanning speed of 41.7 mm/s (0.0417 m/s), with a lack of adequate shielding. The 1000 W specimen showed a more pronounced darker appearance which could be a result of oxidation.



LST specimen	LST 1	LST 2
Laser Power (W)	1000	675
Focus position (mm)	+5	+5
LST visual image		

Figure 4-16: LST visual images of 675 W and 1000 W specimen.

An area of interest arose, that being the laser beam travel length. The total treatment length of the laser beam was 33.4 mm. The total amount of energy per single treatment line irradiated into the specimen was therefore the product of energy input and the travel length (refer to Equation 4). It was therefore noted that reducing the treated area decreased the energy input. This will be expounded upon in the following sub-sections.

$$\text{Total Energy Input (J)} = \text{Energy Input (J/mm)} \times \text{laser beam travel length (mm)} \quad (4)$$

Figure 4-17 and Figure 4-18 show images of the 675 W and 1000 W cross-sections. The yellow line indicates the start position of LST while the red arrow indicates LST direction.

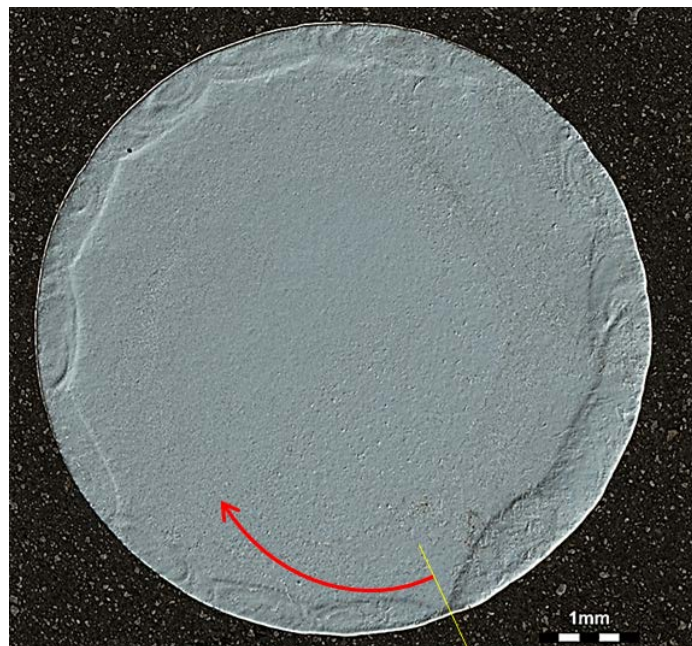


Figure 4-17: LST 1 (675 W, red arrow shows treatment direction).

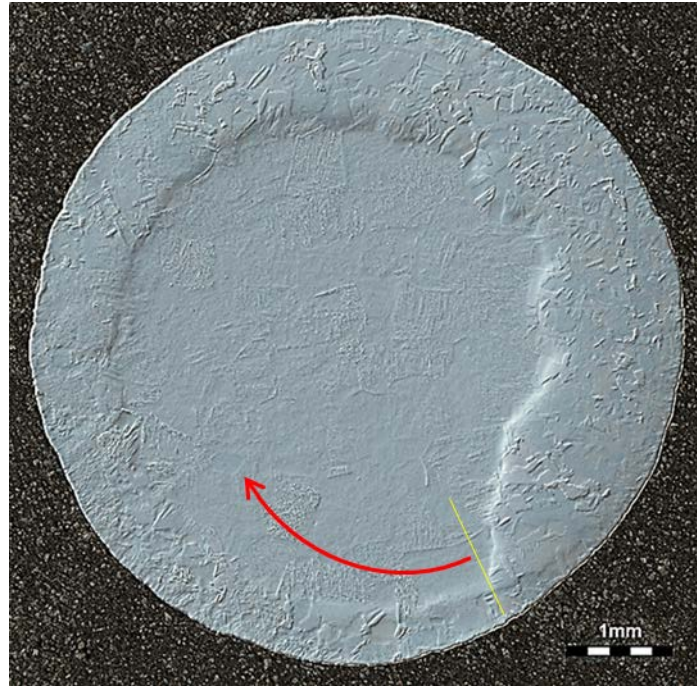


Figure 4-18: LST 2 (1000 W, red arrow shows treatment direction).

From the LST cross sections, it was observed that the LST treatment strategy 1 (continuous) exhibited an uneven laser depth penetration around the specimen. This uneven depth of penetration can be explained by the fact that at the start of the process the specimen is cold, leading to a low initial depth of penetration. As the process continues the temperature of the specimen increases with each following laser treatment run. Ti-6Al-4V ELI has a low thermal conductivity (6.7 W/m-K) when compared to other materials, for example, aluminum (Aluminum 6061-T6, 167 W/m-K). Owing to the low thermal conductivity, Ti-6Al-4V ELI slowly dissipates heat. This temperature difference, in turn, affects the microstructure attained between the start and end positions, leading to a hardness variation in the LST zone.

The microstructure of the specimen was analysed to quantify the effect of microstructure development after the LST process. The microstructure attained in the LST zone of both specimens was purely lamella. The resultant microstructure was the result of processing occurring above the β -transus temperature, then rapid cooling. Figure 4-19 shows the microstructure variations between the start and end of the LST process (1000 W specimen).

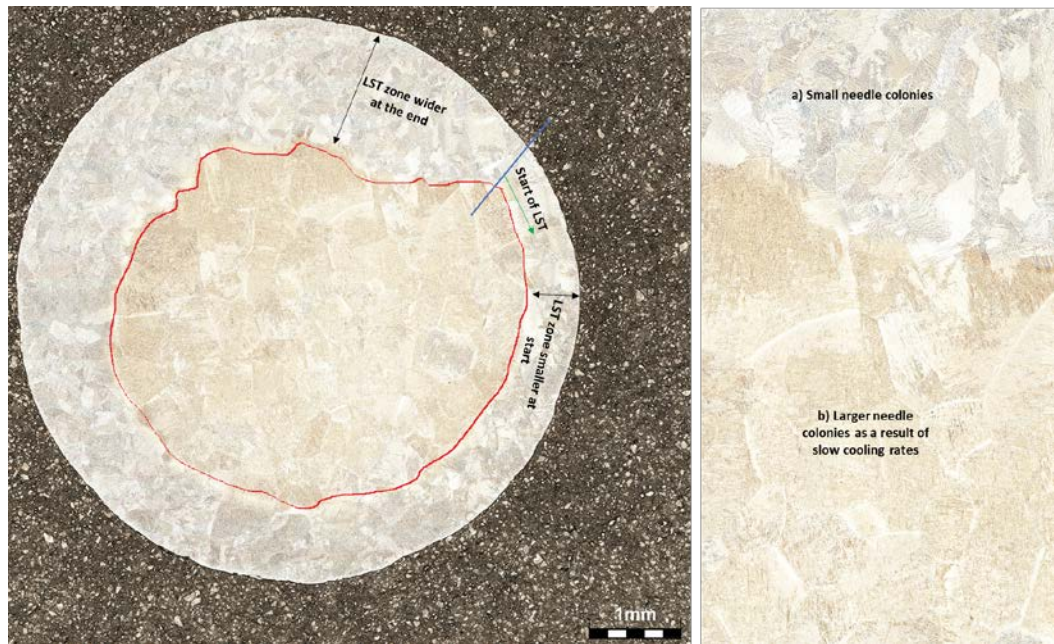


Figure 4-19: LST 1000 W microstructural analysis showing effect of continuous LST strategy and difference between the needles in the colonies.

4.3.4. LST strategy 2: Non-continuous

In order to combat the issue of the uneven depth of penetration discussed in sub-section 4.3.3, continuous treatment strategy, the following measures were implemented:

- LST strategy 2: a non-continuous treatment method was developed as opposed to the LST strategy 1, continuous. LST strategy 1 involved the bed being rotated in a continuous sequence while LST strategy 2 entailed conducting the LST process in a non-continuous manner. Figure 4-20 shows LST strategy 2, implemented in order to combat the unevenness of the attained LST depth of penetration on the specimen. The laser treatment lines are denoted by 1, 2, and 3, with 1 being the first laser treatment followed by 2 at 180 degrees, then 3 at 90 degrees from 2 and so on until the whole diameter of the specimen has been LST treated.

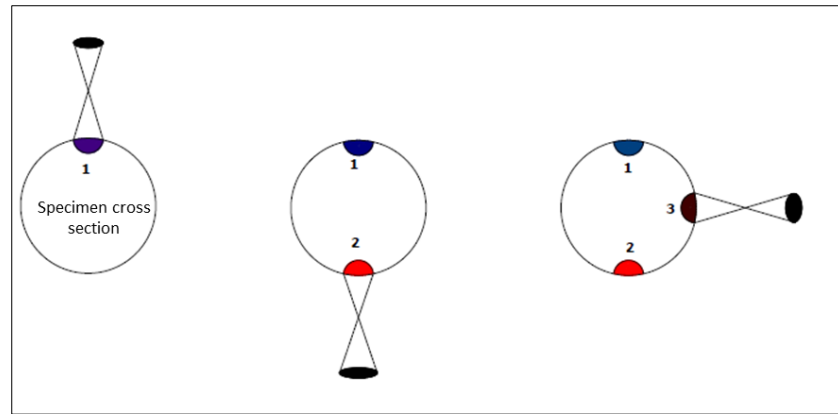


Figure 4-20: LST strategy 2 non- continuous scan (from 1 to 2, 3, etc.).

- In addition, it was decided to shorten the length of the LST scan from 33.4 mm to only 10 mm. 10 mm was seen as being adequate as the RFW weld region is approximately 2 mm.

Figure 4-21 shows the visual images of a respective continuous and non-continuous strategy, as a result of the implementation of the above stated measures. By shortening the length, the total energy input into the specimen (refer to Equation 4) would decrease from 540.6 J to 162 J as per the 675 W specimen shown in Figure 4-20. This change would effectively reduce the amount of input energy by approximately 70 % for each laser beam treatment run.



	LST strategy 1 (Continuous)	LST strategy 2 (non- continuous)
		
Energy Input per length (J/mm)	16.2	16.2
Treatment length (mm)	33.4	10
Energy Input (J) per single treatment	541.1	162

Figure 4-21: Visual image of LST specimens

LST strategy 2 improved the evenness of the depth of penetration around the specimen diameter. The sample had a uniform LST zone, which was one of the requirements for a successful LST strategy. Figure 4-22 shows the third LST specimen conducted using LST strategy 2 (non-continuous) with uniform depth of penetration all around it. Therefore, a non-continuous LST strategy improved the uniformity of the LST zone.

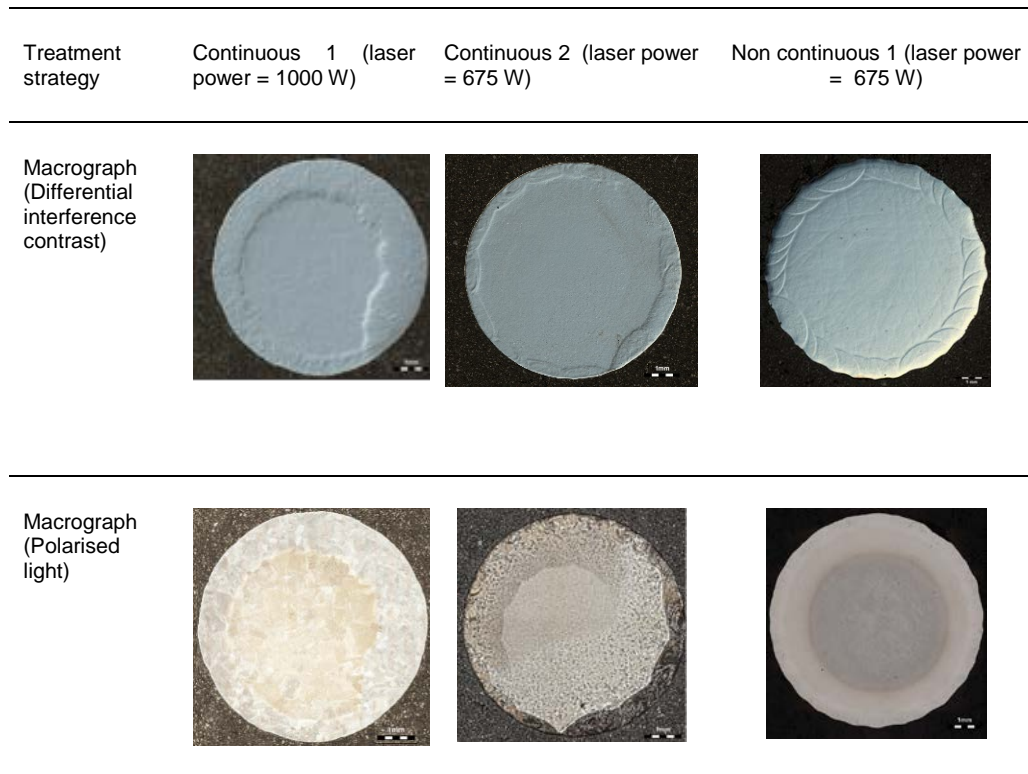


Figure 4-22: Effect of LST strategies on depth of penetration.

The depth of penetration of three specimens was analysed. Figure 4-23 details the depth of LST penetration of the LST zone from the beginning of the LST process to the end (to start at 0°, to end, 360°). LST strategy 1 (continuous) showed an increase in the depth of penetration of the LST zone from start to finish with the plotted data exhibiting a linear relationship. Factors driving this linear relationship were the low scanning speed and the continuous strategy during treatment, which led to heat build-up in the sample with each LST run. By the time the treatment of the specimen had finished, the specimen temperature had increased considerably as compared to its initial temperature at the start of treatment. LST strategy 2, non-continuous, was introduced and the outcome was a uniform LST depth all around the cross-section of the specimen as displayed in Figure 4-22 (LST 2).

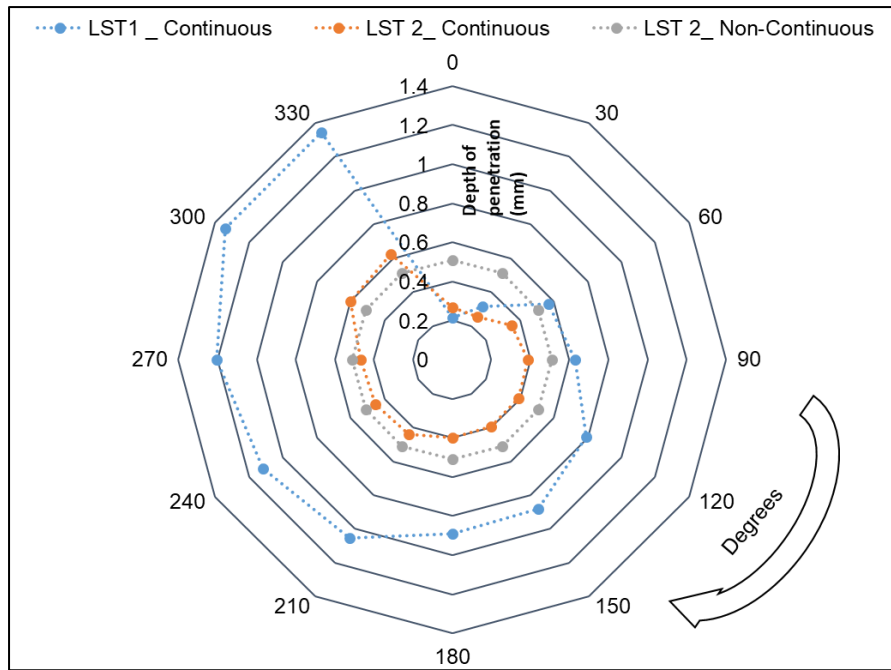


Figure 4-23: LST depth of penetration measurements on cross section analysis.

Micro Vickers hardness tests were conducted to quantify the effect of the LST strategy on the start and end, finish of the LST process. Table 4-2 tabulates the effect of changing the LST strategy from a continuous to a non-continuous strategy on hardness distribution. As predicted, average hardness values in the LST strategy 2 specimens were almost constant when compared to the LST strategy 1 specimens. Therefore, this LST non-continuous strategy improved the temperature distribution within the specimen, almost eliminating the cold '*start*' and hot '*end*'.

Table 4-2: Hardness (start and finish) 0.125 mm from the outer edge of the specimen.

Specimen name	Laser Power (W)	Start of LST average hardness (HV)	Finish of LST average hardness (HV)	Difference (HV)
LST 1 (Continuous)	1000	505	603	98
LST 1 (Continuous)	675	331	385	54
LST 2 (Non Continuous)	675	345	363	18

4.4. Stage 3: Final Experimental Matrix

4.4.1. Introduction

After the first two stages, it was concluded that further analysis would be conducted using low laser powers which meant maximum laser power would not exceed 1000 W as high laser power led to high depths of penetration and in extreme cases oxidation. Using low power would also make the process more efficient. The final matrix was used to quantify the effect that process parameters have on the LST process. The parameters analysed were focus position, scanning speed and laser power. Important process parameter interactions were established. These are further discussed in this section. Temperature measurements were conducted to determine whether the LST process was a repeatable process and therefore, easily repeatable. Figure 4-24 details the LST process development procedure from the as received material to the final LST specimen.

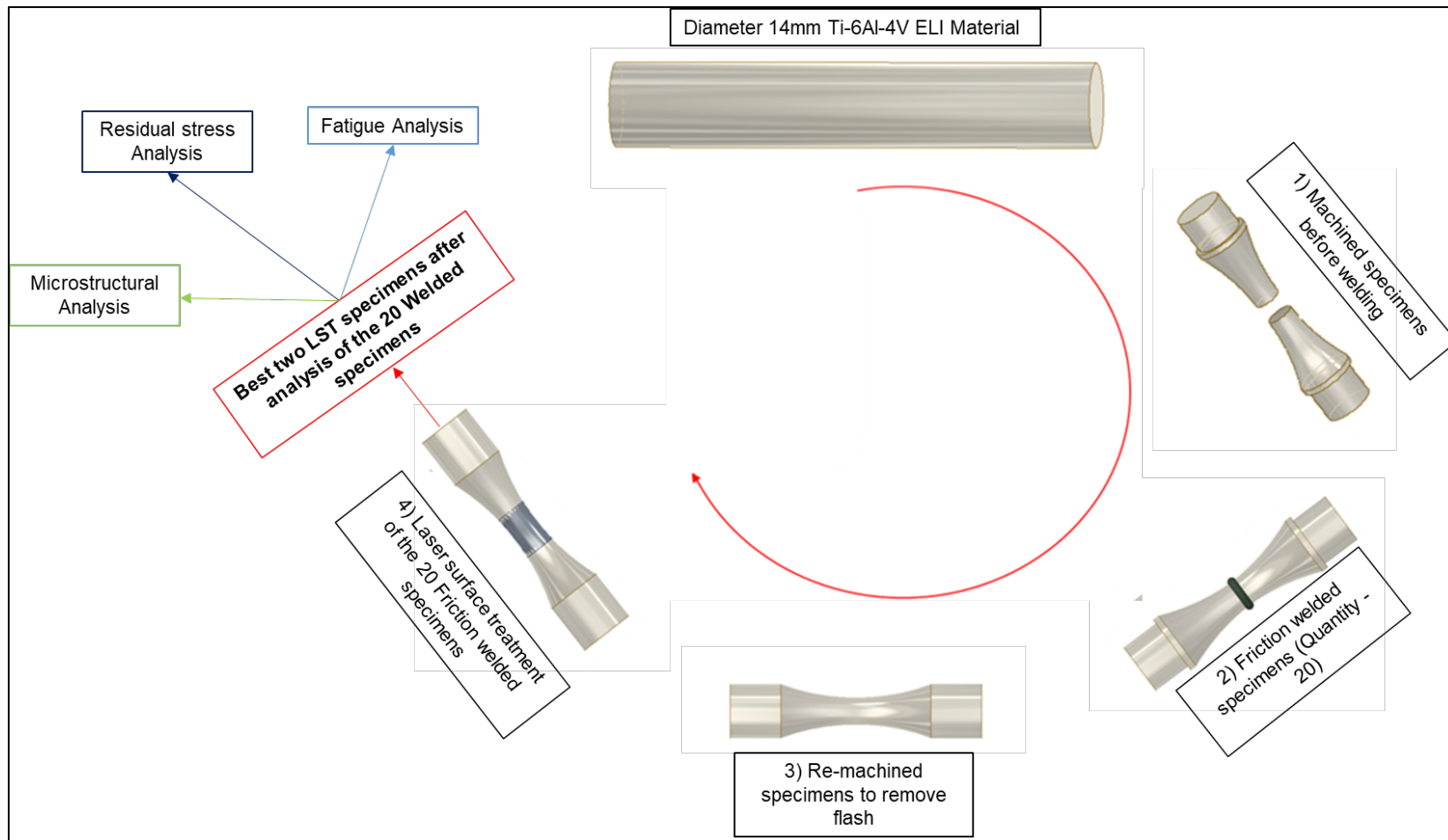


Figure 4-24: LST process development schematic.

4.4.2. Experimental Design

The final matrix experimental design was undertaken using the Central Composite Design (CCD) method. The CCD comprised of three variants; laser power, scanning speed and focus position, therefore the resulting CCD was a 3-variable matrix. The first important step was to determine the process limits of the experiments to be conducted. As discussed in previous sections, it was resolved to conduct the LST process at low laser powers in order to make the process more efficient and cost-effective for large-scale implementation [74]. Table 4-3 tabulates the process limits used in the experimental matrix design.

Table 4-3: Experimental domain star points.

Experimental Domain (Star points)		
	Min	Max
Laser Power (W)	250	1000
Scanning Speed (mm/s)	30	120
Focus Position (mm)	2,5	10

From these process limits, an experimental matrix was established as shown in Table 4-4. The number of friction welded specimens to be laser surface treated was twenty, one for each experimental process trial. The LST runs were not in order but randomised. The main motivation for randomisation was to remove some of the subjectivity from the experiment and to offer protection from systematic but unknown or unaccounted for factors affecting the value of the response variable, in this case, temperature.

Table 4-4: Final experimental matrix showing the varied process parameters.

LST Run	Laser Power (W)	Scanning Speed (mm/s)	Focus Position (mm)
1	625	75	6
2	625	30	6
3	402	48	4
4	625	120	6
5	625	75	6
6	402	102	8
7	848	48	8
8	625	75	6
9	402	48	8
10	625	75	6
11	250	75	6
12	848	102	4
13	625	75	10
14	625	75	6
15	848	48	4
16	848	102	8
17	625	75	3
18	402	102	4
19	1000	75	6
20	625	75	6

4.4.3. Experiment set-up

Temperature was measured by means of a thermocouple which was inserted into the particular RFW specimen to undergo LST processing. The thermocouple was located in the centre through to the mid-section of the specimen. Figure 4-25 shows the location of the thermocouple in a specimen to undergo LST processing. The friction welded specimens had the flash removed before LST was conducted. The sequence of steps for specimen preparation is depicted in Figure 4-26.

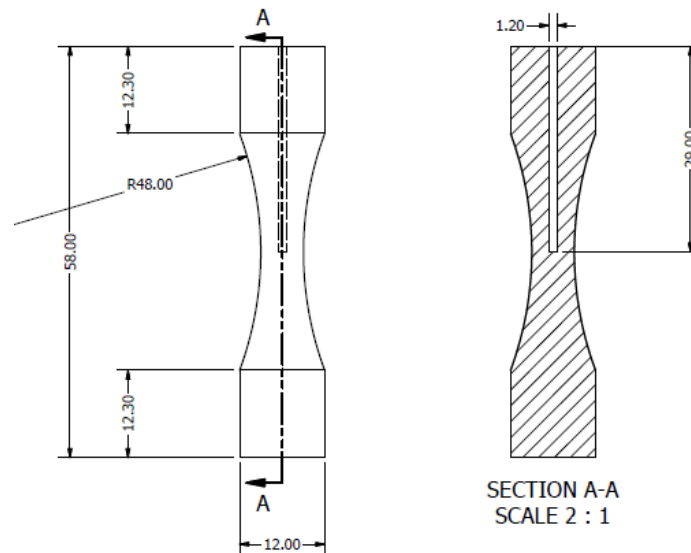


Figure 4-25: Hole position for thermocouple inserted in the specimen undergoing LST processing.

Figure 4-27 shows the LST process from position A to B without the thermocouple for better visualization of the process. The experimental set-up utilised was the same as the one detailed in section 4.2.2 and Figure 4-14 with the exception of the added tempoint which was used for temperature measurement. For statistical reasons, the temperature measured was used as a response variable. It is important to note that this temperature was measured inside the specimen, and therefore, it can not be used as a direct representation of the surface temperature. Unfortunately, for this study, the measurement of surface temperature during LST could not be conducted due to safety reasons. The laser system is housed in a laser cell which is closed during the LST process and the laser operator stands outside, observing through a small window.

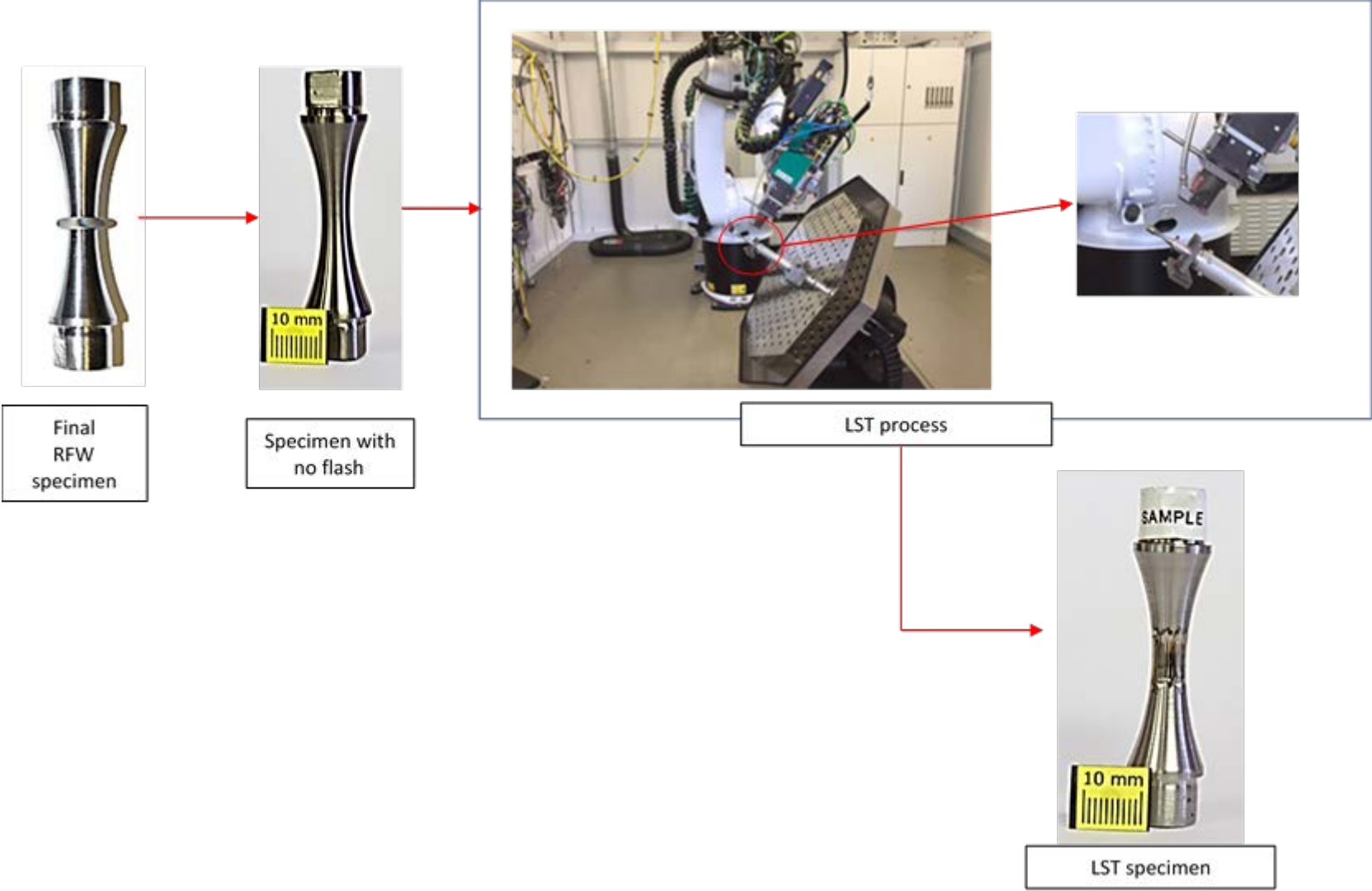


Figure 4-26: From RFW to final LST specimen.



Laser Beam at position A



Laser Beam scanning the specimen A to B:
10 mm travel length



Laser Beam at position B, waiting for bed to rotate 180 degrees: non-continuous strategy

Figure 4-27: LST process for the final matrix.

4.4.4. Statistical Analysis

The response (dependent) variable that was measured, “temperature”, was used to check whether the LST process is **repeatable** through a statistical analysis. Temperature measured is not used in the determination of final specimens for continuing analysis but was used as this could be directly measured while the LST was being performed. Table 4-5 shows the maximum attained temperature for each experimental laser run.

Table 4-5: Measured temperature for each experimental run.

LST Run	Laser Power (W)	Scanning Speed (mm/s)	Focus Position (mm)	Measured Temperature at the centre specimen (°C)	Energy Input (J/mm)	Power density (W/mm ²)
1	625	75	6	137.9	8.33	795.8
2	625	30	6	243.2	20.83	795.8
3	402	48	4	130.5	8.33	1211.5
4	625	120	6	116.1	5.21	795.8
5	625	75	6	171.1	8.33	795.8
6	402	102	8	104.7	3.95	302.9
7	848	48	8	310.8	17.58	638.9
8	625	75	6	171.4	8.33	795.8
9	402	48	8	185.0	8.33	302.9
10	625	75	6	171.7	8.33	795.8
11	250	75	6	98.0	3.33	318.3
12	848	102	4	163.9	8.33	2555.5
13	625	75	10	198.5	8.33	310.8
14	625	75	6	179.0	8.33	795.8
15	848	48	4	348.1	17.58	2555.5
16	848	102	8	171.8	8.33	638.9
17	625	75	3	202.2	8.33	2630.7
18	402	102	4	90.5	3.95	1211.5
19	1000	75	6	220.0	13.33	1273.2
20	625	75	6	170.8	8.33	795.8

LST runs 1, 5, 8, 10, 14 and 20 represented the repeated parameter selection during the experimental runs. These repeat LST runs were conducted at the

same process parameters with the maximum attained temperature almost identical. Figure 4-28 shows the process curves of the 6 repetitive experimental runs. From these runs, it was observed that the LST process is highly repeatable. The maximum temperature observed in LST 1 was lower than the others because of an experimental error (initial Argon gas flow rate was set higher at 15 L/min then reduced to 10 L/min) but was still deemed acceptable to fit within the analysis. From the graph, the temperature at the start of the process of LST is 28 °C, which related to the temperature in the laser cell during the experimental trials. Using the repeat experimental runs, the error in the measured maximum temperature is 14 °C and if LST 1 is excluded, the error is 4 °C.

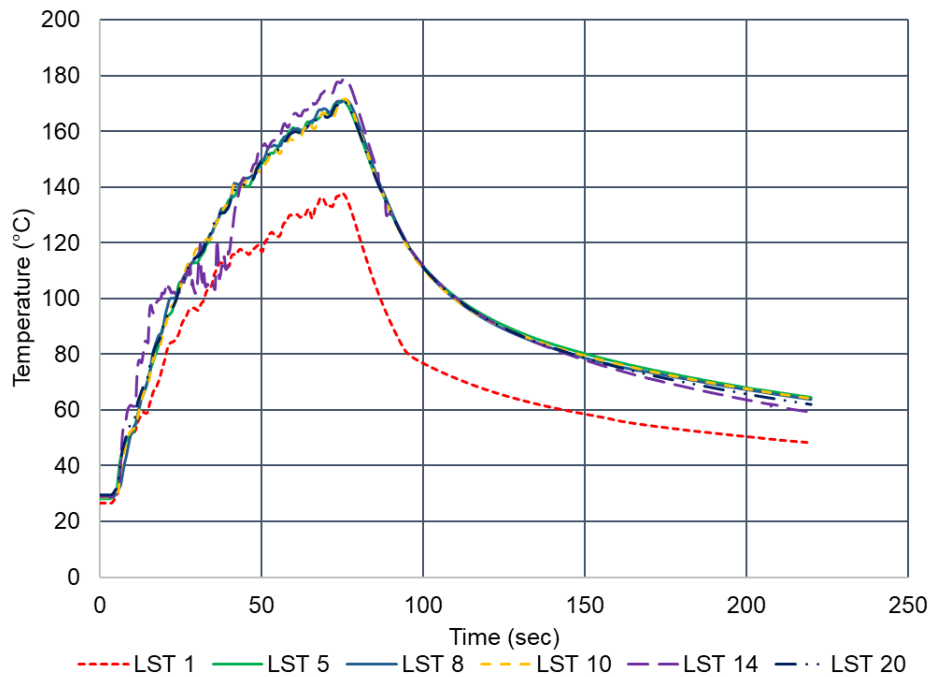


Figure 4-28: Repeated experimental runs.

Equation 5 and Table 4-6 show the developed statistical regression model.

Note: For Table 4-6 and Equation 5, abbreviations are utilised for scanning speed, laser power and focus position, SS, LP and FP respectively, while in the rest of the report the full name is used for these individual process parameters. The model equation also includes parameters with p-values greater than 0.05 which will be explained later.

The model equation was as follows:

$$T = b_0 + b_1LP + b_2SS + b_3FP + b_4FPn^2 + b_5LP.SS \quad (5)$$

Table 4-6: Model results after regression analysis.

		b	Standard Error	p-value
b0	Intercept	61.77	87.70	0.49
b1	LP	0.54	0.11	0.0002
b2	SS	0.86	0.89	0.35
b3	FP	-31.86	17.63	0.09
b4	FP ²	2.65	1.38	0.08
b5	LP*SS	0.00	0.00	0.01

Profile plots for scanning speed, laser power and focus position are shown in Figure 4-29, Figure 4-30 and Figure 4-31.

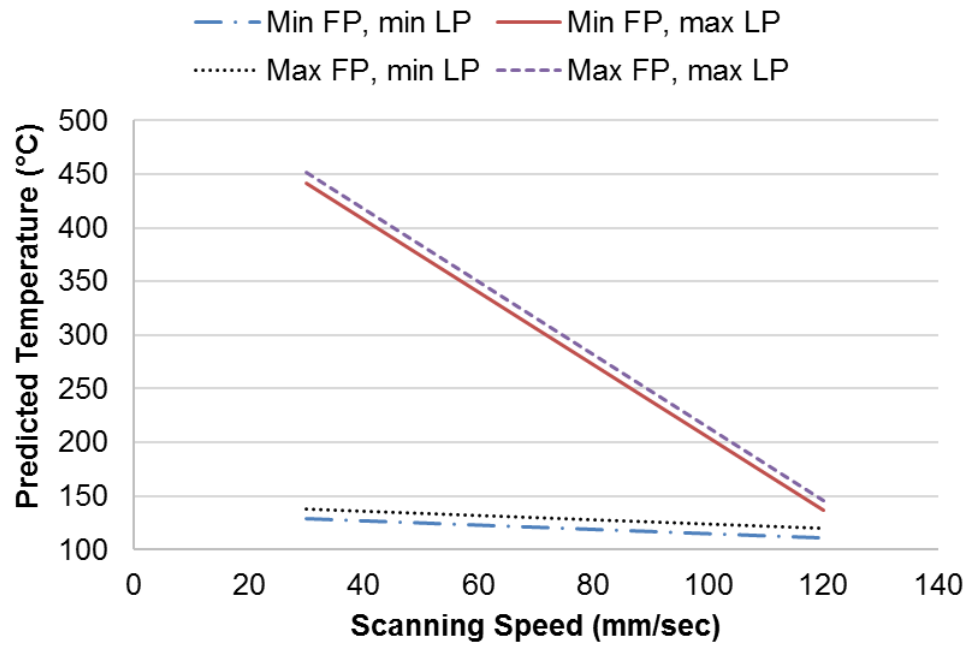


Figure 4-29: Profile plot of temperature vs scanning speed.

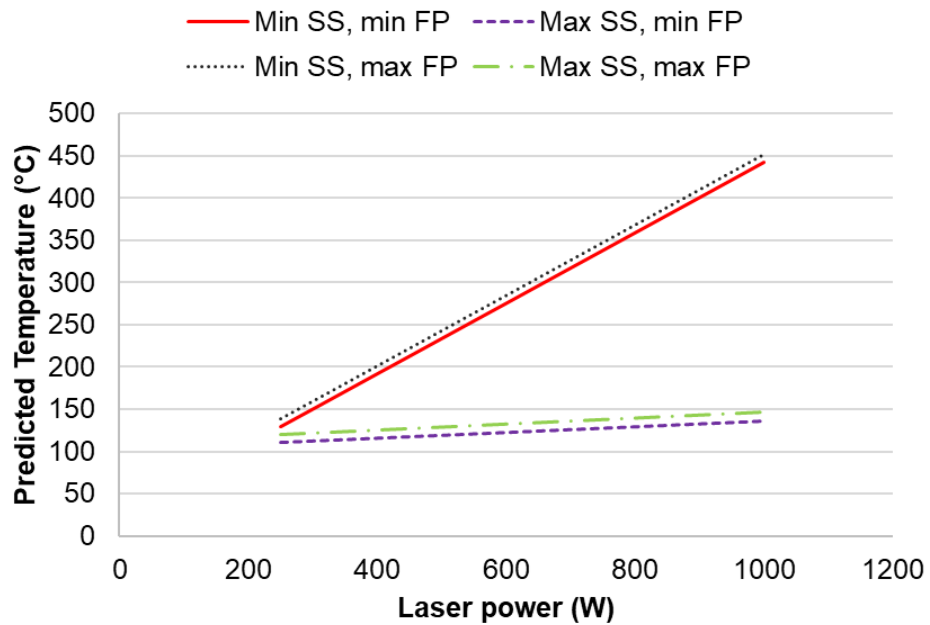


Figure 4-30: Profile plot of temperature vs laser power.

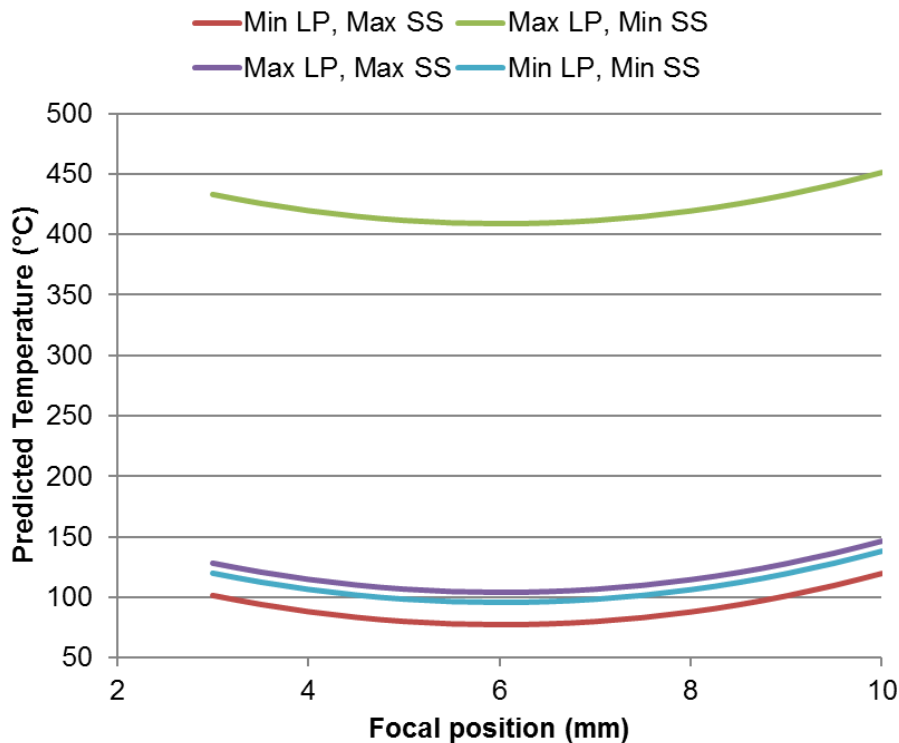


Figure 4-31: Profile plot of temperature vs focus position.

The following conclusions were established with reference to the regression model that was determined (refer to Equation 5):

- Although the effect of focus position (FP_n and FP_n^2) is minimal, evidence of a non-linear effect on temperature was observed. The p-values for FP_n and FP_n^2 are 0.09 and 0.075 (above p-value of 0.05) respectively, highlighting this minimal effect on temperature.
- The model showed that scanning speed and focus position do not interact. It was concluded that the effect of scanning speed on the temperature was not influenced by focus position. Scanning speed alone was insignificant with a p-value of 0.35 (above p-value of 0.05) but is included in this model because of its strong interaction with laser power.
- The effect of laser power on temperature was linear (refer to Figure 4-30).
- Similarly, as with laser power, scanning speed had no quadratic effect on the temperature, only a linear effect (refer to Figure 4-29).

- The effect of laser power was not influenced by focus position. The profile plot for focus position showed that focus position had minimal effect on the sample temperature.

The main observation is that there was a strong antagonistic effect between laser power and scanning speed, with the effect of laser power on temperature negatively influenced by increasing scanning speed. The p-value (0.008) of the product of laser power and scanning speed was very low, showing a high correlation between the two process parameters. A p-value below 0.05 indicates a high significance of the parameter being analysed. Therefore, energy input can be kept constant by varying either laser power or scanning speed.

4.5. Final Matrix Analysis

The final matrix analysis section details the process in which the final two specimens were selected for further analysis by EBSD and synchrotron X-ray diffraction technique for microstructure and residual stresses respectively. The total number of LST specimens analysed was fifteen instead of the experimental matrix's twenty. The five specimens omitted, represented the experimental repeat runs of the final matrix as tabulated and explained in Table 4-5 and section 4.4.4 respectively. Energy input was used to group the specimens into three categories which were low, medium and high. For a specimen to be classified in the low energy input category, the maximum energy input could not exceed 6.5 J/mm. The medium energy input category was considered to be between 6.5 J/mm and 13.0 J/mm and an energy input above 13.0 J/mm considered to be high energy input. Only two specimens were selected for further characterisation because of the cost of running these aforementioned tests. The selection criteria involved an analysis of the visual images, macrostructure and hardness distribution of the LST specimens. Figure 4-32 shows the selection process that was followed.

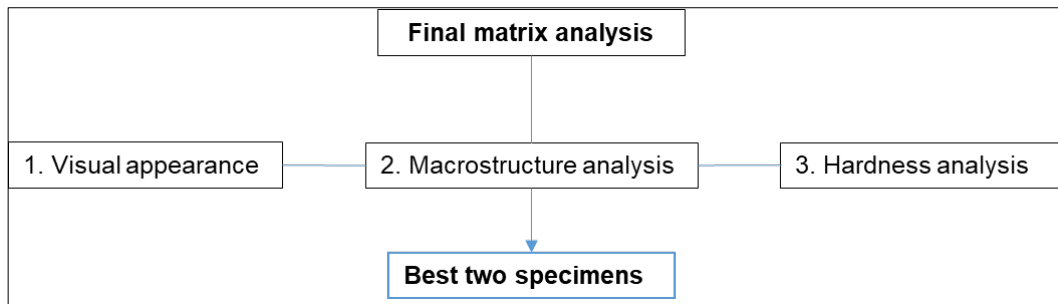


Figure 4-32: Illustration of the selection process for the final analysis.

4.5.1. Visual Inspection

Figure 4-33 shows examples of the LST specimens produced in the final experimental matrix. The visual images show the region that was LST processed which was approximately 10 mm in length. It was observed that at high energy input the specimens' surface showed evidence of oxidation discolouring and was highly degraded compared to the low and medium specimens.

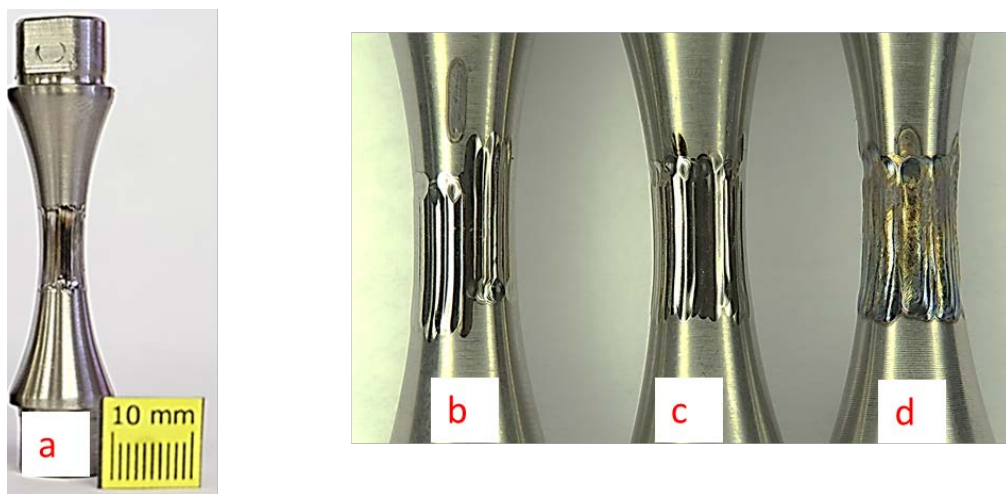


Figure 4-33: Examples of random visual images of the final matrix, a) example of full specimen, b) low energy input (LST 4), c) medium energy input (LST 1) and c) high energy input (LST 7).

Another observation drawn from the visual images was that at a high scanning speeds of 102 mm/s and above, the treated area became uneven. This was mainly due to the control system of the laser robot, which made it difficult for

the laser robot to stop at the exact distance of 10 mm from the treatment start position at high scanning speeds. This resulted in some LST processing lines not being in the correct position. At low speeds, this problem was not visible. Therefore, the scanning speed was limited to a maximum of 75 mm/s. Figure 4-34 shows the effect of scanning speed on the LST processing lines between two specimens at scanning speeds of 75 mm/s and 102 mm/s respectively, illustrating the above-explained difference.

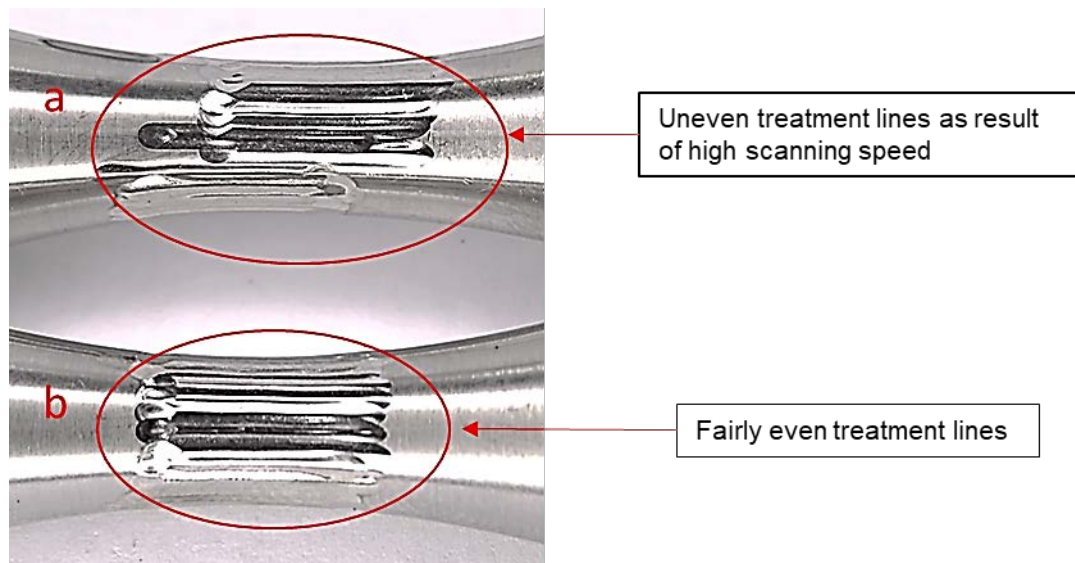


Figure 4-34: Two LST specimens at different scanning speeds a)102 mm/s b) 75 mm/s.

4.5.2. Macrostructure analysis of LST specimen

The LST specimens were cross sectioned in the direction perpendicular to the treatment direction shown in Figure 4-35 and then mounted, ground and polished. Polishing was performed using a semi-automatic polishing machine. The polishing process took approximately 30 s using 320 Grit paper, followed by 3 minutes on the Largo diamond using 9 μm allegro and lastly 4 minutes on the polishing cloth using 1 μm Oxide Polishing Suspension (OPS). After polishing, the specimens were etched using a mixture of 2 ml HF (40%), 5 ml H_2O_2 (30%) and 100 ml H_2O .



Figure 4-35: Example of perpendicular cross section used for analysis.

Table 4-7 shows the cross-sectional appearance of the LST specimens of the final matrix grouped in different energy input levels. Table 4-7 shows macrograph examples of the three different energy input categories. Remaining LST specimens can be seen in Appendix C. Table 4-8 displays the measured LST depth of penetration from the macrographs of the resultant specimens.

Table 4-7: Macrographs of the three different energy input levels.







Energy input level	Low		Medium		High (showing effect of different power densities)	
Macrograph						
LST specimen	4	18	1	16	2	15
Energy Input (J/mm)	5.21	3.95	8.33	8.33	20.83	17.58
Power density (W/mm ²)	795.8	1211.5	795.8	638.9	795.8	2555.5
Scanning speed (mm/s)	120	102	75	102	30	48
Focus position (mm)	6	4	10	8	6	4
LST depth of penetration (average) (mm)	0.22	0.35	0.39	0.25	0.83	0.84

Table 4-8: Average LST depth of penetration.

LST Run	Energy Input (J/mm)	Power density (W/mm ²)	Average LST depth of penetration (mm)	Comment
1	8.33	795.8	0.39	
2	20.83	795.8	0.95	High energy input = a largest LST
3	8.33	1211.5	0.46	Medium energy input
4	5.21	795.8	0.22	Low energy input = small LST zone
6	3.95	302.9	0.20	Low energy input and power density
7	17.58	638.9	0.83	High energy input
9	8.33	302.9	0.27	
11	3.33	318.3	0.16	Low energy input and power density = smallest LST zone
12	8.33	2555.5	0.42	
13	8.33	310.8	0.56	
15	17.58	2555.5	0.84	High energy input and power density = largest LST zone
16	8.33	638.9	0.25	
17	8.33	2630.7	0.65	
18	3.95	1211.5	0.35	
19	13.33	1273.2	0.63	

High energy input specimens had the maximum attained LST zone depth. LST specimens 07 and 02 had LST average depths of 0.83 mm and 0.95 mm respectively. Comparing the representative high energy input specimens, as shown in Table 4-7, the main difference between the two specimens in this energy level was the power density with a high power density affecting the uniformity of depth of penetration around the specimen's diameter. For example, with the high-power density specimen, at the start of LST processing, the average depth was 0.49 mm gradually increasing to 0.81 mm at the mid

position and 1.23 mm at the end of the LST processing. Aside from the uneven depth at high energy input and high power density, the evidence of voids in the LST zone was another area of concern. The resultant voids were as a result of the high temperatures and uneven cooling rates, leading to a lack of homogeneity in the LST zone as material cools and consolidates.

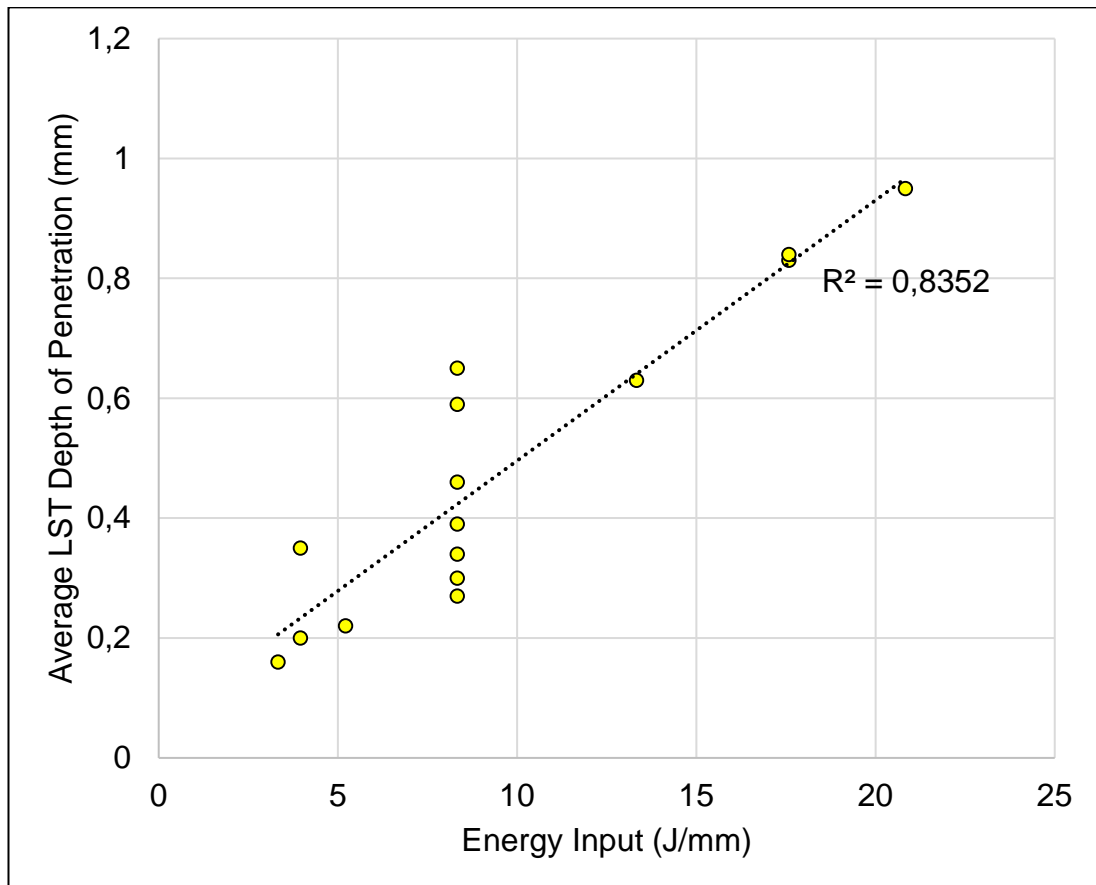


Figure 4-36: A comparison of energy input versus LST depth of penetration.

Figure 4-36 graphically depicts the relationship between energy input and LST depth of penetration. From the graph, the following was concluded;

- The depth of penetration of the LST zone increased with an increase in energy input.
- Also at constant energy input the LST depth of penetration also increased. This increase in depth of penetration was as a direct result of increasing power density. Table 4-9 shows the seven LST

specimens analysed at a constant energy input of 8.33 J/mm with varying power densities. Figure 4-37 graphically illustrates the effect of increasing power density on the LST depth of penetration.

Table 4-9: Medium Energy Input LST depth of penetration analysis.

LST	Energy Input (J/mm)	Power density (W/mm ²)	LST depth of penetration (mm)
1	8.33	795.8	0.39
3	8.33	1211.5	0.46
9	8.33	302.9	0.27
12	8.33	2555.5	0.59
13	8.33	310.8	0.34
16	8.33	638.9	0.3
17	8.33	2630.7	0.65

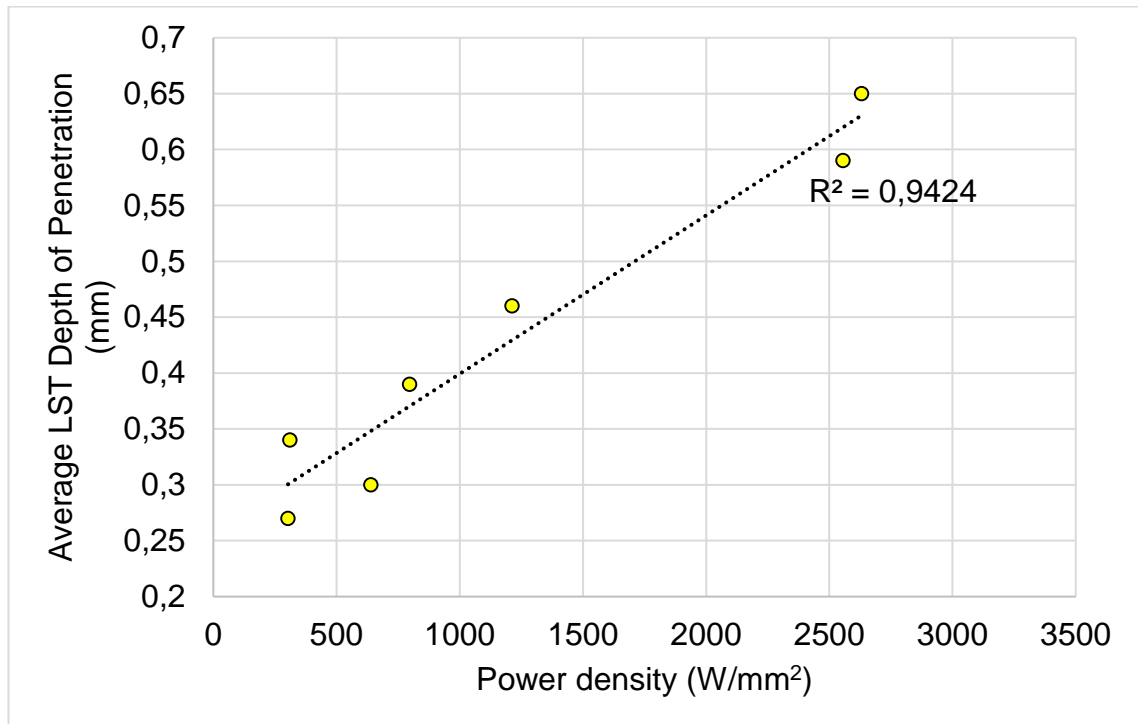


Figure 4-37: Power density vs LST depth of penetration at constant energy input.

4.5.3. Hardness distribution of Laser Surface Treated Specimens

Micro Vickers hardness profiles were measured for the three energy input levels: low, medium and high. Consistent with previous hardness

measurements, indentations were made using a 0.5 kg load at a dwell time of 15 seconds across the centre of the sectioned macrographs with spacing of 0.125 mm. Figure 4-38 displays results of hardness measurements on three LST specimens 04, 01 and 02, representing the low, medium and high energy inputs respectively. These specimens chosen for hardness analysis were conducted at varying energy inputs but had similar or closely relatable power densities for consistency.

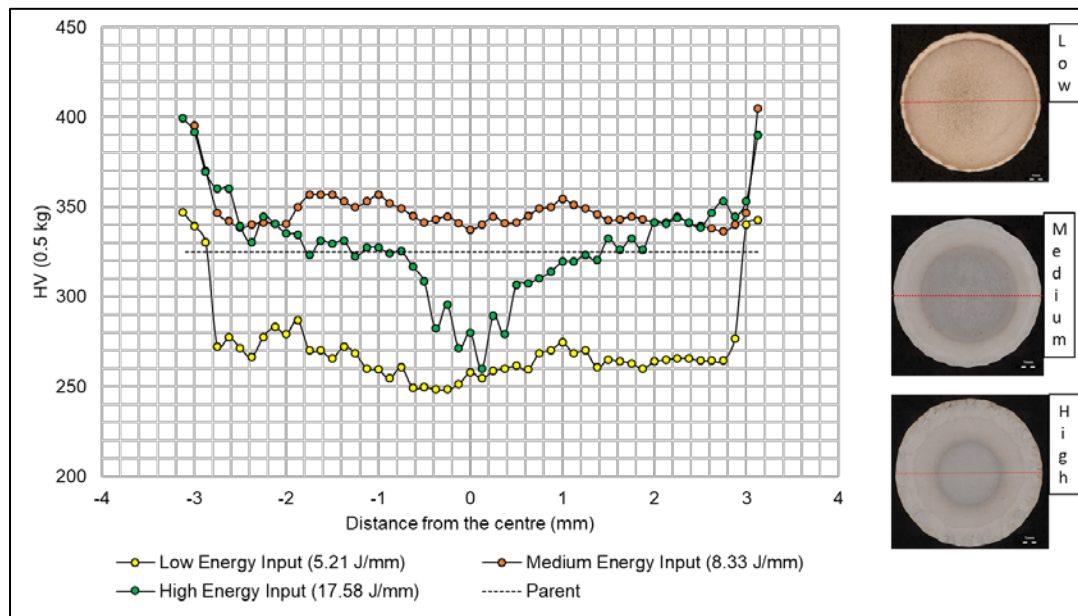


Figure 4-38: Hardness profiles across the LST specimen's centre.

The three hardness profiles of the LST processed specimen were compared to each other and to the parent material. LST processing changed the hardness profile of the three specimens by introducing a hard layer on the edge and by affecting the hardness distribution across the specimen with varying energy inputs. The hardness results plotted were symmetrical on both sides from the centre. The profiles of the specimens were similar, with high hardness values at the edge of the specimen (LST zone) and decreased values in the unprocessed zone. The high hardness in the LST zone is explained by the heating and rapid cooling, leading to microstructure transformation and refinement in this zone. It was concluded that hardness was affected by the energy input.

From the hardness distribution plots, it was observed that the low and medium energy input specimens had much more even profiles when compared to the high energy input specimen. The hardness profiles are very similar from the LST zone to the centre but with the increase in energy input in the medium energy input specimen giving rise to high hardness values. The medium energy input specimen hardness was above the parent from LST zone to the centre unlike the low one. The high energy input hardness is high on the edge, above the parent material's hardness and drops gradually across to the centre, with the centre having the lowest attained hardness. A possible reason for this observation could be that as the energy input increases, the heat affected region is larger thereby leading to different cooling rates from the edge (LST zone) to the centre of the specimen. Energy input effect between the low and medium specimen is clearly observed in the two hardness profiles. The difference in the hardness profile of the low energy input specimen as compared to the other in the region outside the LST zone still needs to be studied further.

4.5.4. Selection specimens for final analysis

Table 4-10 shows a summary of the specimens analysed under the 3 energy input conditions.

Table 4-10: Summary of the 3 selection criteria at different energy inputs.

Condition	Energy Input level		
	Low	Medium	High
Surface finish	Best surface finish	Good surface with consistent surface all around specimen	Worst surface finish, high degradation Visible oxidation
Macrograph/Visual appearance	Lowest attained LST zone depth of penetration	Uniform LST zone depth of penetration	Uneven LST zone depth of penetration at high power density.
Hardness distribution	Below that of parent	Above that of the parent, uniform across the specimen	High in LST but uneven across specimen

Taking these to be the criteria for selecting a specimen for continued analysis – namely, surface finish after LST, uniformity of the LST process on the visual images and hardness– it was decided to use medium energy specimens for continuing analysis. Medium energy input specimens displayed a better surface finish, and a homogenous or uniform LST zone when compared to both the low and high energy input specimens.

Table 4-11 displays the two medium energy input specimens selected for further evaluation. The medium input specimens selected were final matrix, LST 1 and 3, both of which had a uniform LST zone as compared to some of the low and high input specimens, which made the choice even more appealing. The two medium energy input specimens differed in power density as shown in Table 4-11. For differentiation and easy of naming, the two specimens were named low and high power density with high being power density above 1000 W/mm² and low below.

Table 4-11: Selected LST specimens for further analysis.

LST specimen	Energy Input (J/mm)	Power density (W/mm ²)	Description
1	8.33	795.8	Low-power density
3	8.33	1211.5	High-power density

4.6. Summary

The first developmental stage was used to understand the effect of laser process parameters when conducting single experimental runs on 3 mm Ti-6Al-4V sheets. It was observed that, because of the LST processing phases of heating and cooling, a LST zone with different characteristics to the parent material was introduced. This LST zone had an area of homogenous microstructure and its size (bead width and depth of penetration) was mainly affected by the input process parameters. The LST depth was influenced primarily by laser power and the position of the beam relative to the material surface. At 0 mm focus position, with the laser beam focused at the material surface, it was observed that the profile of the macrograph was uneven at the bottom. For example, at a laser power of 2000 W and focus position of 0 mm, the macrograph profile was similar to that of a laser beam weld. The bead width and depth of penetration of the LST process were seen as being critical, particularly when determining the required overlap.

The second developmental stage quantified the effect of different treatment strategies on the uniformity of the depth of penetration of the LST zone on parent fatigue specimens. It was observed that using a continuous treatment strategy led to uneven depth of penetration around the specimen from the start to the end position. This was mainly because the specimen was cold at the beginning and, as multiple LST runs were performed, the specimen became more heat saturated leading to a temperature increase.

Considering that Ti-6Al-4V has a low thermal conductivity, thereby making it difficult for it to dissipate heat quickly enough, the temperature gradient

between the start and end of the LST process was considerable as highlighted by continuous treatment specimens which had an uneven depth of penetration from start to finish. To counter this effect, a non-continuous LST strategy (2) was introduced. It was found that the LST processing of small friction welded specimens can be performed using a non-continuous laser scanning strategy. The main benefit of this treatment strategy was a uniform and homogenous microstructure, aiding in the elimination of microstructure variations observed from start to finish during the LST strategy 1 continuous treatment. There was microstructure refinement by LST which lead to a hardness increase in the LST zone.

The final matrix was developed using a 3-variable matrix with temperature being measured as a response variable. The temperature measured was not surface temperature but temperature inside or at the centre/core the specimen being processed. The measured temperature gave experimental data that was used in analysis of the analogous behaviour of the LST process. From a statistical analysis point of view, it was observed that laser power and scanning speed had the greatest effect on the temperature attained during LST processing. The relationship between laser power and scanning speed was antagonistic.

A selection criteria was identified and utilised for the selection of the best specimen for further testing from the final matrix. The final matrix specimens were quantified in terms of static performance with particular attention paid to the macro- and microstructure as well as the hardness distribution of the LST specimens. The specimens were grouped in three categories: low, medium and high energy input, as discussed.

It was observed that medium energy input specimens had a more homogenous LST zone in terms of depth of penetration all around the specimen as compared to the low and high energy input specimens. The low energy input specimens had the smallest attained LST zone depth of penetration and in some instances, a lack of uniformity and overlap between

subsequent treatment zones. The high energy input specimens had a clear uneven distribution, mainly due to the increased energy input which in turn increased the temperature gradient from start to finish of the LST processing. Defects or voids were also observed in the high energy input specimens because of uneven LST molten pool contraction during the cooling phase of the process.

Micro Vickers hardness profiles were conducted for the different energy input specimens but at the similar power density of 795.8 W/mm^2 . From the hardness profiles, it was observed that there was a general hardness increase in the LST zone especially at indentations closer to the surface. At positions 0.15 mm from the surface, the three different energy input specimens indicated higher average hardness as compared to the average hardness of 325 HV of the parent specimen. The hardness profiles of the three specimens were significantly different, which could be mainly attributed to the influence of cooling rates at different energy inputs. On the near surface of the specimen, the hardness was high but then reduced with depth. The average hardness of the low energy input specimen was below the average parent hardness of 325 HV in the regions below the surface.

The specimens selected for further analysis were determined by the quantification of surface finish after LST, uniformity of the LST process on the visual images as well as hardness. Specimens examined at medium energy input levels had the best characteristics and were selected for further analysis. The microstructural analysis of the final matrix specimens are quantified in Chapter 5.

Chapter 5. Microstructural Characterisation

5.1. Introduction

This chapter evaluates the different microstructural characteristics which develop in the LST processed - friction welded specimens selected from the final process matrix as described in Chapter 4. Microstructural analysis was conducted using Electron Backscatter Diffraction (EBSD) analysis. The main reason for using EBSD for microstructural evaluation was because the microstructure of the RFW and friction welded LST specimens could not be resolved satisfactorily by optical microscopy due to the very fine refined grains exhibited. Grain size and $\alpha + \beta$ phase distributions were determined from the EBSD analysis. A clear and concise difference between parent, RFW, and RFW + LST microstructures was seen.

5.2. Experimental Method

EBSD analysis was performed using a Scanning Electron Microscope (SEM), Jeol JSM-7001F, housed at the Nelson Mandela Metropolitan University's CHRTEM. Figure 5-1 shows the position where EBSD analysis was done on the different specimens.

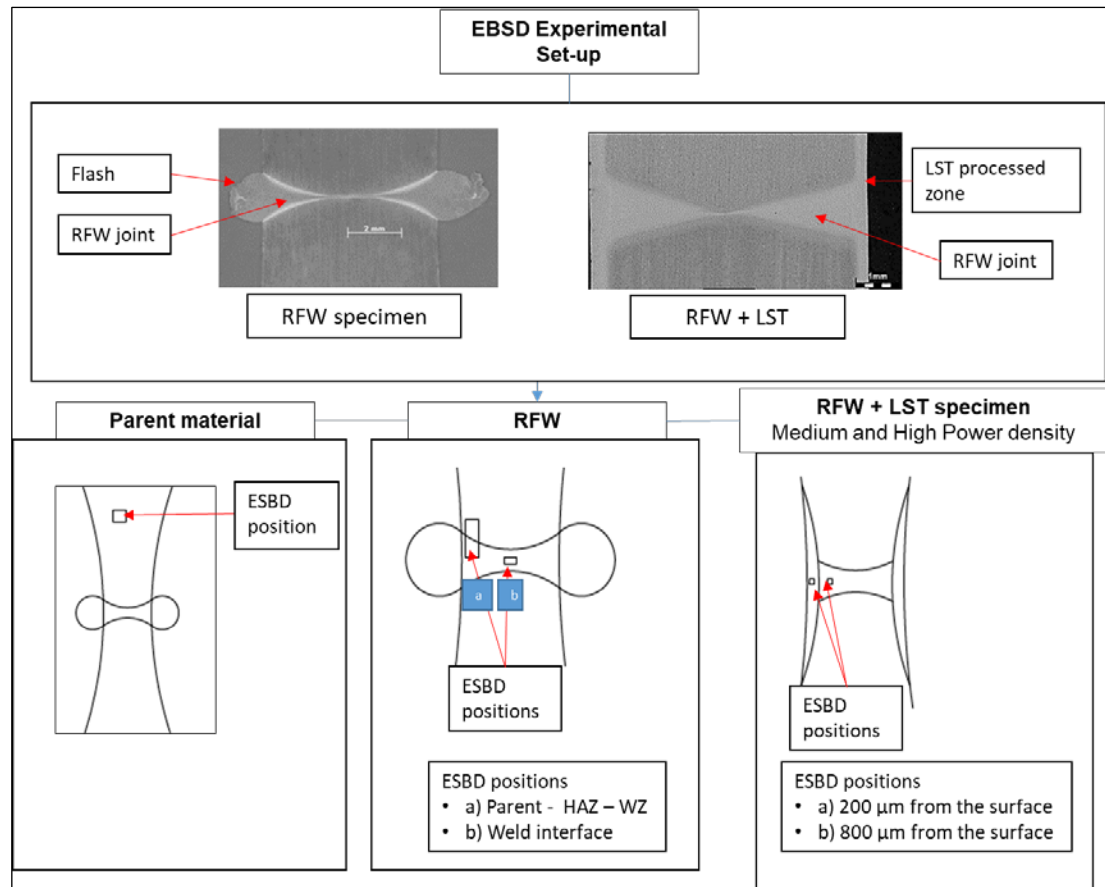


Figure 5-1: EBSD analysis position.

The following further details the experimental method used for each of the four specimens:

- The **as-received (parent) material** was characterised using EBSD by scanning an area of approximately 1.2 mm^2 at a high resolution of a step size of 0.25 μm .
- EBSD was performed on the **RFW weld zone**, a step size of 0.1 μm was used for a scanned area of 350 μm by 35 μm . The EBSD technique was able to resolve the different microstructural zones resulting from the friction welding process. Two EBSD scans were performed as shown in Figure 5-1.
- The selected specimens from the final LST matrix processed at a medium energy input were analysed using EBSD. The two specimens selected differed in power density and were categorized as low (LST 1) and high (LST 3) power density specimens. EBSD analysis was

conducted at two positions or depths from the surface, 200 μm and 800 μm . The rationale for the choice of the two positions for analysis was in order to characterise the microstructure evolution in the LST zone, 200 μm and the heat-affected region, 800 μm . Figure 5-1 displays the two positions where EBSD analysis was conducted on an LST vertical cross section. Symmetrical homogeneity and consistency was assumed for all LST specimens, which allowed EBSD measurements to be made on the same side.

5.3. Microstructure Characterisation: Results

The results of the microstructural characterisation are detailed in this section.

5.3.1. Parent material

The structure of the parent material consisted mainly of equiaxed grains with intergranular β phases. The equiaxed structure is similar to the bimodal structure with the major difference being the cooling rate during recrystallisation and also the low annealing temperature in the equiaxed structure formation [7, 59]. Figure 5-2 illustrates the EBSD band contrast image with grain boundaries.

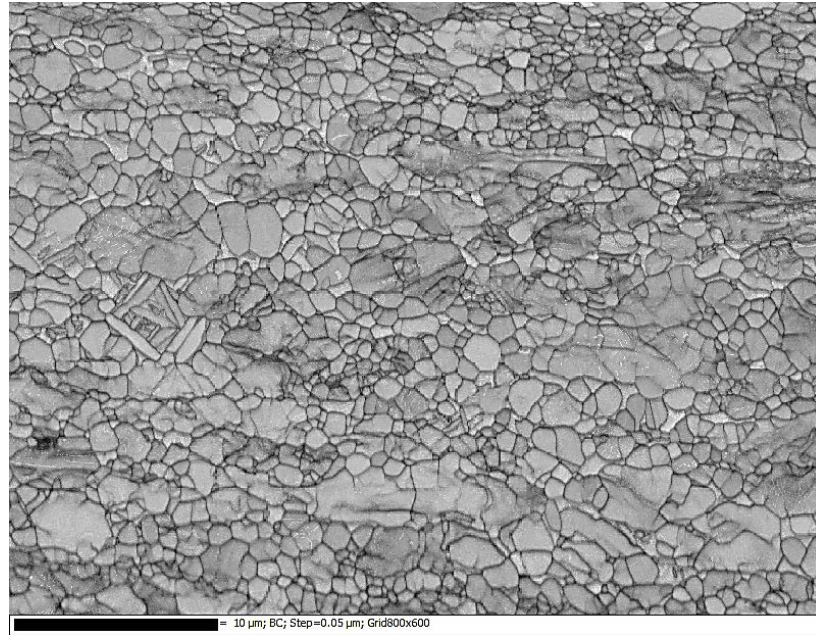


Figure 5-2: Parent material microstructure (Band Contrast with Grain Boundaries).

Figure 5-3 shows the $\alpha + \beta$ distribution of the parent material through EBSD analysis. The phase distribution was denoted as α -phase: red and the β -phase: blue. $\alpha + \beta$ distribution was quantified with approximately α 94 % to 6 % retained β which is similar to mill annealed Ti-6Al-4V ELI.

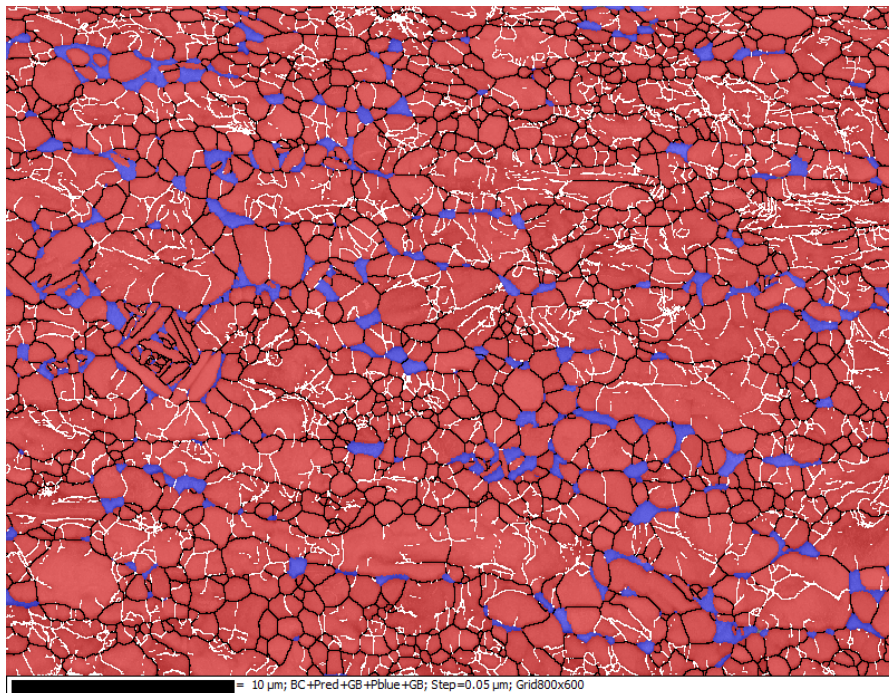


Figure 5-3: EBSD phase maps (α -red: β -blue).

5.3.2. Weld zone

Figure 5-4 and Figure 5-5 display the microstructure evolution from weld zone, to HAZ and to parent material. Figure 5-6 displays results of the EBSD analysis from the parent to the HAZ with respect to phase maps. The full EBSD results are available in Appendix D: EBSD results of the RFW specimen, illustrating the full scans.

The EBSD results showed that there was a variation in the microstructure from the parent material, through the HAZ to the weld zone. The variations in the attained microstructures were as a direct result of the friction welding process. The variation in microstructure is of major concern in the medical and aerospace industries as it is directly related to the mechanical properties of welded components. The weld zone had a very fine microstructure as displayed in the band contrast images. The weld zone microstructure and appearance were primarily governed by the cooling rate. As the first EBSD scan was close to the surface, very fast cooling rates are achieved once rotation ends.

The results showed that there was a gradual increase in the β phase composition from the HAZ to the parent material, with no β phase in the weld zone. The gradual increase in the β phase was as a result of the variation of temperatures reached within the two-zones as compared to the weld zone. The observed results were in agreement with literature, which reports that there is a lack of or no β phase in the weld zone of the friction weld when conducting EBSD analysis [59].

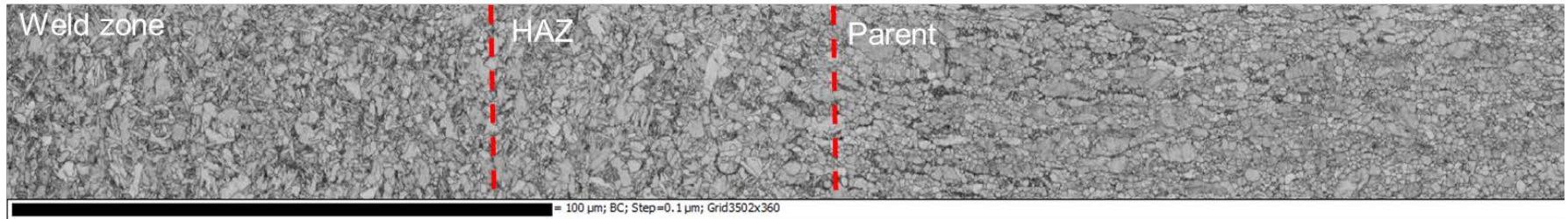


Figure 5-4: Band Contrast: weld zone, HAZ to parent microstructural evolution.

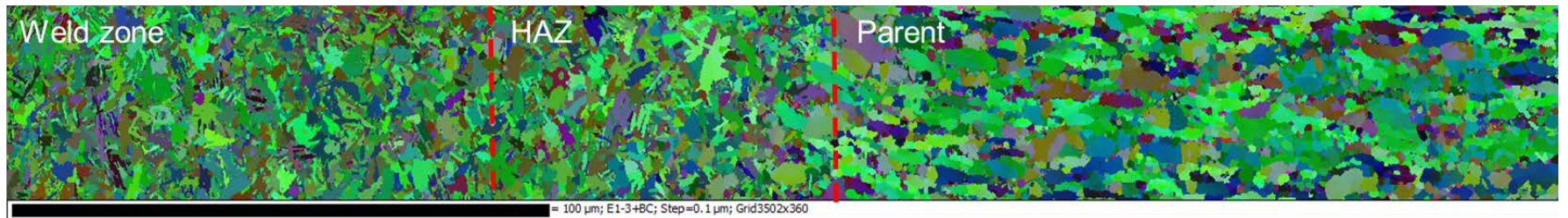


Figure 5-5: Band Contrast Euler contrast: weld zone, HAZ to parent microstructural evolution.

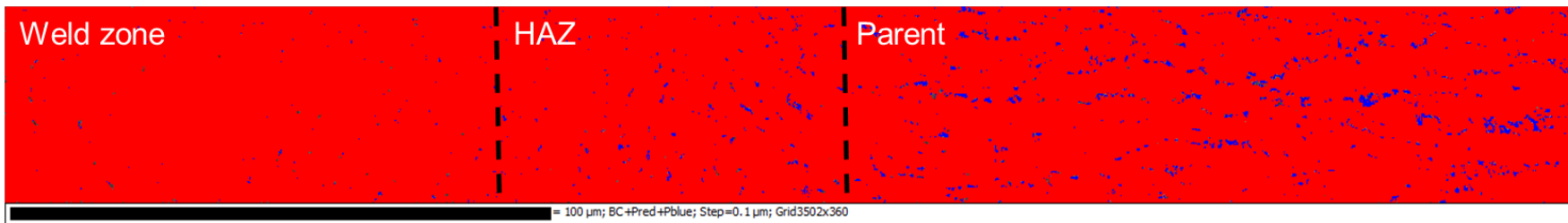


Figure 5-6: Phase map: weld zone, HAZ to parent microstructural evolution.

The second EBSD scan highlighted the centre of the weld. The attained microstructure is illustrated in Figure 5-7, with red colour lines indicating the sub grains. In this zone, a bimodal microstructure was observed which was mainly influenced by cooling rate from the beta transus. The bimodal structure requires homogenisation to occur above the β transus temperature with the rest of the stages occurring below the β transus temperature (deformation, recrystallisation and aging respectively). The rotary friction weld centre is the thinnest section; this leads to a quick dissipation of heat to the cold parent material as soon as the RFW process is completed or when the rotation stage is complete.

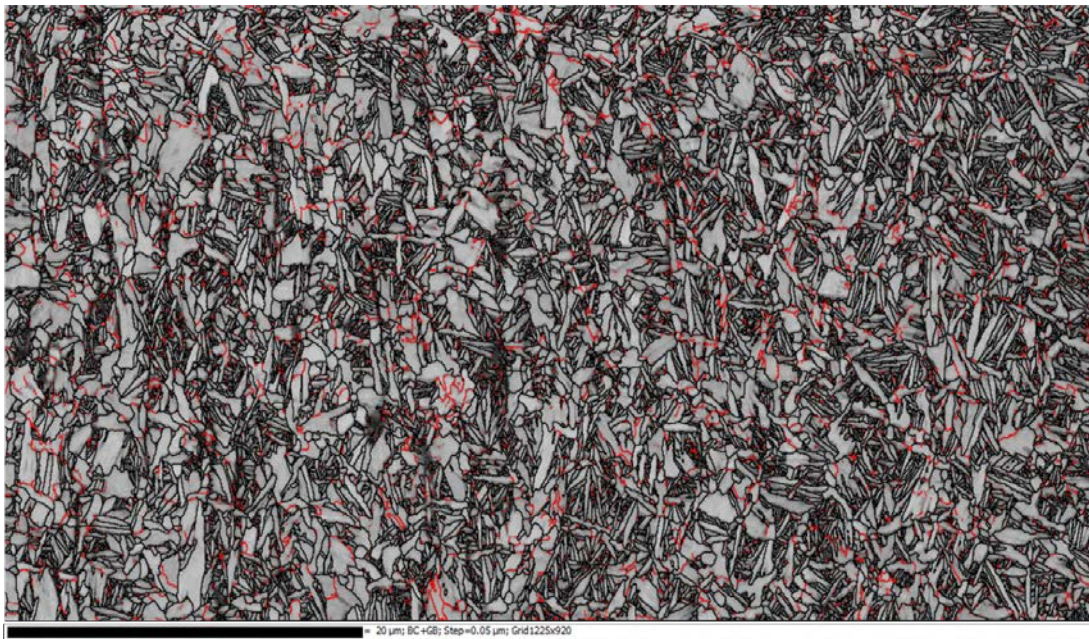


Figure 5-7: RFW weld interface microstructure band contrast + sub grains (red).

At the centre of the RFW weld, there was no evidence of retained β as shown in the Figure 5-8 phase map. Therefore, at this position, the maximum temperature was above the β transus temperature which led to all the β being transformed to α .

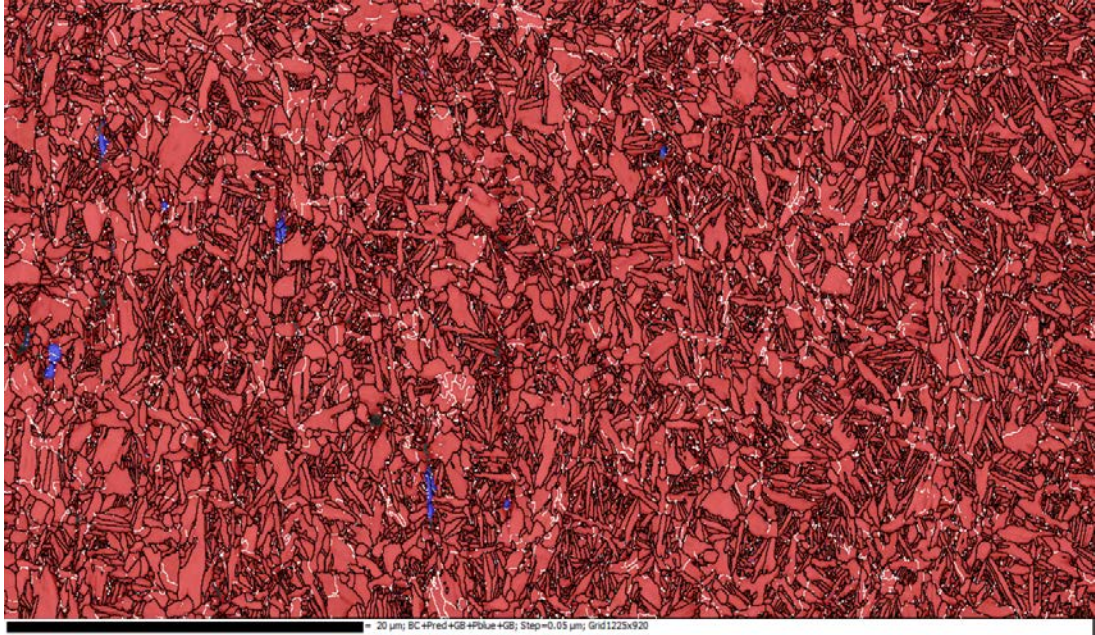


Figure 5-8: Phase maps at position two (α -red and β -blue).

5.3.3. RFW - LST specimens

The microstructural characterisation results from the two positions (200 and 800 μm) selected are detailed in this section. Each half of the specimen was deemed to be symmetrical. Figure 5-9 illustrates the attained microstructures for both low and high-power density specimens at the 200 μm . The microstructure observed in the LST zone position a) was a fine acicular α lamella (needle-like α) basket weave structure. This microstructure was formed as a result of cooling occurring from above the β -transus region. From the images of both specimens, colonies were identifiable as lamella needle-like structures lying in the same orientation.

Note: All Euler plots in EBSD display non-equivalent orientations in the microstructure with different colours and in Figure 5-9, these images best show colonies with lamella needle-like structures lying in the same orientation.

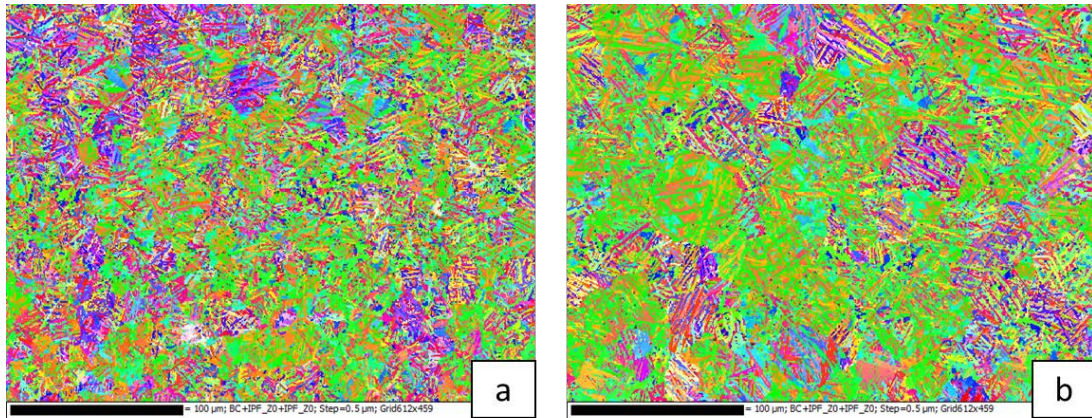


Figure 5-9: All Euler plots of LST specimens at position 1, 200 μm showing the difference in the colonies and lamella size a) low b) high.

A further EBSD analysis study was conducted at a depth of 800 μm . At this depth, it was observed that there was a microstructure variation with depth (200 μm to 800 μm). Closer to the surface at the 200 μm depth, the microstructure observed was fully lamella for both specimens but at the 800 μm position, a mixture of equiaxed grains and lamella structures was visible. A full lamella structure was evident at the 200 μm instead of the 800 μm because of the proximity to the surface at 200 μm which led to a fast cooling rate or quenching effect. Figure 5-10 shows an example of the microstructure evolution of the specimen from the 200 μm to 800 μm position for the low-power density specimen.

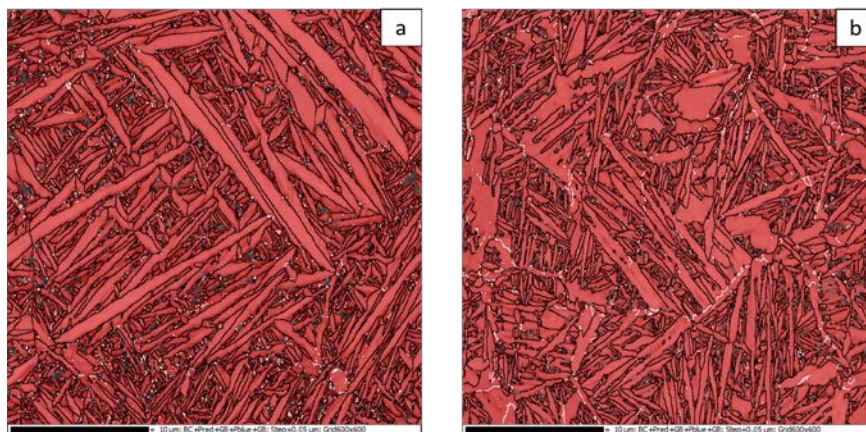


Figure 5-10: Microstructure evolution of low-power density specimen a). 200 μm b). 800 μm positions.

To further analyse the LST specimens, it was decided to measure the lamella width. As was discussed in the literature review, lamella width and length dictate the fatigue performance of Ti-6Al-4V ELI specimens. The smaller and thinner the width and length of the lamella structure, the better the fatigue performance. Determining the lamella length was difficult because this would require performing a large EBSD scan at high resolution which would increase the scanning time three fold. The current scanning time for the large scan was 18 hours. Therefore, small scans were done to determine the lamella width.

Comparing the two LST specimens, of low and high-power density, there was a clear microstructural difference at a depth of 800 μm . The high-power density specimen had a coarse structure in comparison to the low-power density specimen. The respective power densities affected the observed microstructure as different cooling rates were present.

The low and high-power density specimens had an average lamella width sizes of 0.93 μm and 1.88 μm respectively. The lamella width of the high-power density specimen was double that of the low-power density specimen, which could therefore be attributed to the increase in power density. Although there is recognisable difference in the lamella width, both sizes are classified to be very fine microstructures which relate to very fast cooling rates from temperatures above the β transus. Phase maps of all the positions measured indicated that the LST zone had no β phase present. The fine microstructures could only be resolved by EBSD, which further explains the extent of the degree of the size of the microstructure. Figure 5-11 illustrates the attained microstructures for both specimens, low and high power density. Appendix E illustrates the EBSD phase maps of LST specimen.

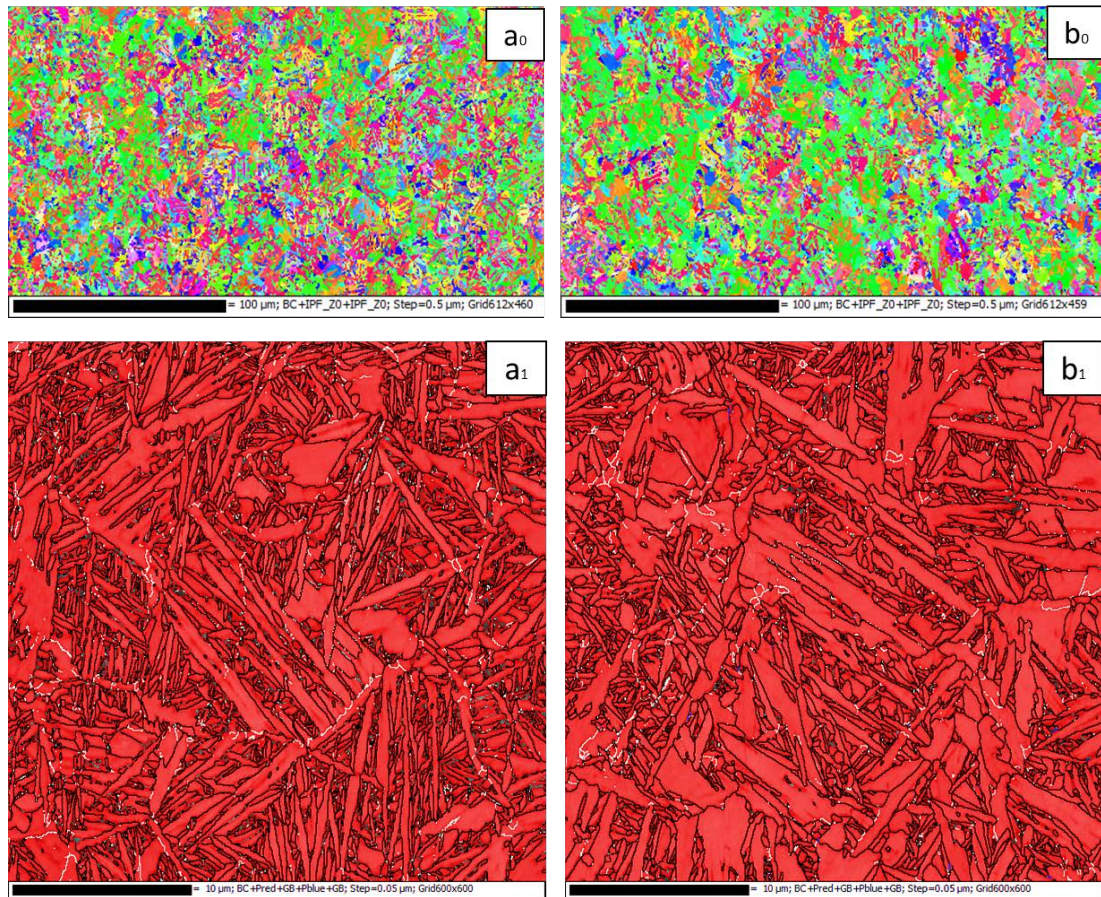


Figure 5-11: Microstructure at 800 μm for a) low (a_0 – enlarged area IPF plot and a_1 – small zoomed in area) and b) high (a_0 – enlarged area IPF plot and a_1 – small zoomed in area).

5.4. Hardness Distribution in the Laser Surface Distributed Zone

After completion of the EBSD microstructural characterisation, a hardness analysis was performed on the near surface (at approximately 0.2 mm from the surface) of the friction welded, LST low and high-power density specimens. This was done to further analyse what effect the microstructural changes had on the hardness in the three samples. The hardness measurements were done in the direction parallel to the surface as shown in Figure 5-12 using a 0.5 kg load. Figure 5-13 shows the different hardness profiles of a friction weld and LST processed specimens as compared to the parent material.

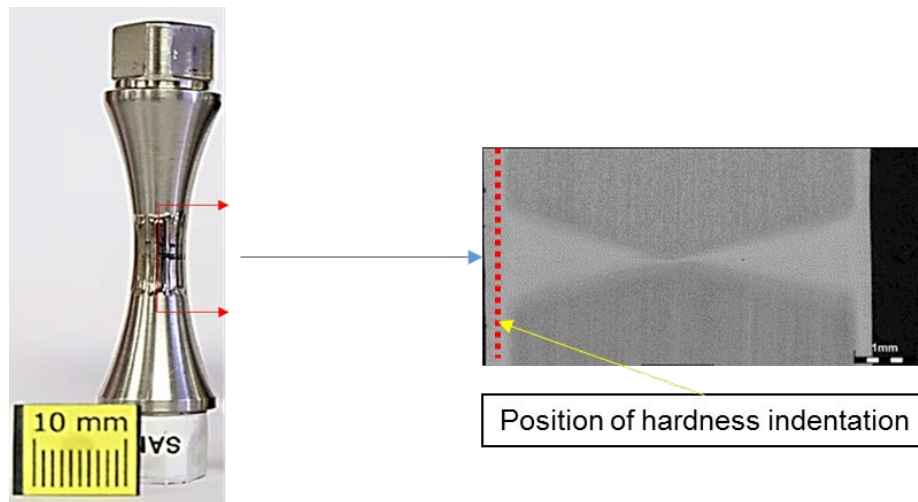


Figure 5-12: Position of hardness indentation.

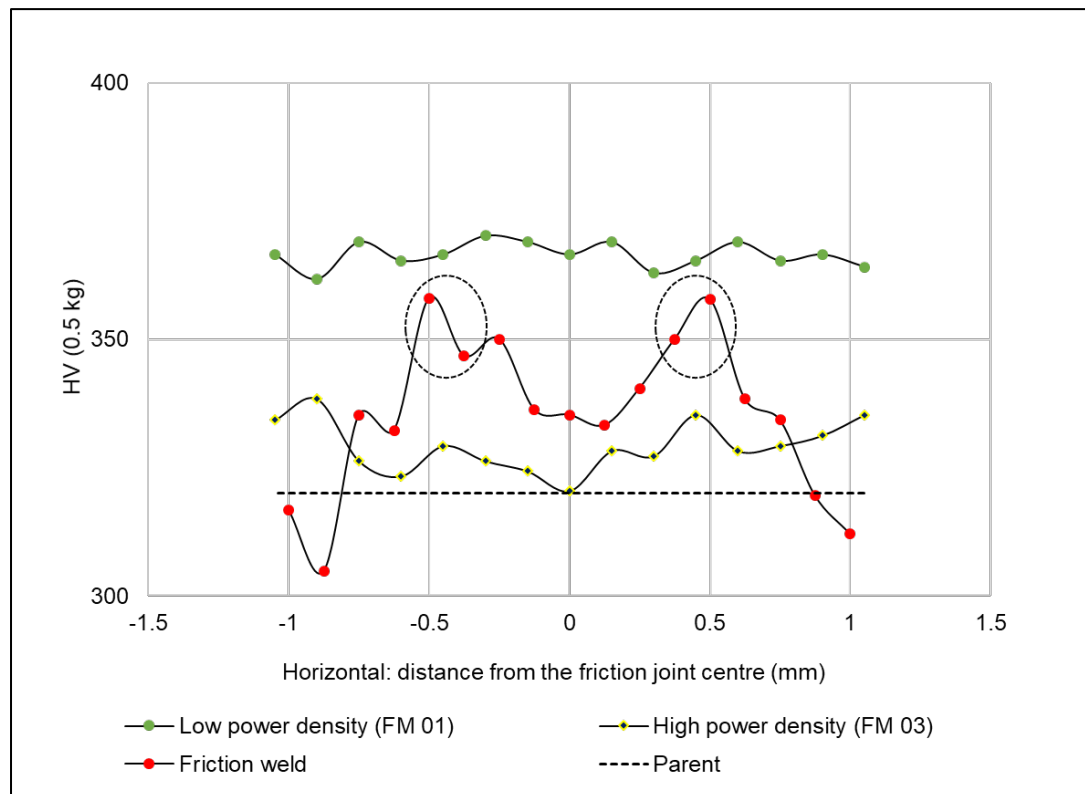


Figure 5-13: Hardness analysis for the three specimens. (Two circles highlighting position of the HAZ)

Although the HAZ is very narrow, hardness peaks were observed in this region similar to van der Merwe's [5] observations. The hardness peaks in the HAZ and decreases close to the weld centre. This increase in hardness in the HAZ

is due to the microstructure change in this zone as shown in Figure 5-7. The weld zone has hardness values close to that of the parent material. As noted earlier, the microstructures on the outside of the weld are all refined equiaxed structures but the hardness values differ. This hardness differential is not desirable in fatigue testing; if the gradient is too steep the joints will inherently have a poor fatigue life as a result of the adverse grain boundaries providing loci for crack initiation and propagation in the HAZ region [5].

LST processing introduced a decrease in hardness variation from the start to the end of the treated specimens when compared to just a friction weld. Between the two LST specimens, the low-power density specimen had a higher hardness average when compared to the high-power density specimen. Therefore, the results were consistent with observed microstructure where the low-power density specimen had very fine microstructure in comparison to the high-power density specimen, and the friction weld only showed variation of microstructure from the parent material, through the HAZ and to weld zone.

5.5. Summary

The EBSD results displayed the effect of power density on the observed microstructure within the LST zone. A fully α -lamella microstructure was observed in the two specimens analysed at a position of 200 μm from the surface. The α -lamella had different width sizes with the low-power density specimen having a very fine microstructure in comparison to that of the high-power density specimen. Phase distribution showed that there were no traces of β in the LST zone, thereby indicating that the microstructure obtained was a result of cooling above the β -transus temperature. The two power densities gave rise to different cooling rates which affected the final observed microstructure. It can be concluded that the cooling rate directly influences the final observed microstructure and relative hardness distribution.

Two specimens were analysed at different power densities. To analyse the effect of power densities, a Micro Vickers hardness measurement was

conducted across the vertical direction in the LST zone. This hardness evaluation was systematically different from that detailed above in that it quantified the vertical cross-section as depicted in this chapter. There was a hardness difference in the LST between the specimens, with the high-power density (1211.5 W/mm^2) exhibiting a low average hardness as compared to the low-power density specimen (795.8 W/mm^2).

Chapter 6. Residual Stresses and Fatigue Properties of Laser Surface Treated Specimens

6.1. Introduction

This chapter quantifies the influence of laser surface treatment on residual stresses and fatigue properties of LST specimens selected from the final matrix as compared to the parent material and RFW specimens. Through-depth residual stresses were measured using a synchrotron X-ray diffraction technique. The LST processed specimens were subjected to dynamic loading by performing rotary bending fatigue tests at a stress ratio of $R = -1$. Fatigue tests were conducted on specimens in the polished condition. A polished surface condition aided the elimination of surface defects which is known to negatively affect the fatigue behaviour of Ti-6Al-4V components.

6.2. Residual Stress Analysis

The technique of synchrotron X-ray diffraction has been in existence since the 1960s and has greatly benefited the engineering community. The main advantage of synchrotron X-ray diffraction is its ability to acquire data in the order of seconds or even milliseconds because of the high intensities and the high collimation rates of the beam. In engineering, synchrotron X-ray diffraction has been used to quantify the residual stresses within welded components and plastically deformed structures to mention a few. The main principle of synchrotron X-ray diffraction is the determination of strain from measured lattice spacing with reference to the strain-free lattice spacing. The term synchrotron is defined as *'a type of cyclotron consisting of magnetic sections alternately spaced with sections in which particles are electrostatically accelerated while diffraction refers to the spreading wave pattern from a finite-width aperture.'*

As stated in the introduction, to better quantify the effect of residual stresses, through-depth, residual stresses were measured using synchrotron X-ray diffraction. The synchrotron X-ray diffraction residual stress experiments were performed at the European Synchrotron Radiation Facility (ESRF) in Grenoble, France, experimental number ESRF ME1440. ESRF has a third-generation synchrotron source which is able to overcome the limitations posed by X-ray techniques [75]. The third-generation sources provide high X-ray energies with no absorption edges while the attenuation length increases as a result of high energies. A method commonly used in synchrotron X-ray analysis is energy-dispersive synchrotron X-ray diffraction (EDXRD). EDXRD is a versatile and powerful tool because of its ability to provide full X-ray spectra at a single diffraction angle [76]. In strain field depth profiling, EDXRD is the technique of choice because of the high-count rates achievable from small diffraction volumes and the simultaneous multi-line diffraction spectra attainable. In this study, EDXRD measurements assisted in the understanding of the overall nature of the induced residual stresses. Four specimens were tested, the parameters of which are explained in the section to follow.

6.2.1. Experimental method and set-up

For this experimental study, the number of specimens was kept relatively small. The matrix included an as welded specimen, an as machined half specimen and two LST specimens. For the LST processed specimens, only power density differed whilst energy input was kept constant. The friction welded specimen was prepared by machining away the flash and then polishing the specimen to remove any surface scratches. The diameter for all the specimens was 6 mm.

Table 6-1 displays the specimens selected for synchrotron X-ray diffraction analysis and the two LST specimens were labeled as either high or low-power density specimens.

Table 6-1: Specimens analysed by synchrotron X-ray diffraction.

Specimen number	Energy input (J/mm)	Power density, (W/mm ²)	Depth of penetration of LSE layer (mm)	Description
0		-	-	As welded specimen
1	8.33	859.4	0.45	Low-power density
2	8.37	1211.5	0.46	High-power density
3		-	--	As machined half specimen

Figure 6-1 shows the arrangement of the specimens before synchrotron X-ray diffraction commenced.



Figure 6-1: Specimens to be analysed by synchrotron X-ray diffraction.

The residual strains were measured from the surface to the centre of the specimen with the residual strain measurements done on a single sample for all the different parametric samples. The technique utilised was white beam energy-dispersive synchrotron X-ray diffraction (EDXRD) on the ID15A beamline. The ESRF ID15A is used specifically for applications of high energy X-ray radiation to

materials in the fields of chemistry and engineering. The beamline has a wiggler source which enables it to provide a continuous spectrum up to 250 Kev coupled with high flux thereby achieving penetration depths of several centimetres. The detector was a liquid-nitrogen-cooled germanium single crystal detector attached to a multi-channel analyser. The experimental set-up utilised was described in great detail by Steuwer et al [77]. Figure 6-2 illustrates a basic schematic of beamline ID15A at the ESRF and Figure 6-3 shows the specimens mounted on the specimen holder in the synchrotron X-ray diffraction chamber before commencement of the residual stress analysis.

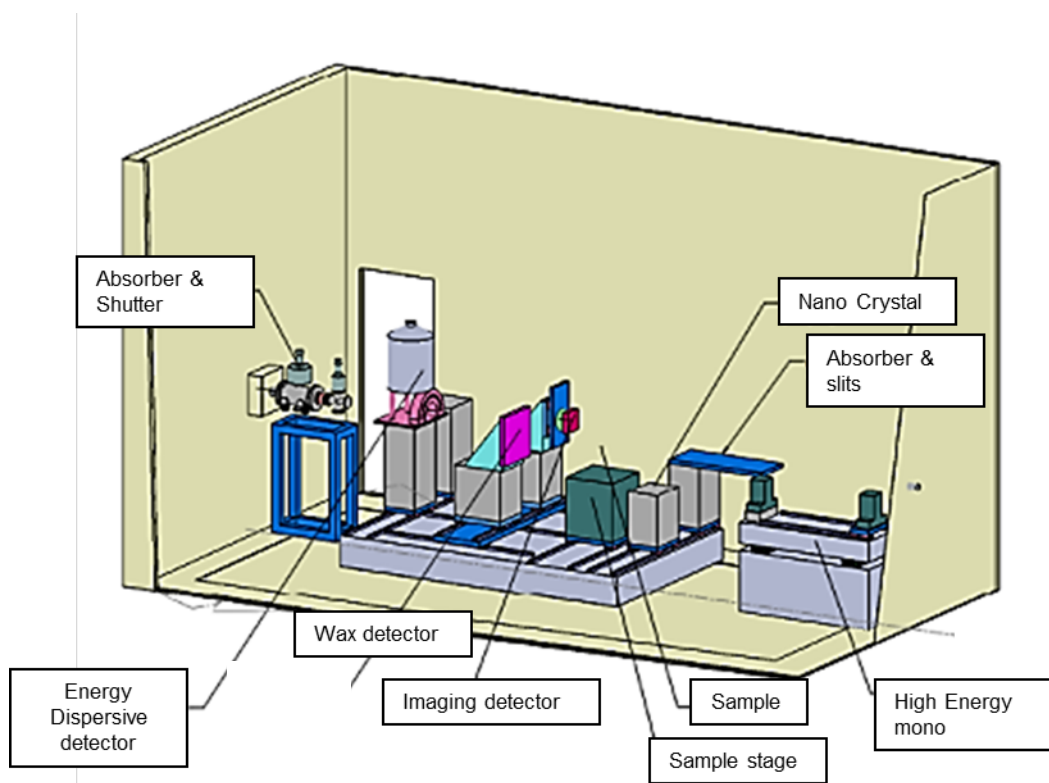


Figure 6-2: Illustration of the ID15A beam at the ESRF [77].

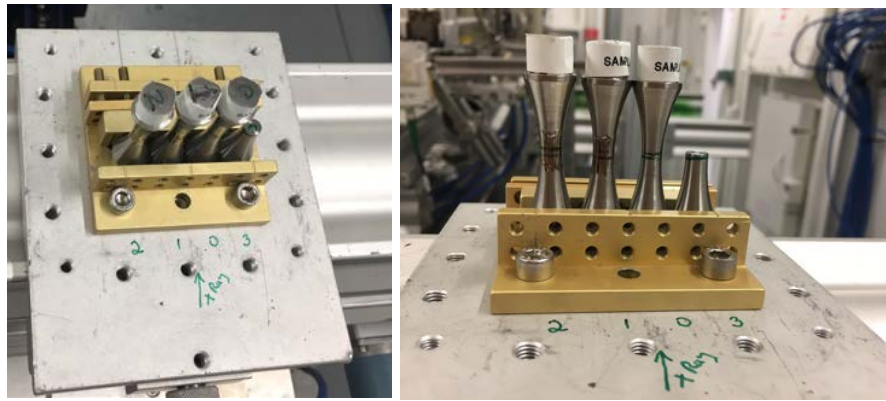


Figure 6-3: Depiction of the synchrotron X-ray diffraction specimens mounted on the specimen holder before testing commenced.

The schematic in Figure 6-4 indicates where the measurements were taken on the specimen from the near surface to a depth of 3 mm into the specimen. The measurements were performed at 0.2 mm intervals from the surface. The two halves of the specimens were assumed to be symmetrical and thus measurements were carried out until the centre of the specimen was reached.

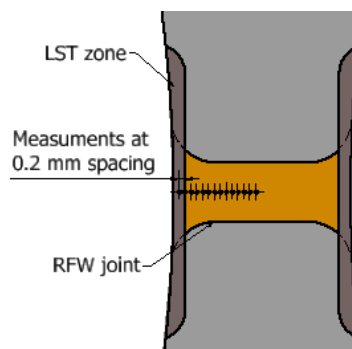


Figure 6-4: Schematic illustrating residual strain measurement positions.

Apart from the LST processing conducted on the specimen, no other post processing heat treatment was performed. The parent material was used in its original as-received state, after which it was machined to the desired shape. Residual stress results. For material properties refer to section 3.2. Olson and Bert [56] provide a detailed analysis for calculating residual stresses in bars and tube using the coring method. For the calculations to be valid they assumed the following:

- The process of boring induced deformation but for the purposes of their calculation they assumed the process to be linear, therefore, Hooke's law applied:

$$\sigma = \varepsilon E \quad (6)$$

- The material is uniform in all three perpendicular planes of symmetry.
- Stress distribution is symmetrical about the axis of the specimen and constant along its length.

Therefore, based on their work, the hoop stress is calculated as follows:

$$\begin{aligned} \varepsilon_a &= \frac{\sigma_a}{E} - (\sigma_\theta + \sigma_v) \frac{\nu}{E} \\ \varepsilon_\theta &= \frac{\sigma_\theta}{E} - (\sigma_a + \sigma_v) \frac{\nu}{E} \\ \varepsilon_r &= \frac{\sigma_r}{E} - (\sigma_a + \sigma_\theta) \frac{\nu}{E} \end{aligned} \quad (7)$$

At the surface: $\sigma_r = 0$

$\sigma_r = 0$, therefore the above equations becomes :

$$\varepsilon_a = \frac{\sigma_a}{E} - \frac{\nu}{E} (\sigma_\theta) \quad (a)$$

$$\varepsilon_r = -\frac{\nu}{E} (\sigma_a + \sigma_\theta) \quad (b)$$

$$\varepsilon_\theta = \frac{\sigma_\theta}{E} - \frac{\nu}{E} (\sigma_a) \quad (c)$$

Then multiply equation (a) by negative Poisson's ratio of the material ($-\nu$)

$$-\nu \varepsilon_a = -\frac{\nu \sigma_a}{E} + \frac{\nu^2 \sigma_\theta}{E} \quad (d)$$

Making $-\frac{\nu \sigma_a}{E}$ the subject of the formula in equation (d)

$$\frac{\nu \sigma_a}{E} = \frac{\nu^2 \sigma_\theta}{E} + \nu \varepsilon_a \quad (e)$$

Substituting equation (a) to equation (b), then equation (b) becomes:

$$\varepsilon_r = -\frac{\nu \sigma_\theta}{E} - \left(\frac{\nu^2 \sigma_\theta}{E} + \nu \varepsilon_a \right) \quad (f)$$

$$\varepsilon_r + \nu \varepsilon_a = -\sigma_\theta \left(\frac{\nu^2 - \nu}{E} \right) \quad (g)$$

Making σ_θ the subject of the formula in equation (c)

$$\sigma_\theta = -\frac{E}{\nu(\nu+1)} (\varepsilon_r + \nu \varepsilon_a) \quad (8)$$

6.2.2. Residual stress results

The error estimation, $\Delta \sigma$ on the residual stress data was less than 10 MPa, therefore is too small to see. Analysis of the residual stress results at the surface, sub-surface and centre showed the following:

Axial stress analysis

Figure 6-5, illustrates the axial residual stress results. The nature of residual stresses in the LST specimen changed from tensile to compressive from the near surface to the centre of the specimen. The as machined half specimen was the only specimen which had a compressive residual stress at a position near the surface of 0.2 mm.

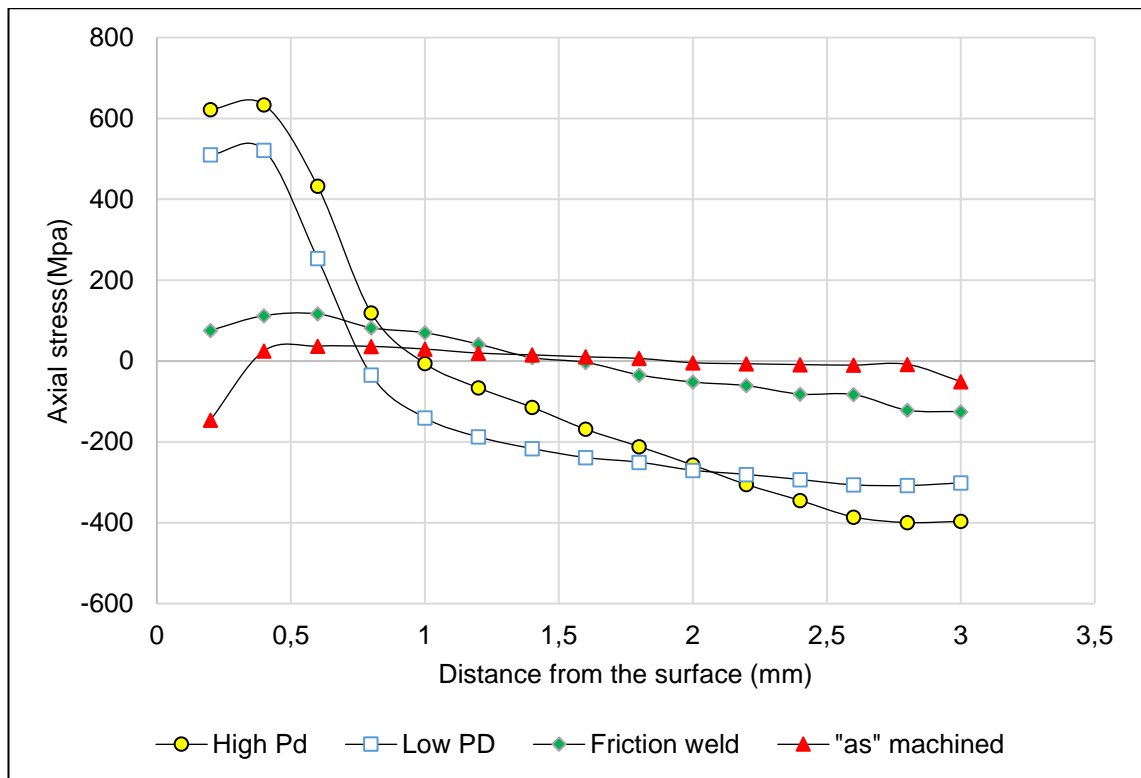


Figure 6-5: Residual stress profile: Axial.

The axial results at the four positions in the axial direction are illustrated in Table 6-2. Figure 6-6 shows a graphical presentation of the results.

Table 6-2: A summary of the axial residual stresses results.

	High Pd (MPa)	Low Pd (MPa)	Friction Welded (MPa)	As machined (MPa)
Surface	622.2	510.1	75.9	-145.8
Sub surface 0.8 mm	119.1	-34.6	82.3	36.3
Sub surface 1.6 mm	-168.6	-238.6	-3.4	10.4
Centre	-396.5	-301.4	-125.1	-50.8

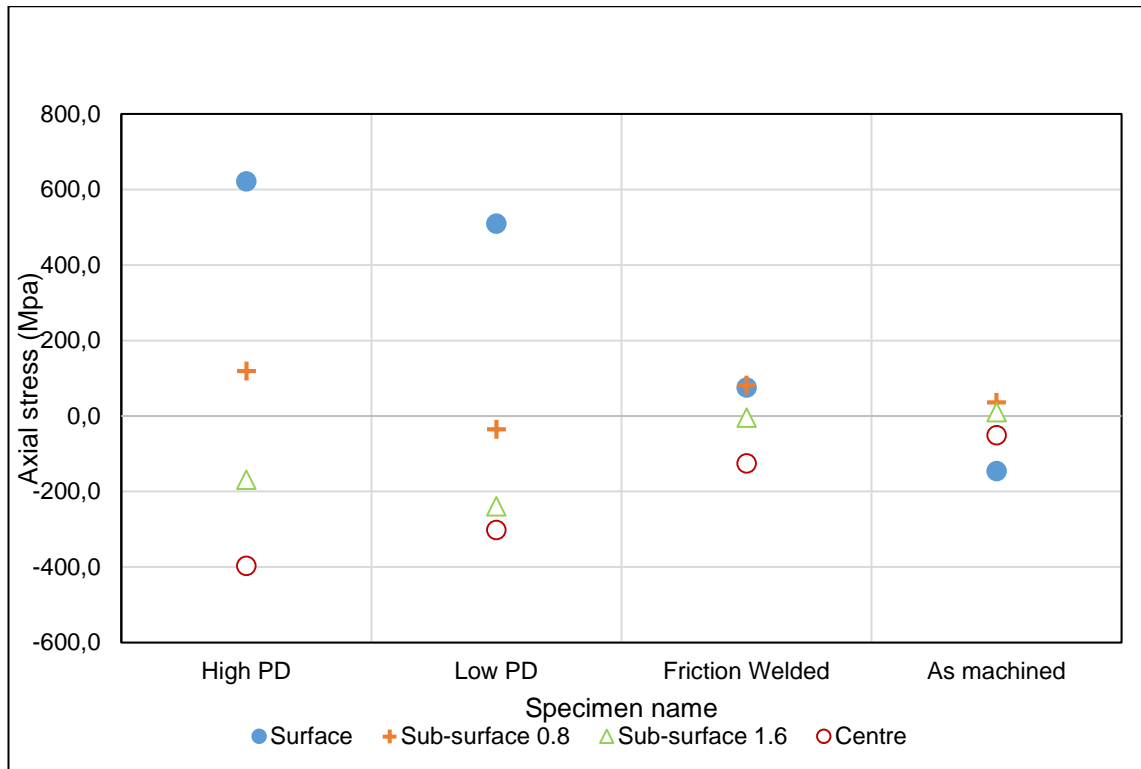


Figure 6-6: Axial residual stress analysis.

From the axial result analysis, an indication of the manner in which the residual stresses were modified at the different positions was established and is detailed as follows:

- Surface (0.2 mm)

The axial stress results indicated that the high-power density specimen had the highest tensile residual stress at the surface, whilst the as machined specimen had a compressive residual stress at the surface of -145.9 MPa. The results show a decrease in residual stresses of 120 MPa at the near surface position of the high and low-power density LST specimens. This decrease in residual stress near the surface was attributed to the microstructural change in the two specimens as a result of LST power density variation. The as friction welded specimen had a tensile stress of 75 MPa. This low tensile residual stress could be explained by the fact that the specimen was in a polished condition. Van der Merwe [5], found that polishing the specimen reduced the tensile residual stress at the surface. The near surface residual stress results of

the LST specimens generally correlated with those reported in the literature.

- Sub-surface (0.8 mm and 1.6 mm)

At the 0.8 mm sub-surface, the LST specimens showed a decrease in the axial residual stress while the as machined specimen had a tensile residual stress of 36.3 MPa. The low-power density specimen showed a clear change from tensile 510.1 MPa to compressive 34.6 MPa between the surface and sub-surface respectively. There was a marginal change in residual stresses of the friction welded specimen from surface to 0.8 mm sub-surface. At 1.6 mm sub-surface, the LST specimens both showed an increase in the compressive residual stress. The low-power density specimen had the highest attained residual stress, followed by the high-power density specimen, the friction welded specimen and lastly the as machined specimen.

- Centre

At the centre, all the specimens naturally had a compressive stress. The high-power density specimen had the highest compressive stress as compared to the other specimens. From the near surface to the centre, LST specimens showed a clear change from tensile to compressive stress.

Radial stress analysis

Figure 6-7 illustrates the results of the radial residual stress. The results of the radial residual stress did not follow a similar trend to the axial stress results.

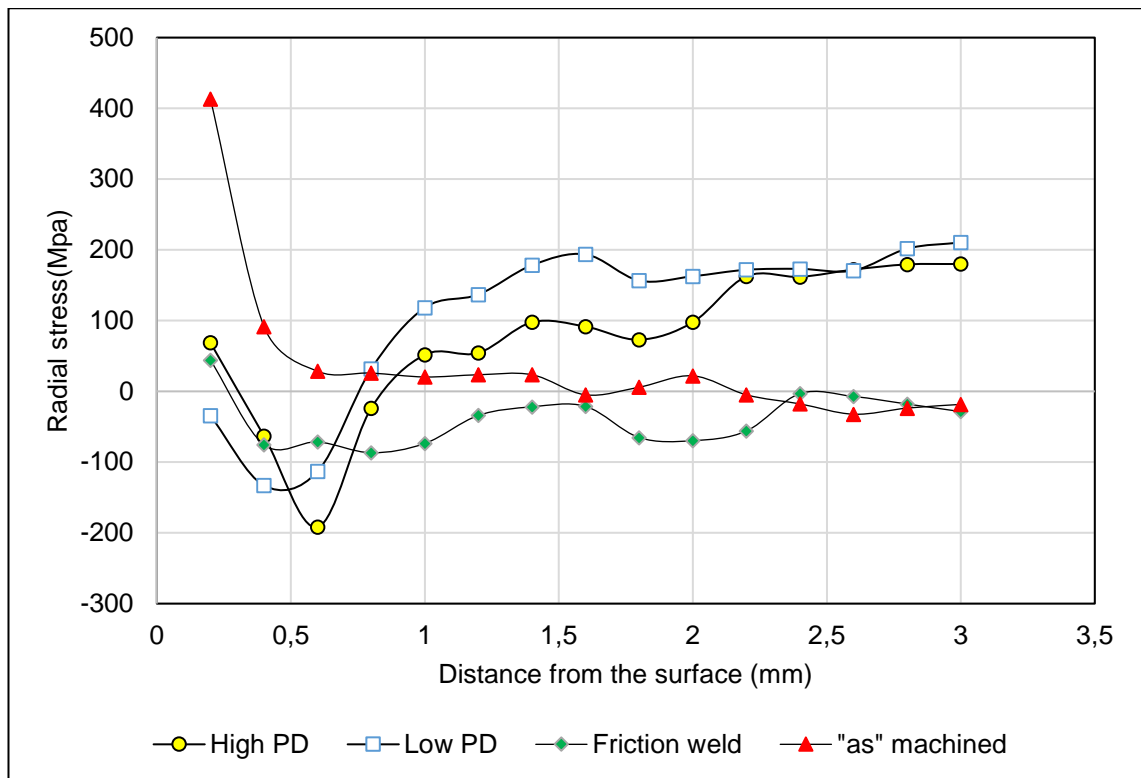


Figure 6-7: Residual stress profile: Radial stress.

The radial results at the four positions in the axial direction are illustrated in Table 6-3. Figure 6-8 shows a graphical presentation of the results.

Table 6-3: A summary of the radial residual stress results.

	High Pd (MPa)	Low Pd (MPa)	Friction Welded (MPa)	As machined (MPa)
Surface	68.8	-34.4	44.1	413.4
Sub surface 0.8 mm	-23.7	31.6	-86.7	25.9
Sub surface 1.6 mm	91.5	193.6	-21.3	-4.9
Centre	179.4	210.4	-28.6	-18.4

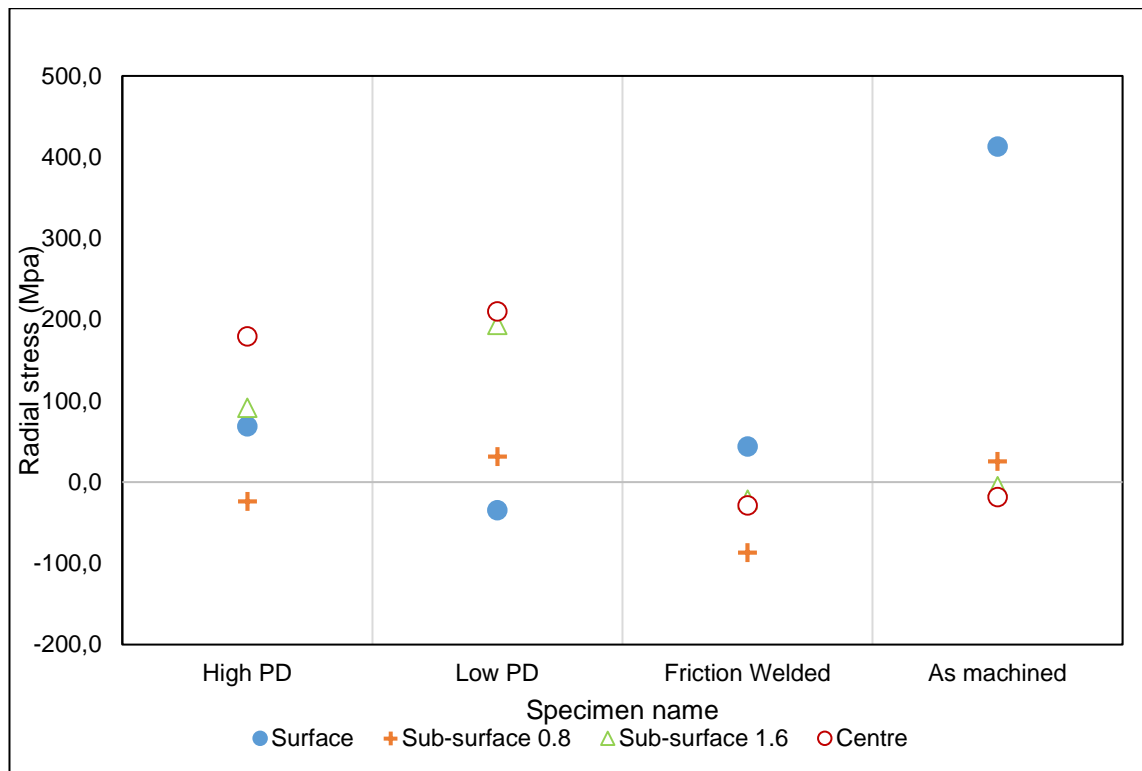


Figure 6-8: Radial residual stress analysis.

The radial residual stress was modified as follows:

- Surface

The maximum tensile residual stress was recorded for the as machined half specimen while the LST processed specimens had similar residual stress profiles, with the high and low-power density specimens having maximum residual stress of tensile 68 MPa and compressive 34 MPa respectively.

- Sub-surface (0.8 mm and 1.6 mm)

In this region, all the specimens exhibited similar residual stress values with the friction welded specimen having the lowest radial stress of -86.7 MPa.

- Centre

The friction-welded specimen showed a constant residual stress profile from the surface to the centre of the specimen. The friction-welded specimen also had the highest compressive residual stress when compared to all the other specimens. The LST specimens both had tensile stress with the low-power density specimen having the highest stress of 201.4 MPa at the centre.

Hoop stress analysis

Figure 6-9 illustrates the calculated hoop stress of the specimens close to the surface only. It was found that close to the surface, the stresses were close to zero for the LST processed and RFW specimens. All the specimens displayed a similar profile or trend with high tensile residual stresses from depths of 0.4 mm, except for the as machined half stud. The as machined half stud had a compressive residual stress from the surface up to the 0.8 mm depth.

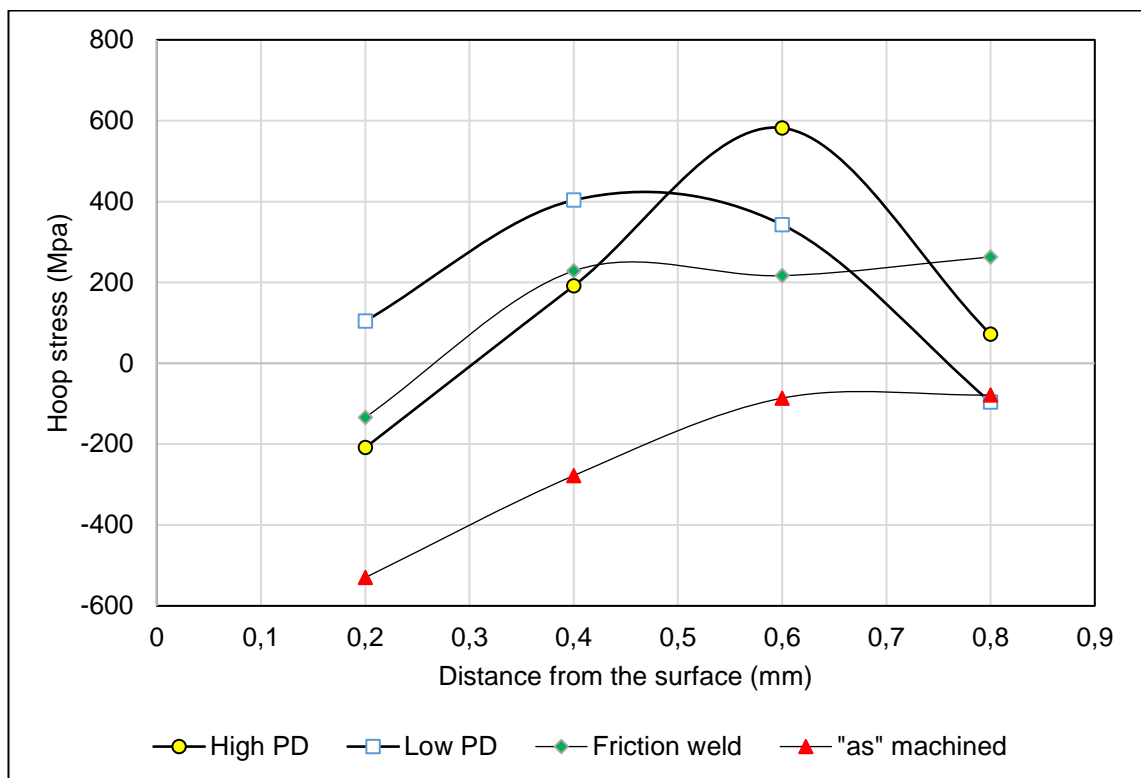


Figure 6-9: Residual stress analysis: Hoop stress close to the surface only.

6.2.3. Summary

In conclusion, the as machined half stud had the highest attained tensile radial residual stress of 413 MPa compared to that of the LST specimens, but the lowest values for axial and hoop stress. Normalisation of the residual stresses was not conducted before LST and RFW processing. The RFW specimen residual stress profile was measured in the weld zone. Normally, notch sensitivity is more pronounced in the HAZ of the welded specimen. Residual stresses arise from plastic misfits introduced by steep thermal welding gradients. In LST processing, the thermal gradients are very steep, resulting in high tensile stresses in the longitudinal direction. Mashinini [30] observed that residual stress peaks were in the HAZ zone of the FSW and LBW. In the longitudinal direction, the attained residual stress values were above 350 MPa and varied greatly with increasing heat input.

The residual stresses properties of the LST processed specimens were quantified and compared to the RFW and parent specimens. Through-depth residual stress analysis was conducted by synchrotron X-ray diffraction. The two synchrotron X-ray diffraction detectors measured residual stresses in the axial and radial direction with hoop stress calculated as shown in this chapter.

The parent specimen had the highest compressive residual stress compared to the other three specimens in the axial direction while the LST processed specimens had the highest tensile stress. This effect was attributed to both the welding and the LST processing. The specimens analysed in this work did not have any stress relieving process performed on them. For both LST processed specimens, the axial residual stresses were highly tensile at the 0.2 mm position as compared to the RFW and parent specimen (both in the polished condition).

At a depth of 0.8 mm from the surface, the residual stresses were compressive in the LST low-power density specimen processed, in comparison to the other specimens. The radial residual stresses were low for all the specimens tested but the low-power density specimen had the lowest radial stress of compressive 34 MPa.

6.3. Fatigue Life Characterisation

To quantify the influence of LST as a post weld processing step on the dynamic properties of Ti-6Al-4V ELI components, fatigue testing was conducted at a stress ratio of $R = -1$ on a rotary bending fatigue platform. The method utilised for fatigue testing was a Step-Loading (Pearl Chain) Technique, which has been successfully implemented by James et al. [28]. This technique makes use of testing a large number of specimens at different stress levels. The principle behind the technique is that the specimen is fatigue tested from the upper limit and as the specimen breaks, the stress is lowered until the endurance limit or run-out is reached. The minimum fatigue strength was initially set at 30% of UTS of the parent material (300 MPa) and the run-out or cycle limit was set at 2×10^6 cycles.

The fatigue life of titanium and its alloys is dependent on the state of the surface finish. Surface finish greatly influences fatigue crack initiation, especially in unnotched specimens due to discontinuities present on the surface. A smooth surface finish generally delays fatigue crack initiation thereby increasing the crack initiation resistance and reducing the probability of the fatigue strength being a result of the different surface finishes instead of the microstructure present. To combat this effect, all the specimens tested (including the LST specimens) were prepared meticulously and the surface roughness was measured before fatigue testing.

The influence of surface modification by LST on fatigue life was characterised with respect to the parent material and RFW specimens only. The fatigue testing specimen sizes were designed according to ASTM standard E466-96. Figure 6-10 shows the dimension of the fatigue specimens. The specimens were designed to ensure identical maximum and nominal stress magnitudes at its centre without employing the use of any geometrical notches on it. One feature of the fatigue specimen was a continuous radius of 48 mm ($K_t = 1$).

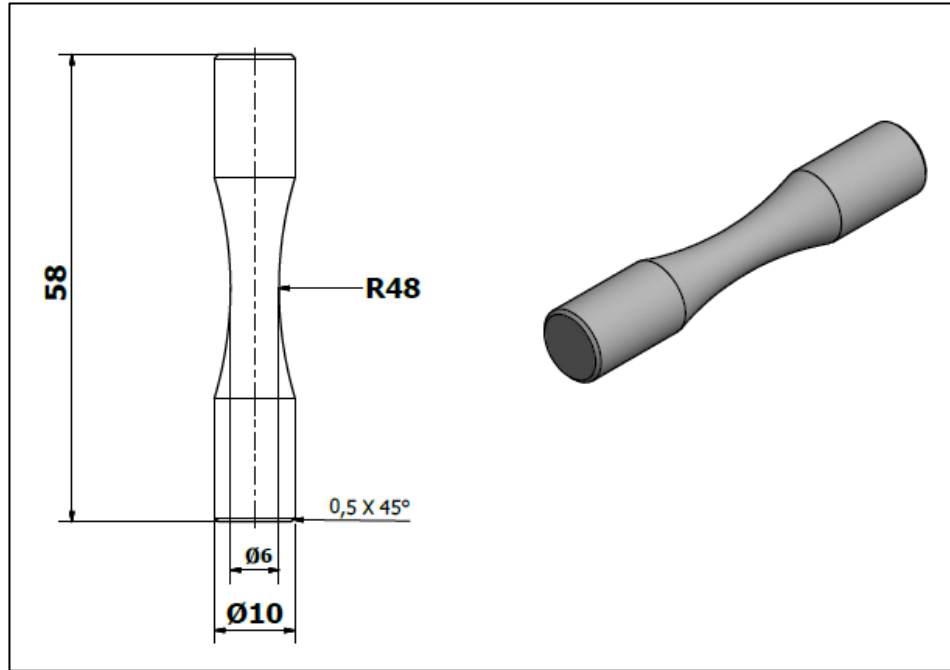


Figure 6-10: Fatigue specimen dimensions (all dimensions in mm).

6.3.1. Fatigue Data

The results of the fatigue tests of the parent, RFW and LST specimens are discussed in this section. Table 6-4, Table 6-5, Table 6-6 and Table 6-7 display the results of the fatigue testing performed on the parent, RFW specimens and LST specimens (low and high), respectively.

Table 6-4: Parent material fatigue test results.

	Stress (MPa)	Cycles	Remarks	Failure area	Position of failure	Crack Initiation Site
1	412	2 029 000	Run-out	N/A	N/A	N/A
2	455	2 010 000	Run-out	N/A	N/A	N/A
3	470	147 000	Failed	Parent	Middle	Surface
4	521	40 000	Failed	Parent	Middle	Surface
5	506	20 000	Failed	Parent	Middle	Surface
6	552	57 000	Failed	Parent	Middle	Surface
7	572	31 000	Failed	Parent	Middle	Surface
8	603	4 000	Failed	Parent	Middle	Surface
9	603	6 000	Failed	Parent	Middle	Surface

Table 6-5: RFW fatigue results.

	Stress (MPa)	Cycles	Remarks	Failure area	Position of failure	Crack Initiation Site
1	382	2 009 000	Run-out	N/A	N/A	N/A
2	398	88 000	Failed	HAZ	Middle	Surface
3	437	50 000	Failed	HAZ	Middle	Surface
4	480	21 000	Failed	HAZ	Middle	Surface
5	529	16 000	Failed	HAZ	Middle	Surface
6	553	6 000	Failed	HAZ	Middle	Surface
7	577	4 000	Failed	HAZ	Middle	Surface
8	577	3 000	Failed	HAZ	Middle	Surface

Table 6-6: LST low-power density specimen fatigue results.

	Stress (MPa)	Cycles	Remarks	Failure area	Position of failure	Crack Initiation Site
1	418	2 200 000	Run-out	N/A	N/A	N/A
2	429	2 107 000	Run-out	N/A	N/A	N/A
3	445	2 000 000	Run-out	N/A	N/A	N/A
4	484	45 000	Failed	Transition	Offset the middle	Surface
5	484	47 000	Failed	Transition	Offset the middle	Surface
6	549	15 000	Failed	Transition	Offset the middle	Surface
7	622	8 000	Failed	Transition	Offset the middle	Surface
8	661	15 000	Failed	Transition	Offset the middle	Surface

Table 6-7: LST High-power density specimen fatigue results.

	Stress (MPa)	Cycles	Remarks	Failure area	Position of failure	Crack Initiation Site
1	419.0	2 000 000	Run-out	N/A	N/A	N/A
2	437.1	596 000	Failed	Transition	Offset the middle	Surface
3	460.2	350 000	Failed	Transition	Offset the middle	Surface
4	493.0	37 000	Failed	Transition	Offset the middle	Surface
5	562.4	13 000	Failed	Transition	Offset the middle	Surface

Fatigue life plots of the three different specimens (LST, parent and RFW) are shown in Figure 6-11. The specimens were all similar and had polished surface finishes with no post weld heat treatment conducted on them.

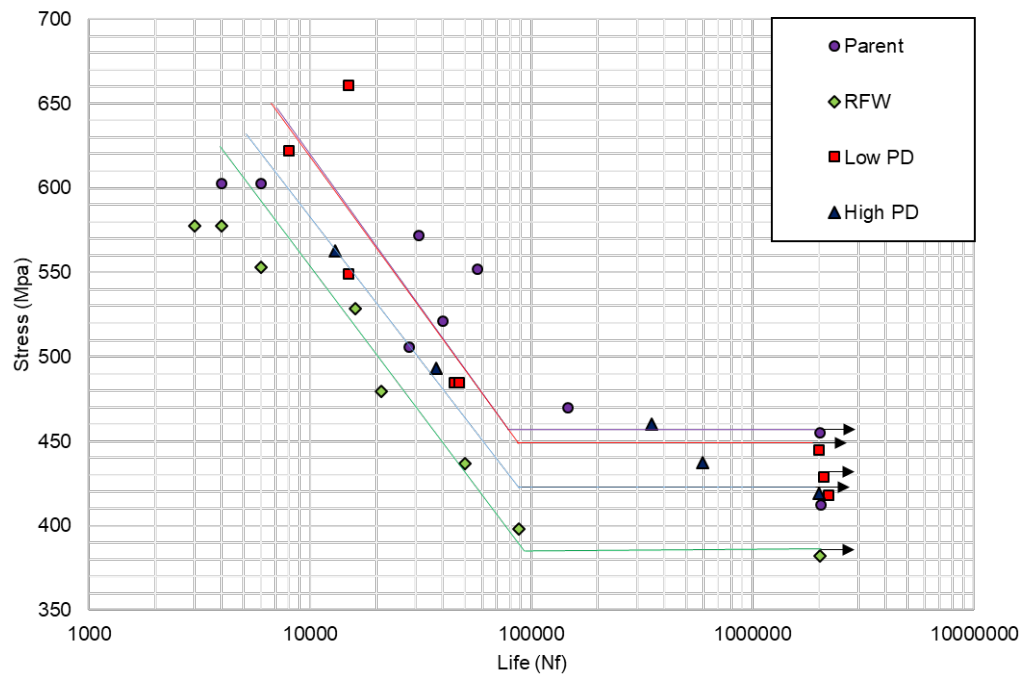


Figure 6-11: Fatigue life plot of the parent, RFW and LST specimens.

The fatigue results showed that both the LST specimens had a high fatigue strength compared to the RFW specimens. The low-power density specimen outperformed both the high-power density and the RFW specimens and achieved run-out (2 million cycles) at a strength of 445 MPa. As expected parent fatigue specimens had the highest achieved run-out at a stress of 455 MPa. The failure position of the parent material fatigue specimens was mainly located at the smallest diameter of the fatigue specimen geometry.

The RFW specimen had the lowest attained fatigue limit of 382 MPa. Crack initiation sites were predominantly located on the surface of the RFW specimens. The HAZ was the predominant initiation site, most probably related to the grain boundary transition zone of HAZ to parent material. This was clearly observed in the microstructure analysis shown in section 5.3.2 where the HAZ was observed to have a coarser grain structure.

Comparing both the RFW and low-power density specimens, fatigue strength was improved by at least 10% through LST processing. Of interest was the new position of failure, which was changed by the LST processing. The position of failure for the LST friction welded specimens at both power densities (low and

high), was analysed and compared to the RFW specimens. It was observed that because of the LST processing, the position of failure shifted from the HAZ in the RFW specimen to a position away from the RFW joint when specimens had been LST processed.

The shift in position of crack initiation was because of the introduction of a more homogenous and very fine microstructure within the RFW region by LST processing the surface. The microstructure introduced by LST had very fine α laths and very small colonies which are beneficial in terms of crack growth retardation purposes as numerous colonies therefore act as discontinuities by changing the crack path. This shift in position resulted in the failure being located on an area with a higher diameter than at the position of the RFW joint. Figure 6-12 illustrates the change in failure position for a friction welded LST processed specimen.

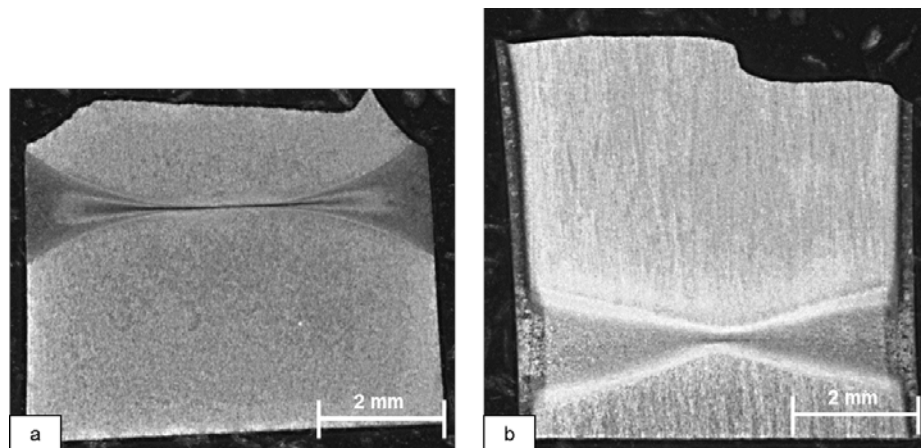


Figure 6-12: Example of the failure position after cross section the half fractured fatigue specimen a) RFW fatigue specimens and b) friction welded LST processed fatigue specimens.

For the two specimens processed using LST, it was observed that increasing the power density had an effect on the fatigue properties of the specimens. This was clearly observed between the low- and high-power density specimens. The fatigue performance observed correlated with the microstructure observed, as the high-power density LST specimen had a coarse lamella structure compared to the low-power density LST specimen. Power density, it seems, affects cooling rates which in turn affects the microstructure attained in the LST processed

specimens. The fatigue results also correlated with residual stress near the surface of the specimens, with higher power density specimens having a higher longitudinal tensile residual stress value compared to the low-power density specimens.

6.3.2. Fracture Surfaces of the LST, Parent and RFW specimens

This section quantifies the fracture surfaces of the parent, RFW and LST specimens. By examining the fracture surfaces, the topography and basic causes of failure can be determined. The crack initiation sites were examined for all the specimens that were fatigue tested. The crack nucleation or initiation sites were surface related due to the presence of a high nominal stress with no stress concentration present as identified using the appropriate ASM guidelines [37]. Due to the fatigue tests being conducted at constant amplitude, beach marks were not visible as they are produced only under variable amplitude conditions. Figure 6-13 displays examples of the fatigue fracture surfaces of the parent, RFW and LST + RFW specimens tested.

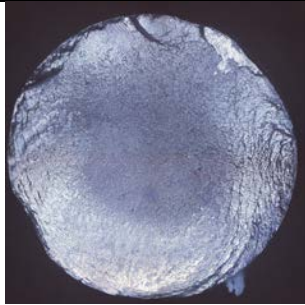


Specimen Name	Parent (521 MPA; 40 000 cycles)	RFW (398 MPA 88 000 cycles)	Low LST (484 MPA 45 000)
Fracture surface			

Figure 6-13: Examples of fatigue fracture surfaces (Additional fracture surfaces are shown in Appendix E)

The fracture surfaces were further analysed using a Scanning Electron Microscope (SEM). The fracture surfaces showed that the dominant failure mode was due to crack initiation on the surface of the fatigue specimen. The crack initiation at the surface predominantly indicated the presence of a high nominal

stress. The LST fracture surfaces indicated striation marks as shown in Figure 6-14.

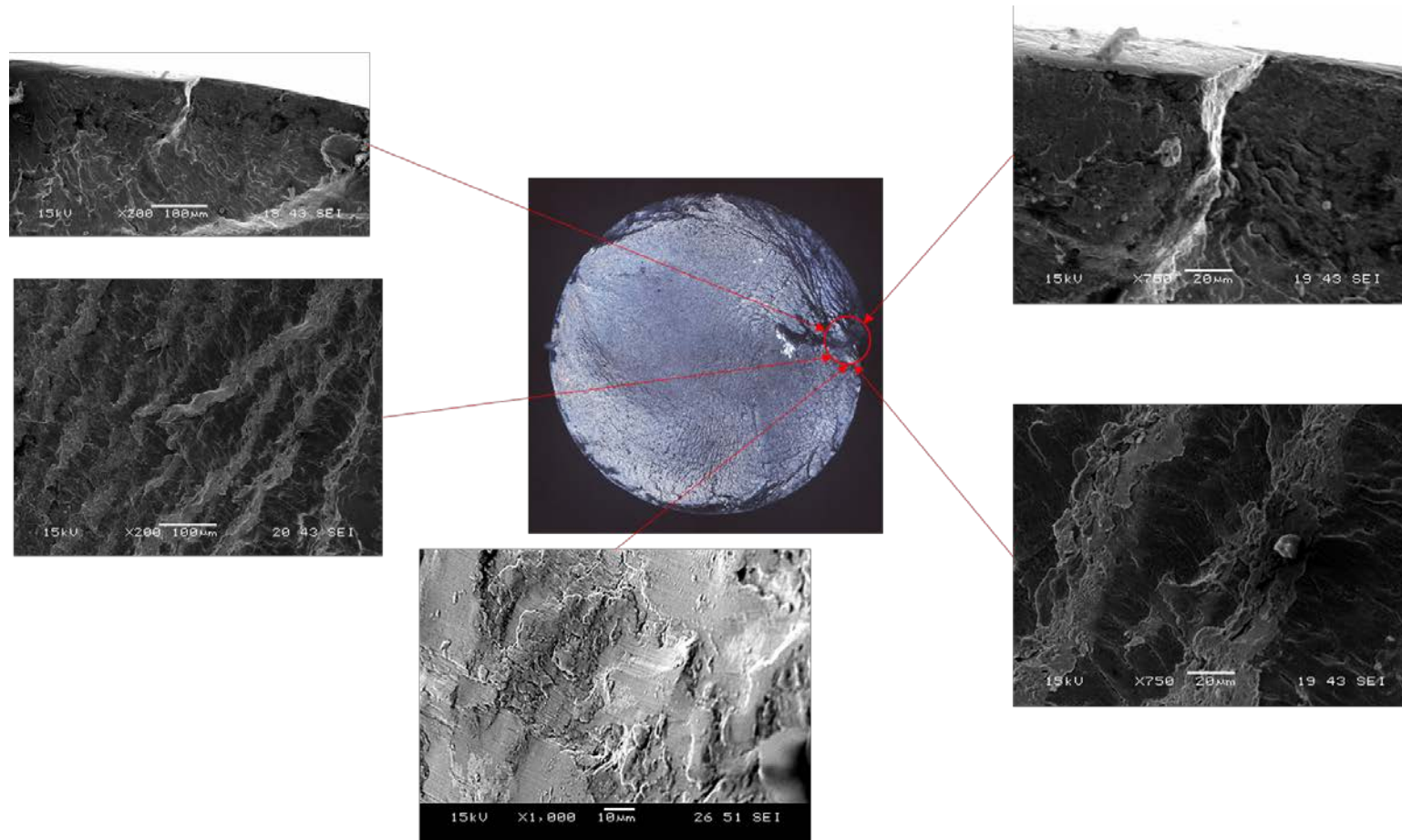


Figure 6-14: Crack initiation site with evidence of striations for LST fracture surface at a stress of 502 MPa (45 000 cycles).

6.4. Summary

The specimens used for fatigue testing were all in the polished condition. The specimens were polished to eliminate any surface defects. LST processing improved the fatigue properties of the RFW specimens. The position of failure shifted from the HAZ to outside the RFW joint. This change in position was attributed to the surface modification by LST thereby introducing a more homogenous microstructure at the surface of the specimen.

Additionally, it was also observed that the power density does play an important role in the fatigue properties of the laser surface treated specimens. Comparing the two LST specimens, it was observed that the high-power density specimen had the highest tensile residual stresses in the axial direction at a position of 0.2 mm from the surface and poor fatigue properties compared to the low-power density specimen. A link was established between the fatigue properties, residual stress and microstructure analysed in chapter 5.

Chapter 7. Conclusion and Future work

From the surveyed literature, it was established that there is little or no information relating to laser surface treatment as a post-processing technique for friction welded components. Therefore, the main objective of this research was to investigate the potential of LST as a post-processing technique for RFW Ti-6Al-4V ELI components by relating fatigue properties, residual stresses and microstructure.

The hypothesis of this research was stated as follows:

“The integrity of Rotary friction welded joints can be improved by introducing Laser surface treatment as a post-processing technique. The research will further unlock the mechanisms contributing to enhanced mechanical properties by linking interactions of different property changes”.

The research was completed in three stages, as follows:

- Laser surface treatment of 3 mm Ti-6Al-4V
- Laser surface treatment of the cylindrical parent Ti-6Al-4V ELI fatigue specimens
- Laser surface treatment of the rotary friction welded Ti-6Al-4V ELI cylindrical fatigue specimens

The LST of the 3 mm Ti-6Al-4V was conducted to establish an understanding of the process characteristics of LST processing. This phase quantified focus position and laser power by analysing the bead width and depth of penetration at different process parameters. It was concluded that the bead width and depth of penetration are greatly influenced by these two process parameters. By increasing the focus position (positive increase which defocusses the laser beam with reference to the specimen surface) at constant power, the depth of penetration was reduced while the LST surface bead width was increased. The uniformity of the LST zone was also affected by the focus position. At the

bottom of the LST zone, uniformity was observed at the focus position of 5 mm and above with an increase in the laser power also affecting the resultant also affecting the resultant shape of the base of the LST region. The microstructure and hardness profiles showed microstructure refinement leading to increased hardness in the LST region as compared to the parent material.

The second phase focused on the method of conducting LST on cylindrical specimens. From a series of tests, it was concluded that the method of LST to be employed in this research would involve the use of a non-continuous strategy. The non-continuous strategy aided in the establishment of a more homogenous and uniform LST processed region as compared to a continuous LST method. A continuous LST method led to a small LST depth of penetration at the process start, gradually increasing until the process end. This phenomenon was mainly due to the cold material at the start of the process before the temperature increased with each laser beam scan. A non-continuous method of laser surface treatment eliminated this problem by randomly treating the surface as opposed to continuous treatment.

The main phase of this research was the laser surface treatment of rotary friction welded cylindrical Ti-6Al-4V ELI specimens. The developed final matrix specimens analysed the three main primary process parameters; laser power, scanning speed and focus position. Secondary process parameters were derived which were energy input and power density. The LST experimental runs were then grouped into three categories in terms of energy input.

The following conclusions were drawn from the final matrix specimens.

Firstly, low energy input specimens had the lowest attained depth of penetration in comparison with the low and high energy input specimens. High energy input specimens had a clear uneven LST region depth of penetration due to the increased energy input. Medium energy input specimens had a uniformed LST zone, all around the specimen. The LST zone's depth of

penetration reached approximately 0.4 mm to 0.6 mm with visible overlapping induced by increased LST processed areas larger than the laser spot size. Power density increased the LST zone's depth of penetration at constant energy input.

Secondly, the high energy input specimens exhibited a highly degraded surface as compared to the medium and low energy input specimens, with low energy input specimens having the least degraded surface. Finally, it was concluded that energy input had an effect on the Micro Vickers hardness distribution, with a specimen processed at the medium energy input showing linear hardness profile values across the LST zone through to the unaffected region. The hardness of the two specimens was quantified in the vertical cross section cut plane as opposed to the horizontal one undertaken for all the final matrix specimens. The hardness profile of the LST zone varied significantly from that of the friction welded joint. Laser surface treatment introduced a similar hardness distribution on the near surface of the specimen thereby eliminating the hardness variation that was exhibited in the RFW specimen. The hardness variation in the welded zone was as a result of microstructural variation in the parent, HAZ and weld zone. This hardness variation provided loci for crack initiation during fatigue testing of the friction welded specimen. The HAZ had the highest attained hardness in a friction welded specimen with no LST processing.

The microstructure of the specimen could not be fully resolved using an Optical Microscope, therefore two LST specimens processed at two different sets of process parameters were selected for further analysis by EBSD and Synchrotron X-ray diffraction techniques. The specimens that were selected were in the medium energy input level but at different power densities. The microstructure developed during LST was different to that of the parent and any of the microstructural regions of a friction welded joint. The microstructure in the LST zone near the surface was a very refined acicular α lamella (needle-like α) structure. The texture of the microstructure varied between the two LST friction welded specimens, with the high-power density specimen having a

coarse structure compared to the low-power density specimen. The final observed colonies size and α -lamella depth of penetration of the final observed colonies was greatly influenced by cooling rate, with the resultant coarse structures in the high-power density specimen as a result of slow cooling rates. Owing to LST processing, there was virtually no β phase in the LST zone as shown by the EBSD phase maps of both specimens (high and low -power density). It was therefore concluded that the process of LST occurred above the β transus and that the microstructure observed was mainly governed by the heating and cooling phase. Although temperature at the surface could not be measured, it was assumed that the melting temperature of 1660 °C was probably reached because of the similarity of the microstructure to that observed in laser surface melting.

The through-depth residual stresses profile of the two LST specimens were measured through synchrotron X-ray diffraction. The surface residual stresses profile showed that the high power density specimen had a high surface tensile residual stress in the axial direction as compared to the low-power density specimen. These results demonstrated that at a highpower density, the tensile residual stresses are increased due to thermal contraction in the molten LST pool. Considering that the specimen was in the unpolished condition, it was concluded that polishing would affect the surface residual stresses of the specimen.

Fatigue testing was conducted on the LST, RFW and parent specimen. The fatigue specimens tested were all in the polished condition and were tested at a stress ratio of $R = -1$ using a rotary bending fatigue machine. Parent specimens had the highest fatigue strength at runout of 455 MPa. The LST processed low-power density, had the second highest attained fatigue strength of 445 MPa at run-out compared to that of the LST and RFW specimens. The parent, LST and RFW specimens all had different failure positions. The failure position in the parent specimen was located in the reduced section, centre of the specimens. Crack initiation sites in the RFW specimens were located in the HAZ, the transition between the parent and the

weld zone. The HAZ as shown in the RFW joint EBSD analysis had coarse and elongated grains as compared to the parent and weld zone, therefore crack initiation sites were located in this zone. Crack initiation sites in the LST were not located at the RFW joint interface because of the very fine lamella microstructure introduced on the surface by the process of LST, especially for the low-power density specimen.

The high power density specimen exhibited low fatigue properties compared to the low-power density specimen. A microstructural variation was noticed between the two different power density specimens. As has been discussed, the high power density specimen had coarse microstructure compared to the low-power density specimen. It was concluded that the microstructure played an important role in the fatigue properties of the LST. It was also observed that most of the specimens did not reach final fracture due to slow crack propagation rates as a result of the lamella microstructure.

In conclusion, the major benefits introduced through laser surface treatment of small friction welded Ti-6Al-4V ELI components were as follows:

- A post surface treatment process for small complex friction welded components, highly adaptable and flexible aiding in the manufacture of near net components.
- A uniform and homogenous microstructure, aiding in the elimination of microstructure variations observed in friction welded components. A decreased hardness variation on the surface of specimens.
- Introduction of a refined microstructure which inhibited crack initiation in the welded region and could easily outperform the parent material at high stresses.

In this thesis, the research detailing a post-processing method using laser surface treatment on small friction welded Ti-6Al-4V has provided a number of avenues for further investigation in order to close the gap in knowledge with

regard to using LST as a post-processing technique. The suggested areas of future study are as follows:

- Measurement of surface temperature during the process of LST would enable the determination as to whether the process is above or below the melting temperature. The temperature could be used to quantify the cooling rates achieved during the process of LST. This temperature measurement could also be used to monitor the process repeatability.
- Determination of the energy process model, considering both heating and cooling phase. The envisaged process model would assist in calculating the process efficiency and its benefit to industry through a cost analysis.
- Microstructural characterisation through EBSD would assist in characterising the influence of microstructure texture on fatigue performance after the process of LST.
- Development of a statistical model which would aid in predicting the fatigue performance of LST specimens conducted at different process parameters.

References

1. Meyer A. Friction Hydro Pillar Processing Bonding Mechanism and Properties. GKSS-Forschungszentrum Geesthacht GmbH: Von der Gemeinsamen Fakultät für Maschinenbau und Elektrotechnik der Technischen; 2003.
2. Nicholas E, D. Friction Processing Technologies. Welding in the World. 2003; 47((11-12), p.2-9).
3. Montealegre M, CAsto G, Rey P, Arias J, Vazquez P, Gonzalez M. Surface treatments By Laser Technology. Contemporary Materials. 2010; 1-1.
4. Temmler A, Walochnik MA. Surface structuring by remelting of titanium alloy Ti6Al4V. Laser Applications. 2015; 27.
5. Merwe Hvd. Variable Amplitude fatigue Analysis and prediction of Rotary Friction Welded Ti-6Al-4V [Masters Dissertation]. Port Elizabeth: Nelson Mandela Metropolitan University; 2016.
6. KGaA W-VVGC. Titanium and Titanium Alloys. Fundamentals and Applications. Leyens C, Peters M, editors. Köln 2003.
7. Donachie MJ. Titanium: A Technical Guide. Second edition end: ASM International; 2007 October 2007.
8. RMI I, Metals, Company. Titanium Alloy Guide.
9. Donachie MJ. Titanium: A Technical Guide. Ohio: ASM International; 2000.
10. Ninomi M. Mechanical properties of biomedical titanium alloys. Material Science and engineering. 1998; A243.
11. Smith LS, Threadgill P, Gittos M. Welding Titanium: A designers and users handbook. Peacock D, editor: The Welding Institute; 1999.

12. Venkatesh BD, Chen DL, Bhole SD. Effect of heat treatment on mechanical properties of Ti–6Al–4V ELI alloy. *Materials Science and Engineering: A*. 2009; 506(1-2):117-24.
13. Group TTI. *Welding Titanium: A designers and users handbook*. World Center for Materials Joining Technology (TWI). 1999.
14. Kingsley-Jones M. *Flight Global Aviation Connected Web site* 2007.
15. Gammon LM, Briggs RD, Packard JM, Batson KW, Boyer R, Dombay CW. *Metallography and Microstructures of Titanium*. ASM Handbook.9.
16. Žitňanský M, Čaplovič L. Effect of the thermomechanical treatment on the structure of titanium alloy Ti6Al4V. *Journal of Materials Processing Technology*. 2004; 157-158:643-9.
17. Sienawski J, Ziąja W, Kubiak K, Motyka M. *Microstructure and Mechanical Properties of High Strength Two-Phase Titanium Alloys: InTech*; 2013.
18. Tsikayi D. *Friction Hydro Pillar Riveting Process of Ti-6Al-4V Titanium sheet [Masters Dissertation]*. Port Elizabeth, Nelson Mandela Metropolitan University; 2015.
19. Gil FJ, Ginebra MP, Manero JM, Planell JA. Formation of α -Widmanstätten structure - effects of grain size and cooling rate on the Widmannstätten morphologies and on the mechanical properties of Ti6Al4V alloys *Journal of Alloys and Compounds*.329.
20. Lutjering G. Influence of processing on the microstructure and mechanical properties of α -B titanium alloys. *Materials Science and Engineering: A*. 1998; A243.
21. Nalla RK, Boyce BL, Campbell JP, Peters JO, Ritchie RO. Influence of Microstructure on High-Cycle Fatigue. *Metallurgical and Materials Transactions*. 2002; 33A.

22. Kimura M, Ichihara A, Kusaka M, Kaizu K. Joint properties and their improvement of AISI 310S austenitic stainless steel thin walled circular pipe friction welded joint. *Materials & Design*. 2012; 38:38-46.
23. Kimura M, Seo K, Kusaka K, Fuji A. Observation of joining phenomena in friction stage and improving friction welding method. *Journal of Solid Mechanics and Materials Engineering*. 2009.
24. Pinhero GA. Local reinforcement of magnesium components by friction processing: determination of bonding mechanisms and assessment of joint properties. [Dissertation]: Vom Promotionausschuss der Technischen Universität Hamburg-Harburals.; 2008.
25. Hattingh DG, James MN, Newby M, Scheepers R, Doubell P. Damage assessment and refurbishment of steam turbine blade/rotor attachment holes. *Theoretical and Applied Fracture Mechanics*. 2016; 83:125-34.
26. Hattingh DG, Wielligh Lv, Thomas W, James MN. Friction processing as an alternative joining technology for the nuclear industry. *The Journal of the Southern African Institute of Mining and Metallurgy*. 2015; 115.
27. Bisadi H, Tour M, Tavakoli A. The Influence of Process Parameters on Microstructure and Mechanical Properties of Friction Stir Welded Al 5083 Alloy Lap Joint. *American Journal of Materials Science*. 2011.
28. James M, Hattingh DG, Bradley GR. Weld tool travel speed effects on fatigue life of friction stir welds in 5083 aluminium. *International Journal of Fatigue*. 2003; 25(12):1389-98.
29. Thomas WM, Dolby E. Friction stir welding developments 6th International Conference on Trends in Welding Research; 15-19 April; Pine Mountain, Georgia, USA2002.

30. Mashinini PM. Dynamic properties of 3 mm Ti-6Al-4V laser beam and friction stir welded sheets: Nelson Mandela Metropolitan University; 2015.
31. García A. BLISK Fabrication by Linear Friction Welding: InTech; 2011 [Available from: <https://www.intechopen.com/books/advances-in-gas-turbine-technology/blisk-fabrication-by-linear-friction-welding>].
32. Yates A. The Effect of Microstructure on Mechanical Properties in Inertia Welded Titanium 6-4. Birmingham: University of Birmingham; 2015.
33. Thomas W. Leading Edge - Friction Hydro Pillar Processing. TWI Connect. 1992.
34. Kimura M, Inoue H, Kusaka M, Kaizu K, Fuji A. Analysis Method of Friction Torque and Weld Interface Temperature during Friction Process of Steel Friction Welding. *Journal of Solid Mechanics and Materials Engineering*. 2010; 4(3).
35. Avinash M, Chaitanya GVK, Giri DK, Upadhya S, Muralidhara BK. *Microstructure-and-Mechanical-Behaviuor-of-Rotary-Friction-Welded-Titanium-Alloys.pdf*. *International Journal of Mechanical, Aerospace, Industrial, Mechatronic and Manufacturing Engineering*. 2007; 1(11).
36. Vander Voort G, James H. *ASM Handbook vol. 9. Metallography and Microstructures*, ASM International, OH (9th printing, March 2000). 2004.
37. ASM International. *Fatigue Failures. Principles of Failure Analysis*. Ohio 2007
38. Schijve J. *Fatigue of Structures and Materials*. Dordrecht: Kluwer Academic Publishers; 2001.
39. Issler L. *Safety and Lifetime Analysis for Engineering Structures*. University of Applied Sciences Esslingen; 2009.
40. Hosseini S. *Fatigue of Ti-6Al-4V*. 2012.

41. G. Schroeder, Albrecht J, Luetjering G. Fatigue crack propagation in titanium alloys with lamellar and bi-lamellar microstructures G Schroeder, J Albrecht *, G Luetjering. 2001; A319.
42. Ritchie RO, Boyce BL, Campbell JP, Roder O, Thompson AW, Milligan WW. Thresholds for high-cycle fatigue in a turbine engine Ti–6Al–4V alloy International Journal of Fatigue. 1998; 21.
43. Jeong D, Kwon Y, Goto M, Kim S. High cycle fatigue and fatigue crack propagation behaviours of β -annealed Ti-6Al-4V alloy. International Journal of Mechanical and Materials Engineering. 2017; 12(1).
44. Schroeder G, Albrecht J, Luetjering G. Fatigue crack propagation in titanium alloys with lamellar and bi-lamellar microstructures Materials Science and Engineering: A. 2001.
45. Banerjee D, Williams JC. Microstructure and Slip Character in Titanium Alloys. Def Sci J. 1986; 36.
46. Sieniawski J, Ziaja W, Kubiak K, Motyka M. Microstructure and mechanical properties of high strength two-phase Titanium alloys. InTech 2013.
47. Wu GQ, Shi CL, Sha W, Sha AX, Jiang HR. Effect of microstructure on the fatigue properties of Ti–6Al–4V titanium alloys. Materials & Design. 2013; 46:668-74.
48. Pyoun Y, Suh C, Cho I, Lee K, Ahn J, Cherif A. Application of UNSM (ultrasonic nanocrystal surface modification) technology for increasing fatigue strength of Ti-6Al-4V ELI spine rod and for decreasing 15% of the spine rod diameter. Proceedings of ICSP. 2011.
49. James MN, Hattingh DG, Asquith D, Newby M, Doubell P. Residual stresses in condition monitoring and repair of thermal power generation components. Theoretical and Applied Fracture Mechanics. 2017.
50. Withers P, Bhadeshia H. Residual stress. Part 1 – Measurement techniques. . Materials Science and Technology. 2001; 17.

51. Prev y P, Jayaraman N, Ravindranath R, editors. Introduction of residual stresses to enhance fatigue life performance in initial design. Turbo Expo; Proceedings of Turbo Expo June 14-17, 2004; Vienna: Lambda Technologies; 2001.
52. Fitzpatrick ME, Fry AT, Holdway P, Kandil FA, Shackleton J, Suominen L. Determination of Residual Stresses by X-ray Diffraction. Measurement Good Practice Guide 2005; 52.
53. An introduction x-ray diffraction residual stress measurement. www.protoxrd.com; 2011.
54. X-ray diffraction residual stress techniques. www.lambdatechs.com.
55. James MN, Hattingh DG, Asquith D, Newby' M, Doubell P. Applications of Residual Stress in Combatting Fatigue and Fracture. *Procedia Structural Integrity*. 2016; 2:11-25.
56. Olson WA, Bert CW. Analysis of Residual Stresses in Bars and Tubes of Cylindrically Orthotropic Materials. *Experimental Mechanics*. 1966.
57. Bhadeshia HKDH. Developments in martensitic and bainitic steels: role of shape deformation *Material Science and engineering*. 2004; A 378:34-9.
58. Peel M, Steuwer A, Preuss M, Withers PJ. Microstructure, mechanical properties and residual stresses as a function of welding speed in aluminium AA5083 friction stir welds. *Acta Materialia*. 2003; 51(16):4791-801.
59. Steuwer A, Hattingh DG, James MN, Singh U, Buslaps T. Residual stresses, microstructure and tensile properties in Ti–6Al–4V friction stir welds. *Science and Technology of Welding and Joining*. 2013; 17(7):525-33.
60. Moat RJ, Hughes DJ, Steuwer A, Iqbal N, Preuss M, Bray SE, et al. Residual Stresses in Inertia-Friction-Welded Dissimilar High-Strength Steels. *Metallurgical and Materials Transactions A*. 2009; 40(9):2098-108.

61. Dawes C. Laser Welding. Toronto, Canada: McGraw-Hill Inc.; 1992.
62. Majumdar Jd, Manna I. Laser processing of materials. S⁻adhan⁻ a. 2003; 28.
63. Kusinski J, Kac S, Kopia A, Radziszewska A, Rozmus-Górnikowska M, Major B, et al. Laser modification of the materials surface layer – a review paper. Bulletin of the Polish Academy of Sciences: Technical Sciences. 2012; 60(4).
64. Astrocamp. Fiber Optics: Continuing the Light Discussion [Available from: <http://astrocampschool.org/fiber-optics-light/>].
65. Majumdar JD, Weisheit A, Mordike BL, Manna I. Laser surface alloying of Ti with Si, Al and SiAl for an improved oxidation resistance. Materials Science and Engineering: A. 1998.
66. Badkar DS, Pandey KS, Buvanashakaran G. Effects of laser phase transformation hardening parameters on heat input and hardened-bead profile quality of unalloyed titanium. Transactions of Nonferrous Metals Society of China. 2010; 20(6):1078-91.
67. Becker TH, Beck M, Scheffer C. Microstructure and mechanical properties of direct metal laser sintered Ti-6Al-4V. South African Journal of Industrial Engineering. 2015.
68. Biswas S, Habib Alavi S, Harimkar SP. Laser surface melting of Ti-6Al-4V under the influence of ultrasonic vibrations. Materials Letters. 2015; 159:470-3.
69. Chikarakara E. Laser surface modification of biomedical alloys: Dublin City University; 2012.
70. Chikarakara, E., S. Naher and D. Brabazon (2010). "Process mapping of laser surface modification of AISI 316L stainless steel for biomedical applications." Applied Physics; Material Science and Processing 101: 367-371.

71. Singh R, Kurella A, Dahotre NB. Laser surface modification of Ti-6Al-4V: wear and corrosion characterization in simulated biofluid. *J Biomater Appl.* 2006; 21(1):49-73.
72. Badkar DS, Pandey KS, Buvanashakaran G. Effects of laser phase transformation hardening parameters on heat input and hardened-bead profile quality of unalloyed titanium. *Transactions of Nonferrous Metals Society of China.* 2010; 20(6):1078-91. 83.
73. Akgun OV, Inal OT. Laser surface modification of Ti-6Al-4V alloy. *Journal of Material Science.*29:1159 - 68.
74. Sematech N. Engineering Statistics Handbook [Available from: <http://www.itl.nist.gov/div898/handbook/pri/section3/pri33.htm>
75. Hutchings MT, Withers PJ, Holden TM, Lorentzen T. Introduction to the Characterization of Residual Stress by Neutron Diffraction.
76. Qureshi N. Elastic neutron scattering Neutron for Science; [Available from: <http://www.esrf.eu/files/live/sites/www/files/events/conferences/HSC/HS18/SC18/Qureshi.pdf>
77. Steuwer A, Santisteban JR, Turski M, Withers PJ, Buslaps T. High-resolution strain mapping in bulk samples using full-profile analysis of energy-dispersive synchrotron X-ray diffraction data. *Journal of Applied Crystallography.* 2004; 37(6):883-9

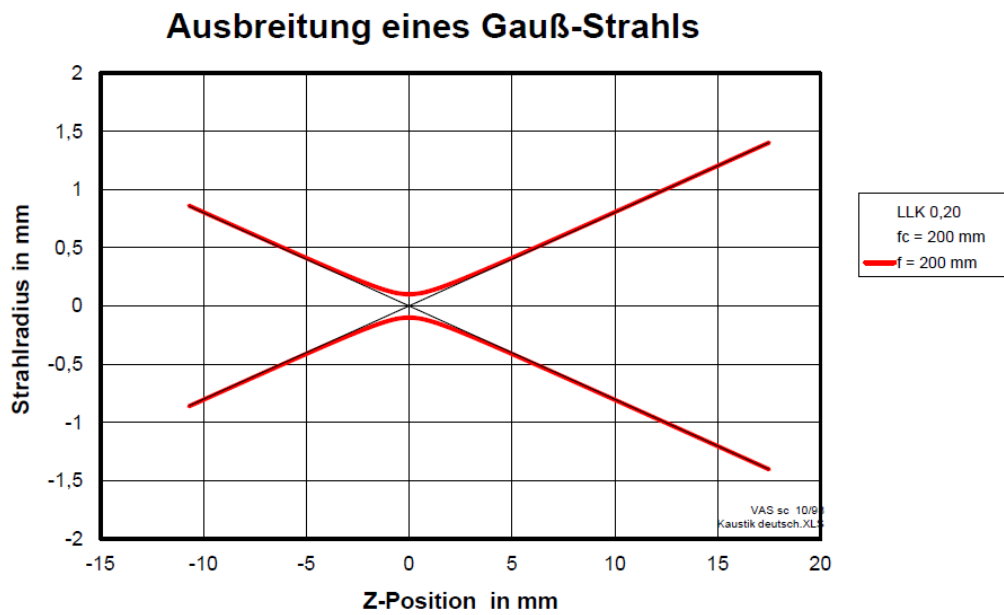
Appendix A: Laser source characteristics and focus position graph

Laser source characteristics

Laser Parameters	
Laser power at the work piece	4000 W
Power constancy at rated laser output	± % with active power regulation
Continuously adjustable power range	80 W – 4000 W with active power regulation
Beam quality	8 mm mrad
Numerical aperture	0.1
Wavelength	1030 nm
Min. Laser light cable diameter	200 µm
Structural design	
Width	1175 mm
Height	1430 mm
Depth	725 mm
Max. number of laser light cables	2
Installation	
Protection type	IP54
Ambient temperature	10 °C -50 °C

Spot size determination graph

This graph was used in calculating the spot size at certain defocus positions. The spot increases as the defocus position of the beam increased.



Spot size calculation graph.

Appendix B: Friction weld upset verification and analysis

Feedback as highlighted in Figure 3-11:

Upset distance analysis

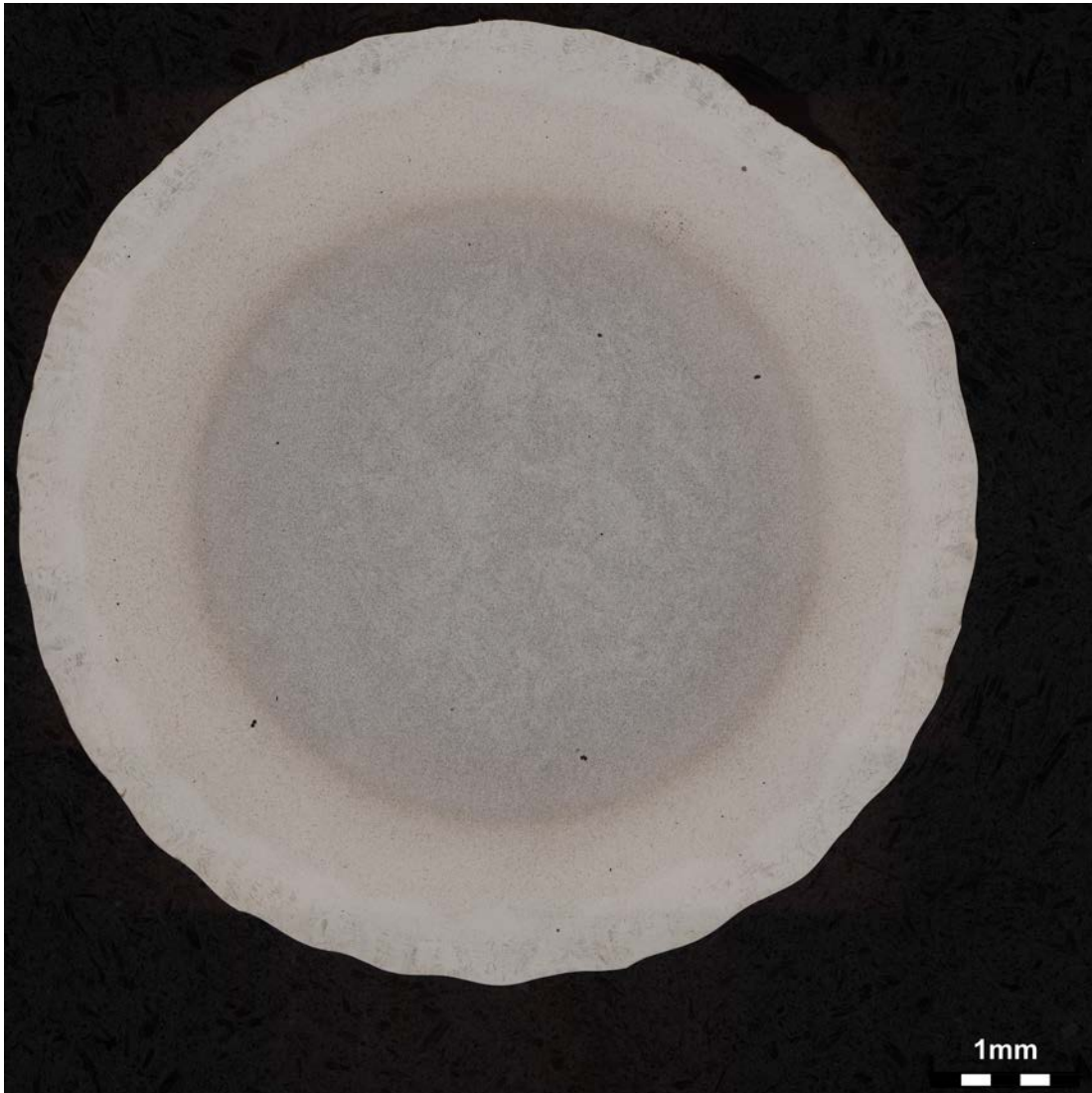
Rotary friction weld number	Upset distance (mm)	Rotary friction weld number	Upset distance (mm)	Rotary friction weld number	Upset distance (mm)
1	1.23	16	1.32	30	1.2
2	1.31	17	1.25	31	1.25
3	1.11	18	1.24	32	1.2
4	1.45	19	1.22	33	1.23
5	1.13	20	1.09	34	1.22
6	1.20	21	1.11	35	1.11
7	1.20	22	1.36	36	1.15
8	1.11	23	1.16	37	1.16
9	1.2	24	1.23	38	1.23
10	1.2	25	1.34	39	1.23
11	1.2	26	1.32	40	1.30
12	1.23	27	1.48		
13	1.22	28	1.22		
14	1.23	29	1.20		

Appendix C: Macrograph of different energy input levels

Specimen: LST 1

Energy Input (J/mm)	8.33
Power Density (W/mm ²)	795.8
Energy input category	Medium

Macrograph



Specimen: LST 2

Energy Input (J/mm)	20.83
Power Density (W/mm²)	795.8
Energy input category	High

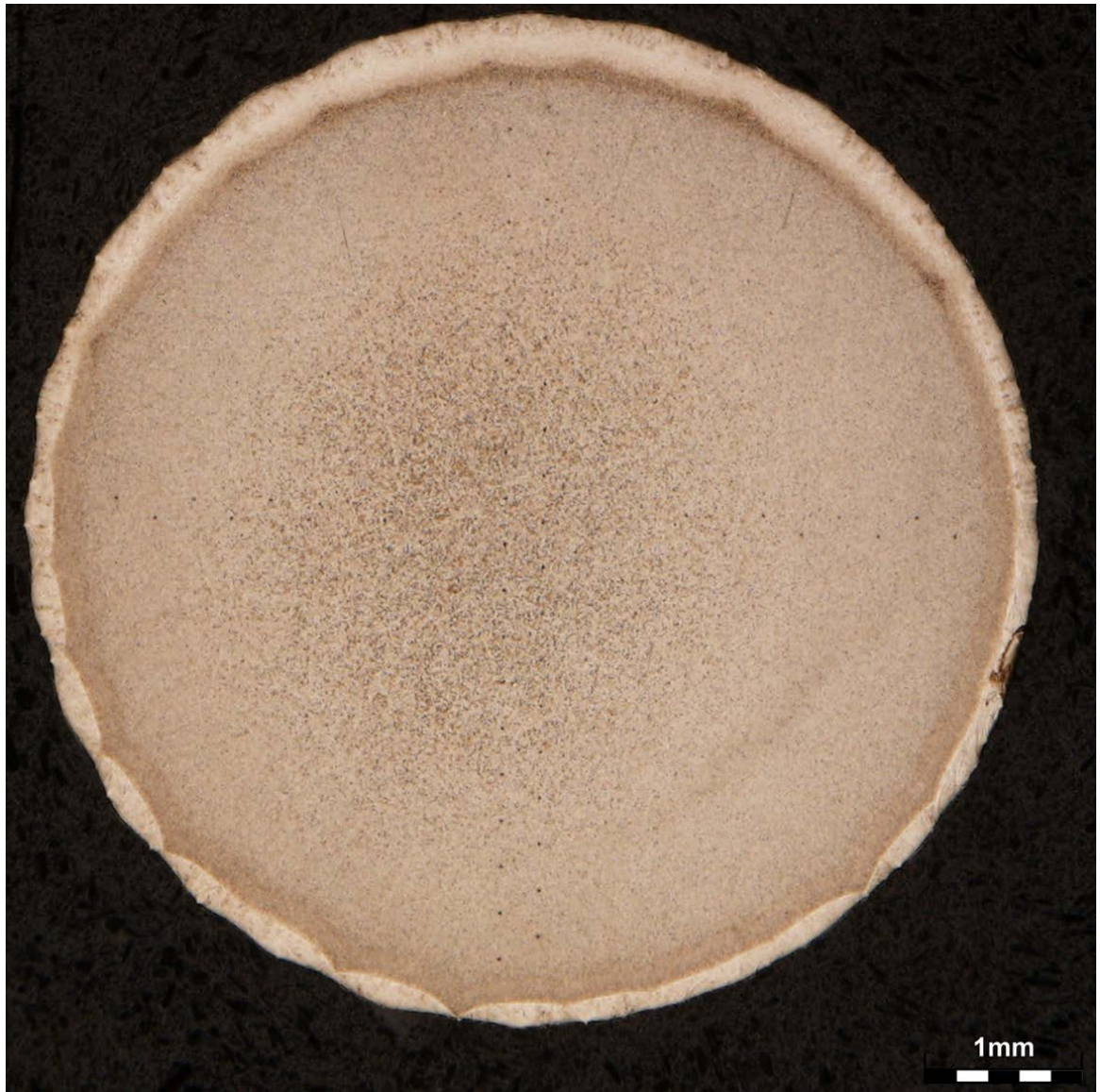
Macrograph



Specimen: LST 4

Energy Input (J/mm)	5.21
Power Density (W/mm²)	795.8
Energy input category	low

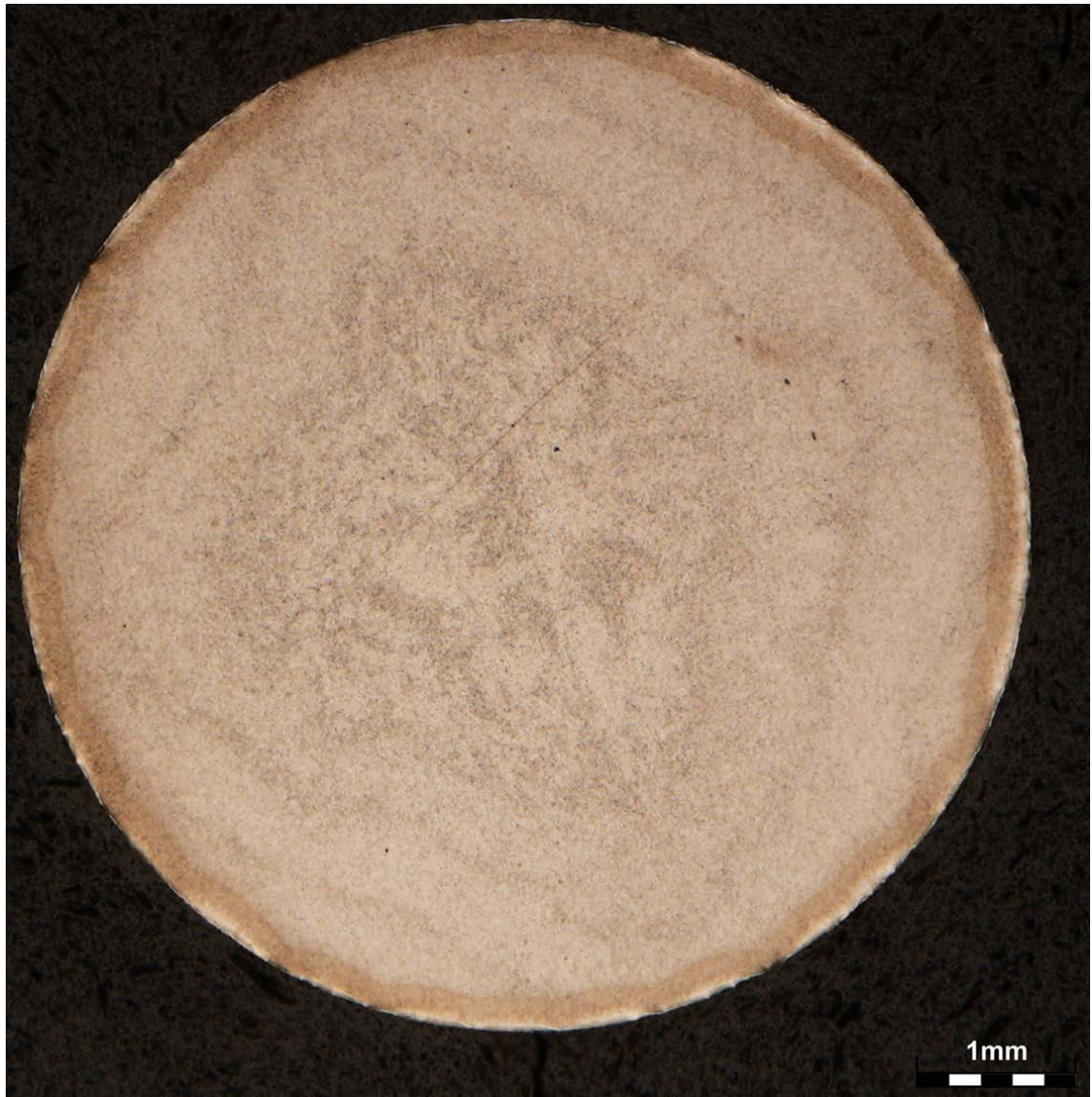
Macrograph



Specimen: LST 6

Energy Input (J/mm)	3.95
Power Density (W/mm²)	302.9
Energy input category	low

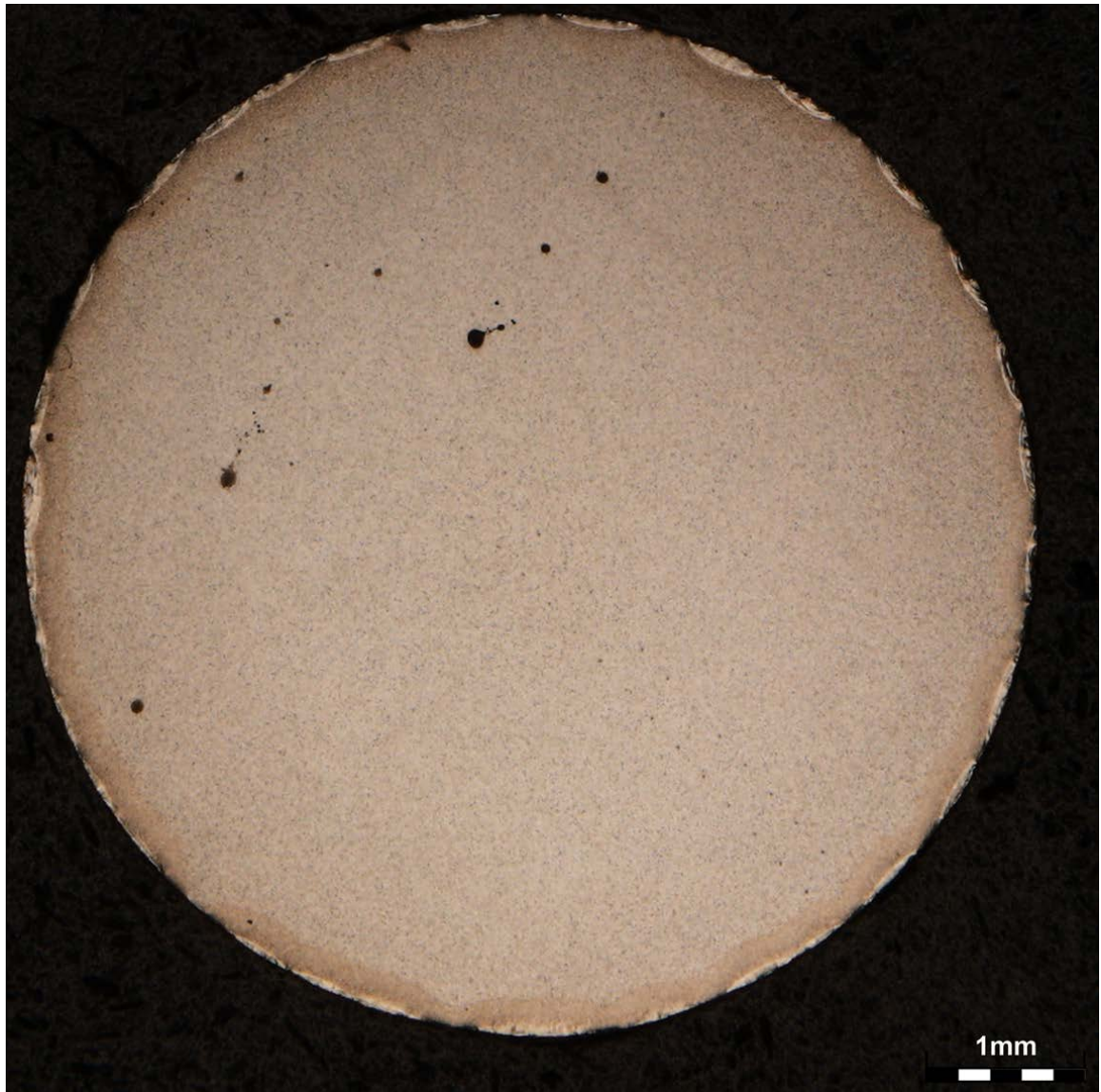
Macrograph



Specimen: LST 11

Energy Input (J/mm)	3.33
Power Density (W/mm²)	318.3
Energy input category	Low

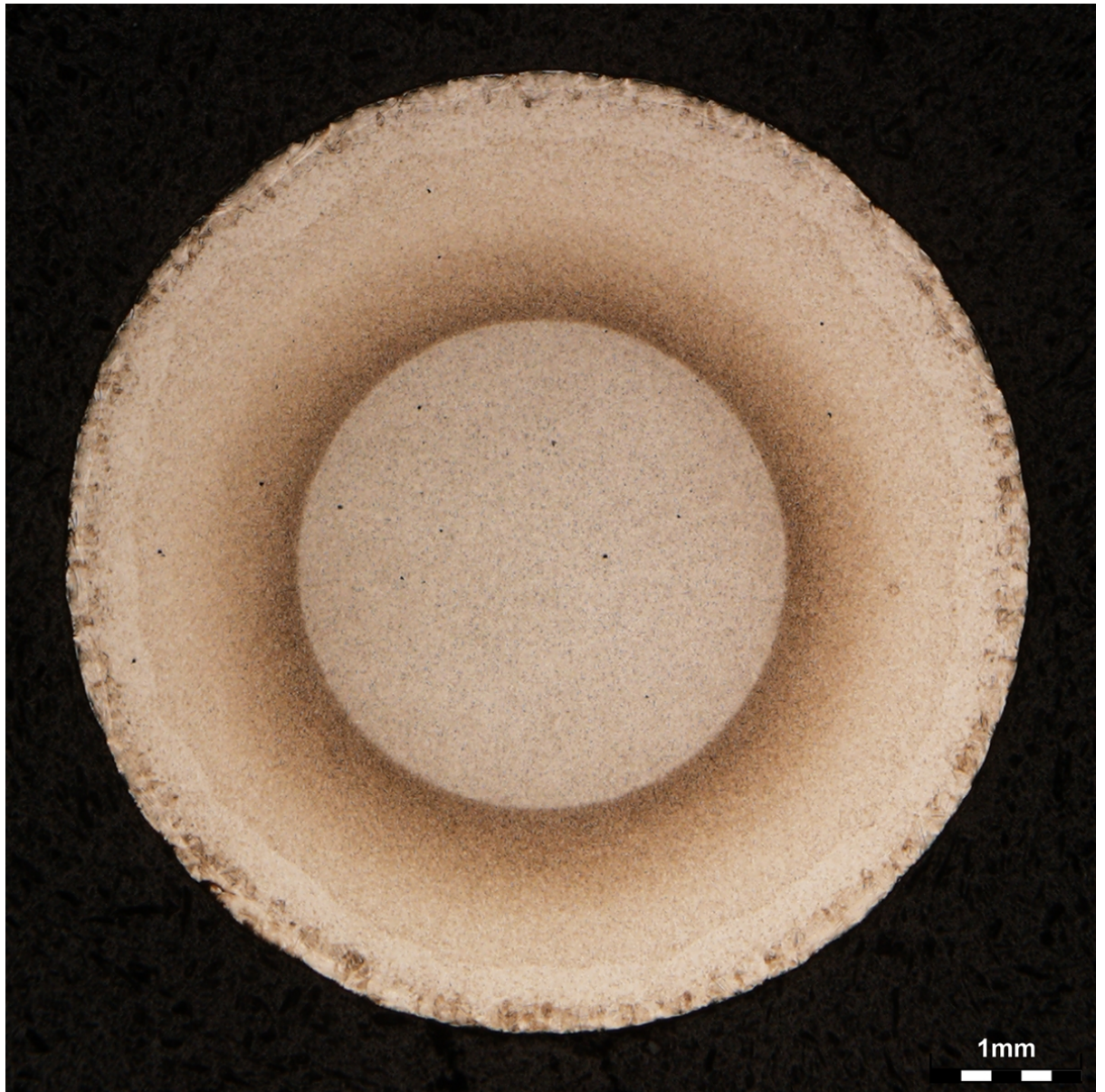
Macrograph



Specimen: LST 12

Energy Input (J/mm)	8.33
Power Density (W/mm ²)	2555.5
Energy input category	Medium

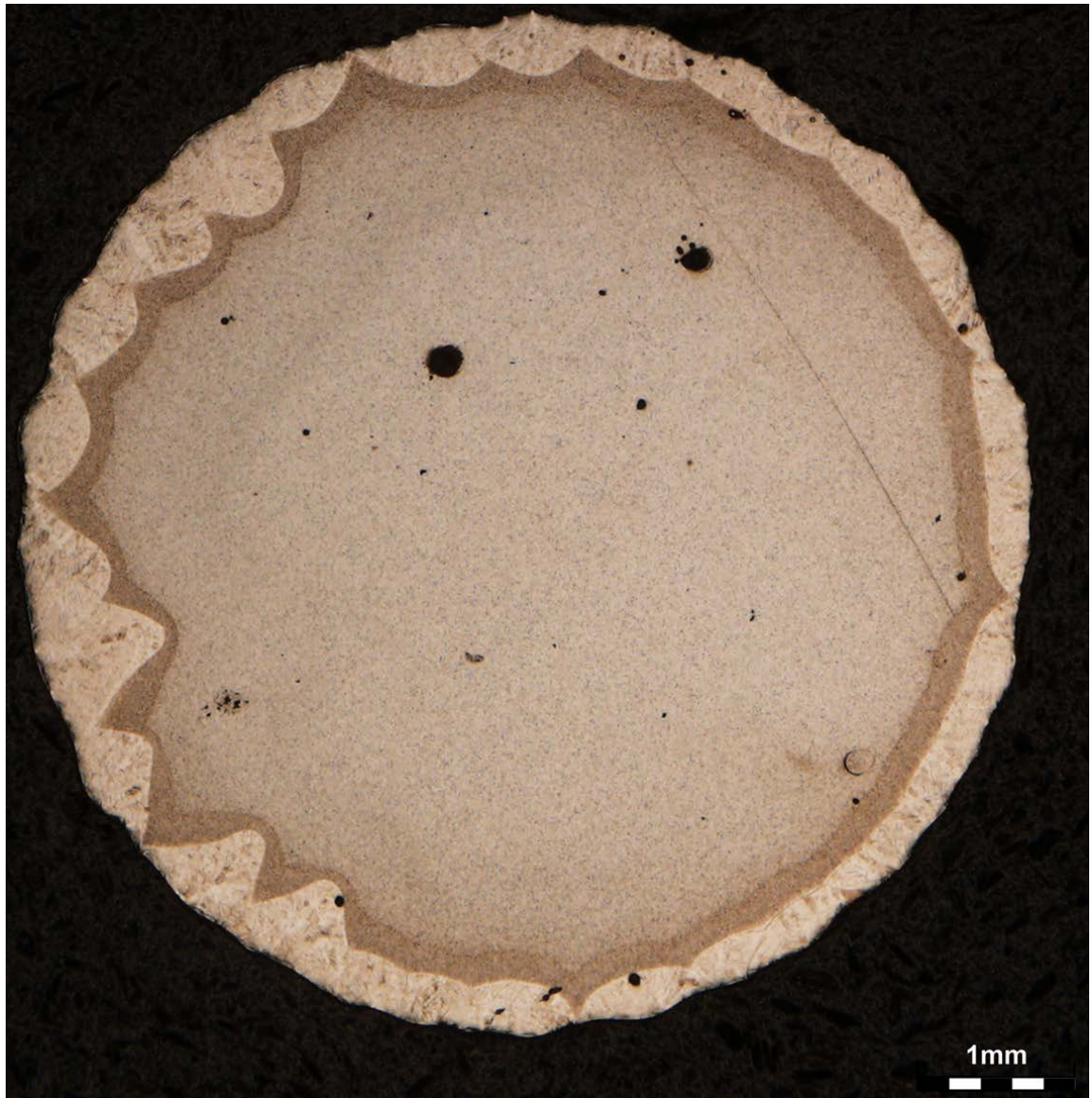
Macrograph



Specimen: LST 13

Energy Input (J/mm)	8.33
Power Density (W/mm ²)	310.8
Energy input category	Medium

Macrograph



Specimen: LST 15

Energy Input (J/mm)	17.58
Power Density (W/mm ²)	2555.5
Energy input category	High

Macrograph



Specimen: LST 16

Energy Input (J/mm)	8.33
Power Density (W/mm²)	638.9
Energy input category	Medium

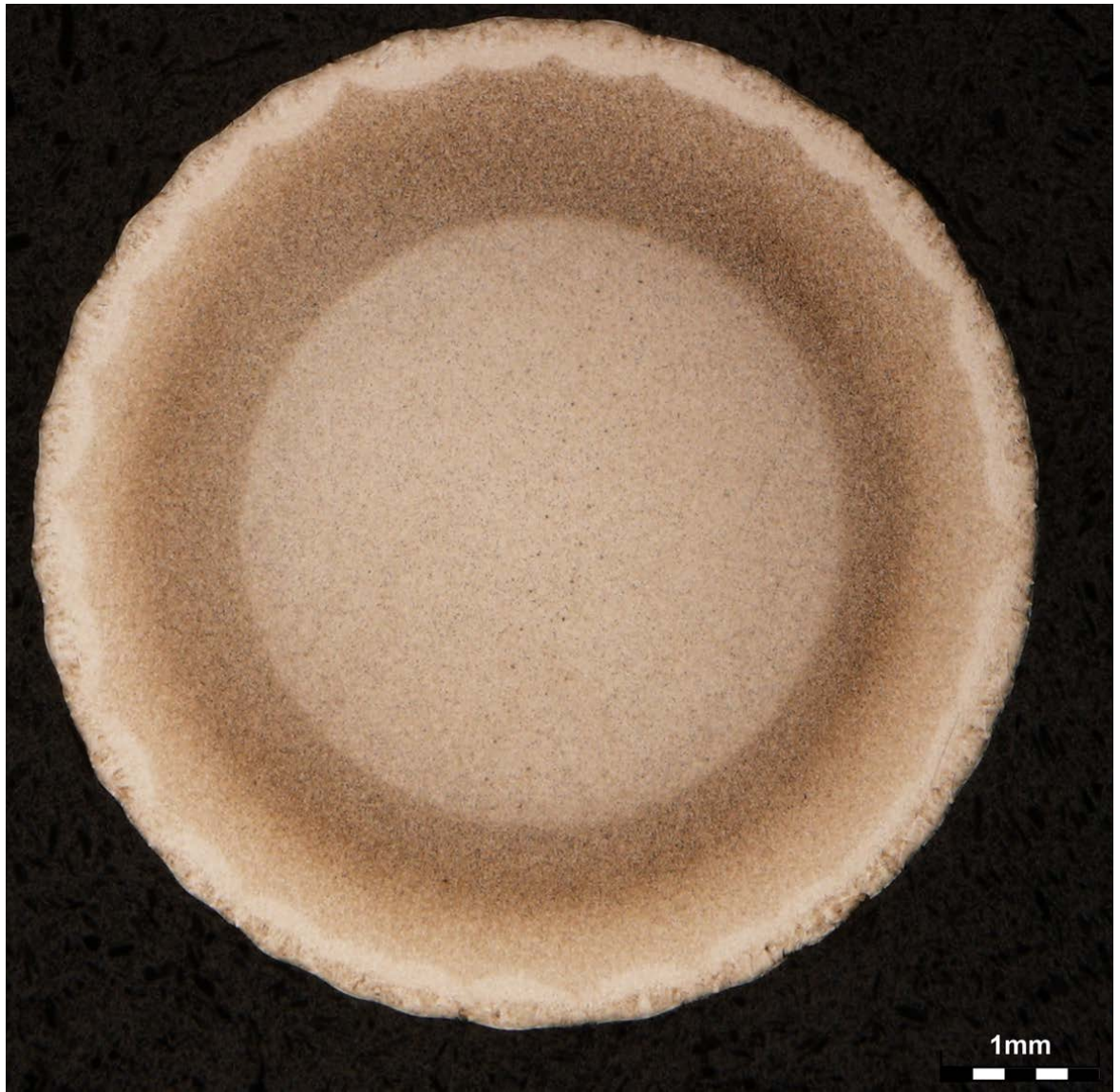
Macrograph



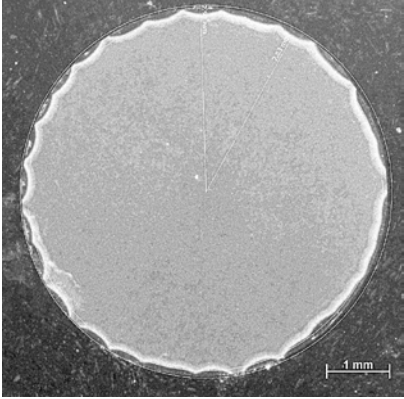
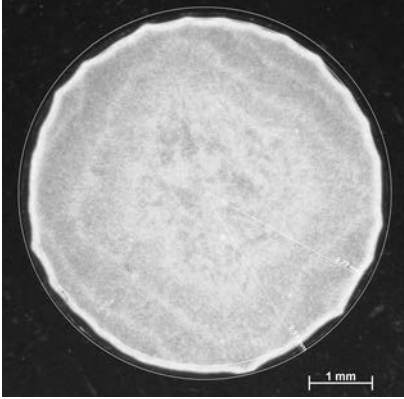
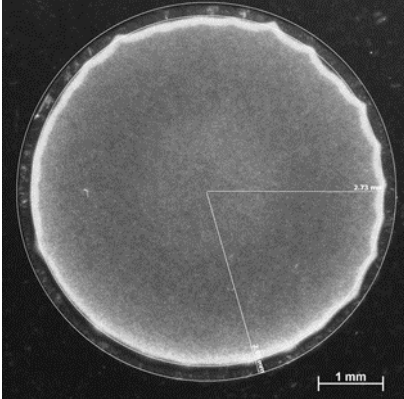
Specimen: LST 18

Energy Input (J/mm)	3.95
Power Density (W/mm ²)	1211.5
Energy input category	Low

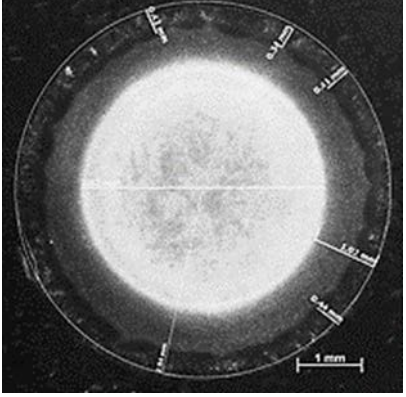
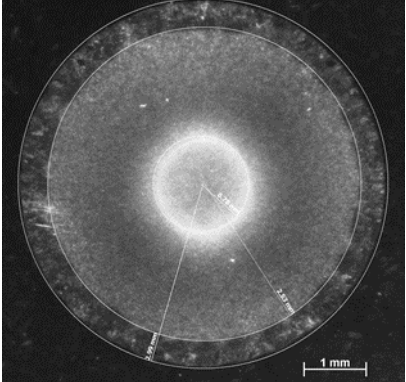
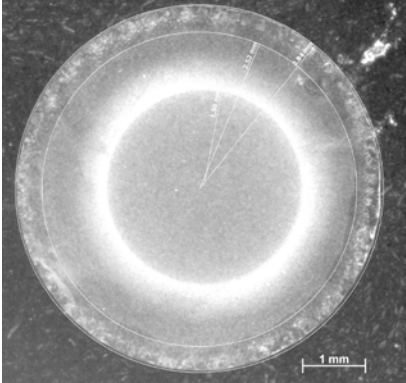
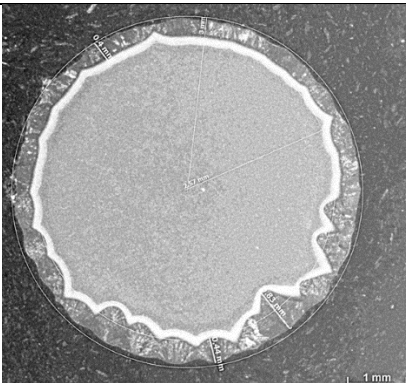
Macrograph



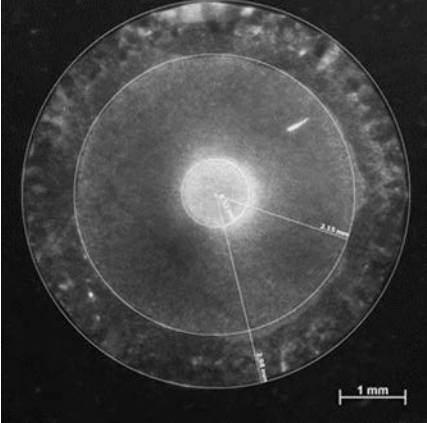
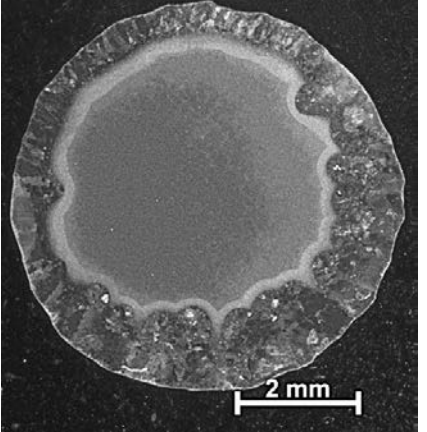
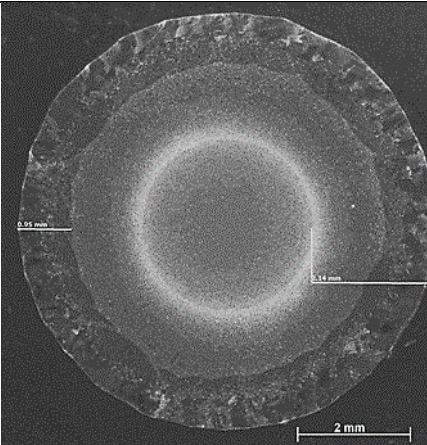
Low energy input specimens' cross section

LST no: FM 11	Cross section
Energy Input: 3.33 J/mm Power density: 318.3 W/mm ² Laser power: 250 W Scanning speed: 75 mm/s Focus position: 6 mm	
LST no: FM 06 Energy Input: 3.95J/mm Power density: 302.9 W/mm ² Laser power: 402 W Scanning speed: 102 mm/s Focus position: 8 mm	
LST no: FM 04 Energy Input: 5.21 J/mm Power density: 795.8 W/mm ² Laser power: 625 W Scanning speed: 120 mm/s Focus position: 6 mm	

Medium energy input specimens' cross section

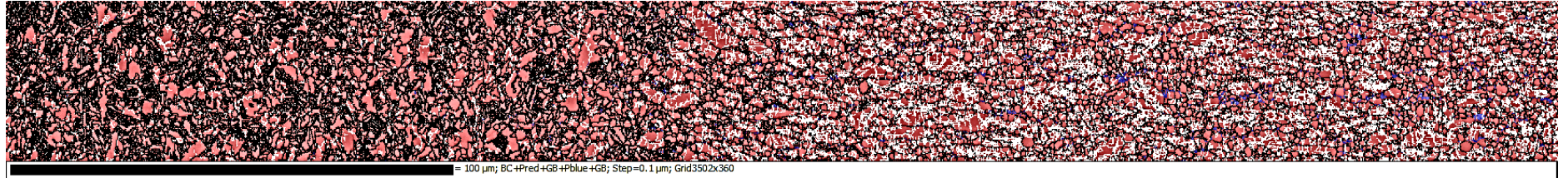
LST no: FM 01	Cross section
Energy Input: 8.33 J/mm Power density: 795.8 W/mm ² Laser power: 625 W Scanning speed: 75 mm/s Focus position: 6 mm	
LST no: FM 03 Energy Input: 8.33 J/mm Power density: 1211.5 W/mm ² Laser power: 402 W Scanning speed: 48 mm/s Focus position: 4 mm	
LST no: FM 12 Energy Input: 8.33 J/mm Power density: 2555.5 W/mm ² Laser power: 625 W Scanning speed: 75 mm/s Focus position: 10 mm	
LST no: FM 13 Energy Input: 8.33 J/mm Power density: 310.8 W/mm ² Laser power: 1000 W Scanning speed: 75 mm/s Focus position: 6 mm	

High energy input specimens' cross section

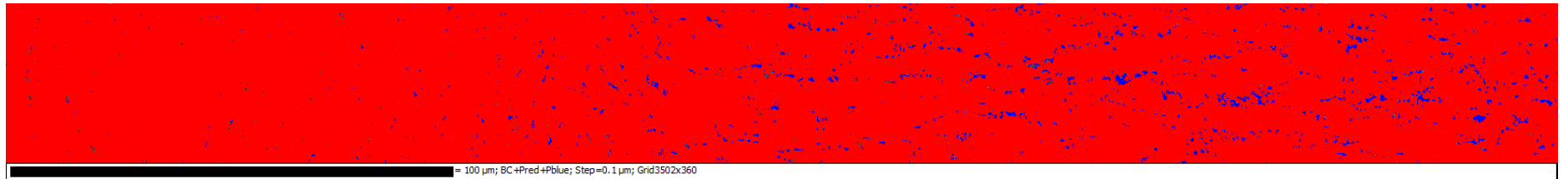
LST no: FM 07	Cross section
<p>Energy Input: 17.58 J/mm Power density: 638.9 W/mm²</p> <p>Laser power: 848 W Scanning speed: 48 mm/s Focus position: 8 mm</p>	
<p>LST no: FM 15</p> <p>Energy Input: 17.58 J/mm Power density: 2555.5 W/mm²</p> <p>Laser power: 848 W Scanning speed: 48 mm/s Focus position: 4 mm</p>	
<p>LST no: FM 02</p> <p>Energy Input: 20.83 J/mm Power density: 795.8 W/mm²</p> <p>Laser power: 625 W Scanning speed: 30 mm/s Focus position: 6 mm</p>	

Appendix D: EBSD results of the RFW specimen

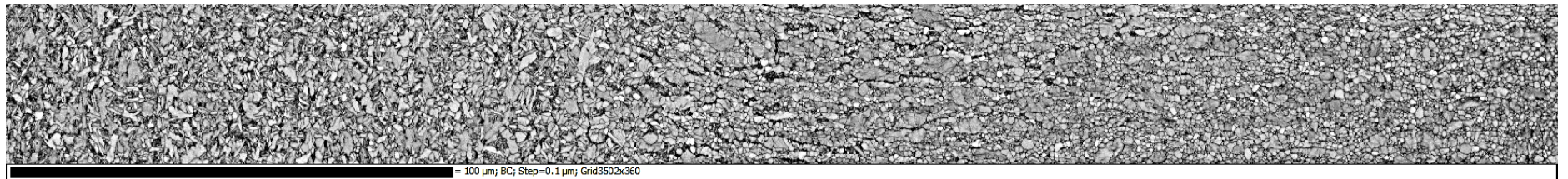
EBSD: Phase distribution α (red) and β (blue), in Band Contrast, Grain boundaries and Sub Grains



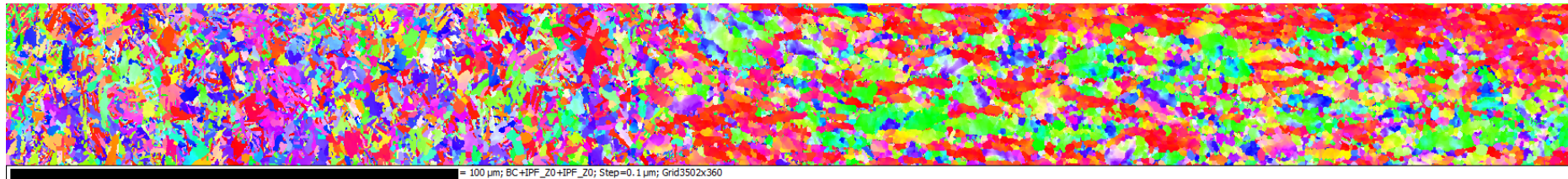
EBSD: Phase distribution, α (red) and β (blue)



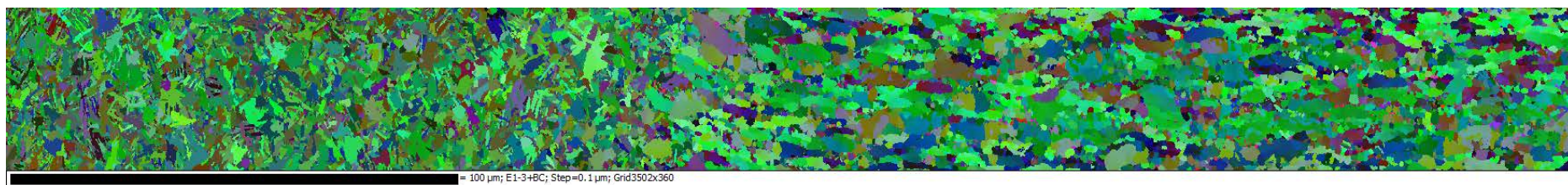
EBSD: Band contrast



EBSD: All euler plot

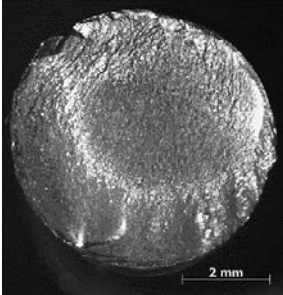
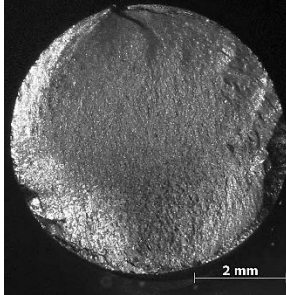
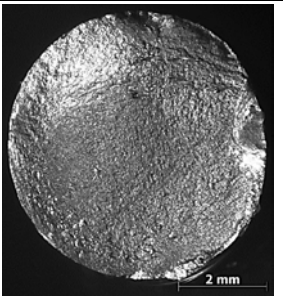
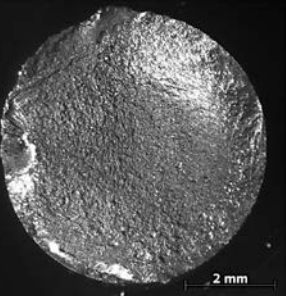
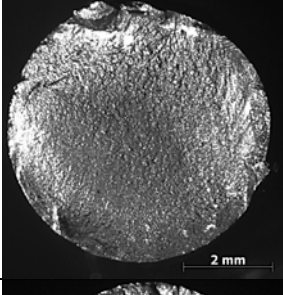
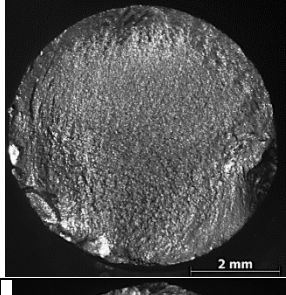
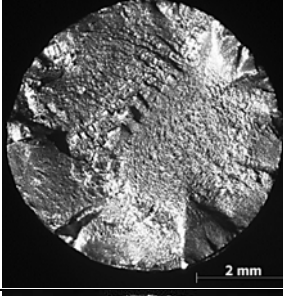
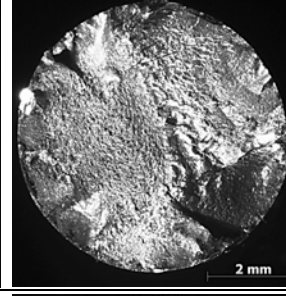
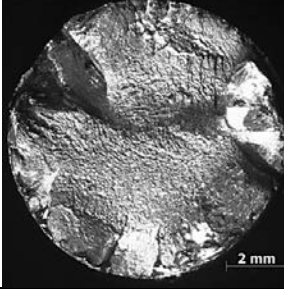
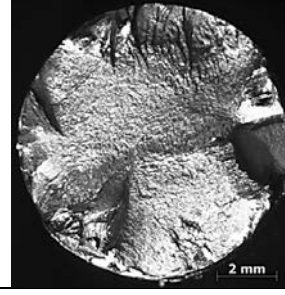


EBSD: All Euler + Band Contrast

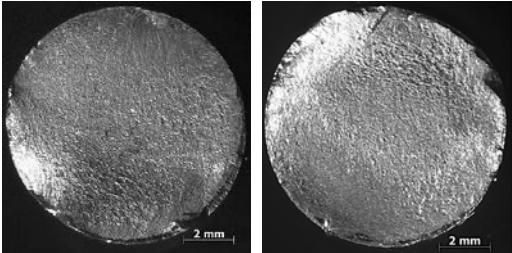
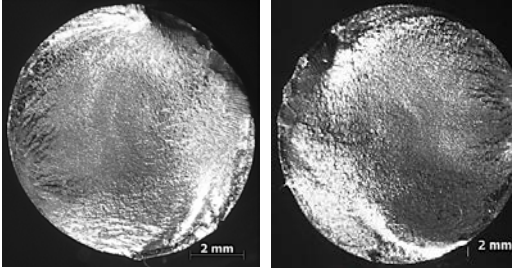
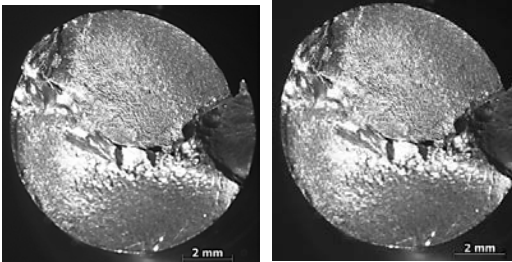
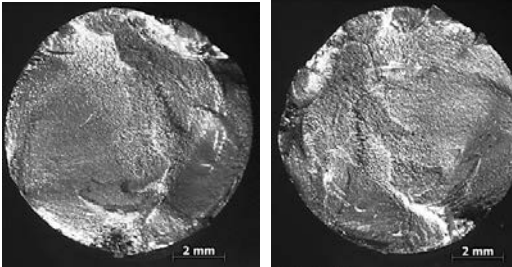
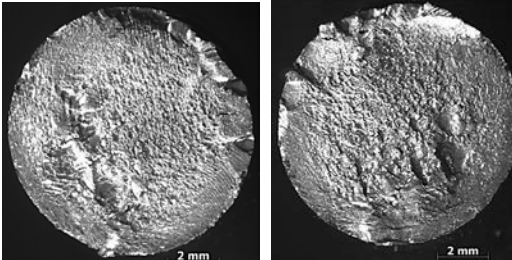


Appendix E: Fatigue Fracture Surfaces

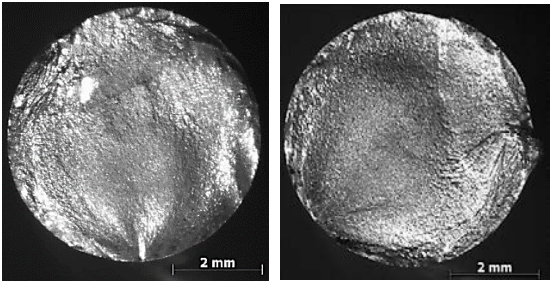
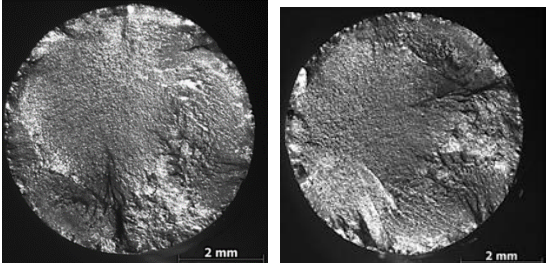
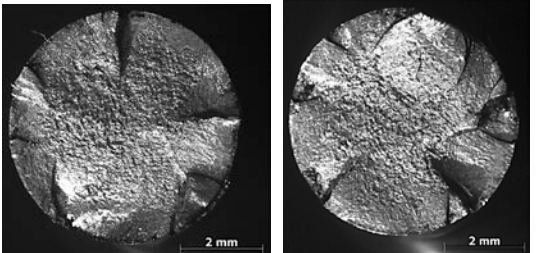
Parent fatigue fracture surfaces

Stress (MPa)	Fracture Surface		No of Cycles	Crack Initiation sites
470			147 000	Surface crack initiation visible
506			28 000	Surface crack initiation visible
521			40 000	Surface crack initiation visible
552			4000	Multiple surface crack initiation visible
603			6000	Multiple surface crack initiation visible

RFW fatigue specimens

Stress (MPa)	Fracture Surface	No of Cycles	Crack Initiation sites
398		88 000	Surface
437		50 000	Surface
480		21 000	Surface
529		16 000	Multiple surfaces crack initiation sites
577		4 000	Multiple surfaces crack initiation sites

LST fatigue fracture surfaces

Stress (MPa)	Fracture Surface	No of Cycles	Crack Initiation sites
501		45 000	Surfaces
548		15 000	Surfaces
621		8 000	Surfaces